REVIEW ARTICLE | JUNE 14 2024

Phonon engineering in thermal materials with nano-carbon dopants

Special Collection: New Carbon Materials

Caleb Stamper ; David Cortie ; Sheik Md Kazi Nazrul-Islam ; Md Rezoanur Rahman ; Dehong Yu ; Guangsai Yang ; Abdullah Al-Mamun ; Xiaolin Wang ; Zengji Yue

Appl. Phys. Rev. 11, 021336 (2024)
https://doi.org/10.1063/5.0173675

Applied Physics Reviews REVIEW pubs.aip.org/aip/are

Phonon engineering in thermal materials with nano-carbon dopants

Cite as: Appl. Phys. Rev. **11**, 021336 (2024); doi: 10.1063/5.0173675
Submitted: 23 August 2023 · Accepted: 14 May 2024 ·
Published Online: 14 June 2024

View Online Export Citation CrossMark

Caleb Stamper,[1,2,a)] David Cortie,[1,2,3,a)] Sheik Md Kazi Nazrul-Islam,[1,4] Md Rezoanur Rahman,[1] Dehong Yu,[2] Guangsai Yang,[5] Abdullah Al-Mamun,[3] Xiaolin Wang,[1] and Zengji Yue[6,a)]

AFFILIATIONS

[1]Institute for Superconducting and Electronic Materials, University of Wollongong, Wollongong, NSW 2500, Australia
[2]Australian Nuclear Science and Technology Organisation, Lucas Heights, NSW 2234, Australia
[3]School of Physics, Faculty of Engineering and Information Science, University of Wollongong, Wollongong, NSW 2500, Australia
[4]Commonwealth Scientific and Industrial Research Organisation (CSIRO) Manufacturing, Clayton, VIC 3168, Australia
[5]Tianjin Key Laboratory of Functional Crystal Materials, Institute of Functional Crystal, Tianjin University of Technology, Tianjin, Xiqing 300387, China
[6]Institute of Photonic Chips, University of Shanghai for Science and Technology, Shanghai, Yangpu 200093, China

Note: This paper is part of the APR Special Topic on New Carbon Materials.
[a)]**Authors to whom correspondence should be addressed:** cjs901@uowmail.edu.au; dcr@ansto.gov.au; and zengjiyue@usst.edu.cn

ABSTRACT

The unique geometric and thermal properties of carbon nanoparticles (NPs)—including nanotubes, graphene, and nanodiamonds—have led to their use as additives in many composite material systems. In this review, we investigate the mechanisms behind the altered thermal conductivity (κ) of thermoelectric (TE) and other thermal materials that have been composited with carbon NPs. We provide a comprehensive overview and analysis of the relevant theoretical and applied literature, including a detailed review of the available thermal conductivity data across five common classes of TE materials (Bi_2Te_3 variants, skutterudites, metal–oxide, SnSe, Cu_2Se) in combination with carbon additives, including graphene, nanotubes, carbon black, carbon fiber, and C_{60}. We argue that the effectiveness of carbon NPs in reducing κ in TE composites generally arises due to a combination of the presence of the carbon NP interfaces and significant changes in the microstructure of the host material due to compositing, such as suppressed grain growth and the introduction of pores, dislocations, and strain. Carbon NPs themselves are effective phonon scatterers in TE composites due to a significant mismatch between their high-frequency phonon distribution and the lower-frequency phonon distribution of the host material. While carbon NP doping has proven itself as an effective way to increase the performance of TE materials, there is still a significant amount of work to do to precisely understand the fundamental thermal transport mechanisms at play. Rigorous material characterization of nanocomposites and spectroscopic studies of the precise lattice dynamics will greatly aid the development of a fully quantitative, self-consistent model for the thermal conductivity of carbon nanocomposites.

TABLE OF CONTENTS

I. THERMAL TRANSPORT IN CARBON COMPOSITE MATERIALS: BACKGROUND AND THEORY

A. Background

Managing thermal energy has always been a crucial task for humanity, originating with the need to maintain our internal body temperatures within a range of only a few degrees. In 2018, the amount of electricity used to cool buildings with air conditioning and fans around the world was approximated to be 20% of their total electricity use.[1] Additionally, the technologies that we rely on for climate control depend on thermal management themselves, since joule heating can result in deleterious performance. Indeed, as we make devices with higher power throughput, such as CPUs built on sub-nanometer-scale architectures, there is a requirement for better thermal energy management. The generation of heat itself represents another issue: the inefficiency of the energy conversion processes in many of our technologies. Over 70% (more than 70 quadrillion watt-hours, per annum) of global energy input is lost as some form of heat after conversion.[2] Increasing energy efficiency by reducing waste heat—thermal energy that is a "lost" by-product of various useful processes—therefore, has three globally crucial outcomes: (1) The development of new technologies, which leads to (2) a reduction in the consumption of precious non-renewable resources, resulting in (3) the reduction of greenhouse gasses and other environmentally harmful waste products. To achieve these goals, materials with unique thermal properties, such as thermal conductivity, κ, are required. Here, we discuss three critical types of thermal materials: high-κ materials that are able to effectively conduct heat ("heat spreaders"), low-κ materials that restrict the flow of heat ("heat blockers"), and those that are able to convert heat into electricity ("heat converters"), i.e., thermoelectric materials. The latter utilize a temperature gradient—maintained by a value of κ—to generate a voltage via the Seebeck effect [Fig. 1(a)]. In fact, the extreme values of κ that are required by these three types of materials can be obtained by deliberately manipulating a linked set of material parameters related to the propagation of lattice vibrations, i.e., phonons.

In order to realize ultra-high or ultra-low values of κ, compositing materials with various forms of carbon allotropes has proven to be a highly effective strategy [Fig. 1(b)].[3,4] Carbon allotropes have incredibly varied thermal properties depending on the nature of their atomic bonding, size, dimensionality, and general form: they simultaneously boast some of the highest (e.g., bulk diamond and in-plane graphene or in-tube nanotubes) and lowest (e.g., amorphous carbon and cross-plane graphene or cross-tube nanotubes) thermal conductivities of any known materials.[5,6] As a result, various carbon materials have been widely employed as additives in order to form composites with properties consisting of either a combination of the intrinsic properties of the host and carbon additive materials or entirely unique properties that result from interface effects or changes to the host matrix due to the presence of the carbon dopant [Fig. 1(c)].[7] In inorganic thermoelectric (TE) materials (e.g., Bi_2Te_3, SnSe, Cu_2Se, PbTe), carbon nanomaterials have been employed as an additive to not only greatly increase their efficiency through κ but also to improve mechanical stability, flexibility, electrical conductivity, and ductility.[4,8,9] The large increase in efficiency of TE materials when composited with carbon nanomaterials primarily originates from the reduction of the lattice thermal conductivity, which is a consequence of additional phonon scattering induced by the nanoparticles and is typically *not* a reflection of the thermal properties of the carbon material of choice. Although many carbon–TE nano-composite materials have been studied, the underlying heat transport mechanisms responsible for the drastic reductions in κ are not well understood. In contrast, high thermal conductivity carbon materials such as carbon nanotubes, carbon fibers, and graphene have been widely incorporated into host materials such as polymers and metals, with the goal of increasing their thermal conductivity and mechanical properties for applications such as electronic packaging and thermal interface materials.[3,10–12] These observations indicate that the host–particle interactions play a critical role in determining the thermal conductivity of carbon composites. Therefore, there is still scope for improving the thermal conductivity of carbon composite materials by better understanding the underlying mechanisms responsible for heat flow and developing synthetic methods accordingly.

In this review article, we survey the progress and understanding of engineering thermal transport in solid-state materials utilizing various forms of carbon nanoparticle dopants, with a particular focus on thermoelectric (TE) materials. We focus on heat carried by lattice vibrations (κ_L), which are important in all material systems and are of primary importance in TE materials. An overview of the key factors influencing κ_L in TE and other solid-state materials, as demonstrated in the main body of this work, is depicted in Fig. 1(d). The review is organized as follows: In Sec. I, we begin with a brief overview of thermoelectric materials and the effect of doping with carbon nanoparticles on thermal conductivity. We then present an overview of the theoretical models used to understand thermal transport in composite systems, focusing on effective medium approaches, thermal boundary resistance, phonon scattering in the Boltzmann-transport regime, and diffuson-mediated thermal transport. Section II details the current literature that brings special insight into the effects of nanocarbon compositing on thermal conductivity, providing a case-by-case overview and analysis. While the primary focus of this article is on TE carbon nanocomposites, we also draw on the literature of metal- and (to a smaller degree) polymer-based carbon nanocomposite materials. Metal and TE matrix carbon nanocomposites, in particular, are valuable systems to overview in parallel since they utilize overlapping synthesis methods and have similar particle–host interactions.

While separate reviews have independently investigated general phonon engineering approaches to the reduction of thermal conductivity in TE materials,[13–15] and the effect of carbon doping on overall TE performance,[4] there has not yet been a comprehensive review of

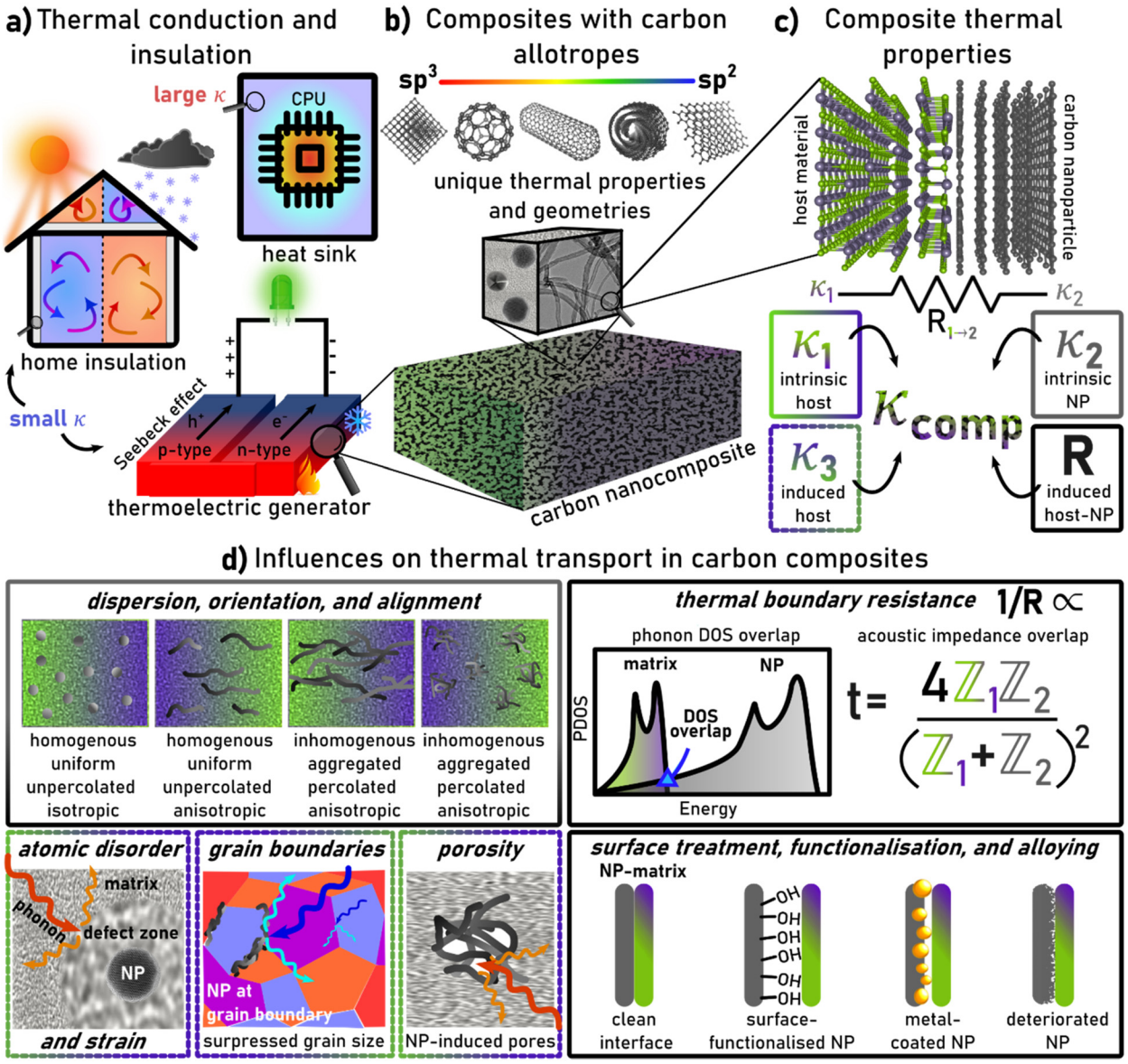

FIG. 1. Overview of the uses of engineered thermal materials and the contribution to the thermal properties of carbon composite materials. (a) Examples of applications of materials with high and low thermal conductivity, including thermoelectric materials. (b) Examples of different types of carbon NP composites. (c) Example of a carbon–host interface. The resulting thermal conductivity of the composite, k_{comp}, will have intrinsic contributions from the host and carbon particles, and induced contributions from the resulting NP–host interfaces and microstructural changes due to the compositing process. (d) Overview of the influences on thermal conductivity of carbon–composite materials. The border colors link to the related properties in (c).

the effect of varying carbon allotrope dopants on the *lattice* thermal conductivity of carbon TE composites. Additionally, published works on the thermal conductivity of polymeric[3,12,16] or metallic[10,11] composite systems with carbon typically have a sole focus on utilizing carbon to *increase* the thermal conductivity of the matrix. As will be demonstrated, a more nuanced approach to understanding κ_L is required for thermoelectric materials, and this approach also provides insight into the thermal transport of polymeric and metallic composites.

B. Carbon nanoparticle doping in thermoelectric materials

Thermoelectric (TE) materials have been researched extensively, particularly in the past decade, with the hope that they will allow for a vast number of novel technologies to be developed and help with the current energy and environmental challenges.[17–21] When configured accordingly, TE materials allow for the conversion of heat into electrical energy, utilizing an established temperature gradient (ΔT).

Alternatively, TE devices can be configured to provide cooling (via ΔT) when powered electrically, which is the basis of widely used Peltier technology. Some of the fundamental benefits of TE devices, when compared to similar energy technologies, originate from their solid-state nature, which results in high stability and reliability, and minimal to no by-products or emissions.[22] Owing to these properties, TE devices have found many uses including in remote power supplies,[23,24] temperature and gas sensors and controls,[25–28] implantable/wearable devices,[29–34] in automotives,[35] and many more areas. The quality of a thermoelectric material—directly related to its energy conversion efficiency—is typically given by its thermoelectric figure of merit, ZT, as[36]

$$ZT = \frac{S^2\sigma}{\kappa_{total}}T, \tag{1}$$

where S is the Seebeck coefficient (or thermo-power), given by $S = -\Delta T/V$, where V is the Seebeck voltage, σ is the electrical conductivity, and κ_{total} is the total thermal conductivity of the material, which is typically given by the sum of charge carrier (e.g., electron) and lattice (e.g., phonon) contributions, $\kappa_{total} = \kappa_e + \kappa_L$.[37] The Wiedemann–Franz law relates κ_c to σ and to the number of charge carriers, n: $\kappa_e = \sigma LT = ne\mu LT$,[38] where L is the Lorentz number, n is the charge carrier concentration, μ is the carrier mobility, and e is the charge of an electron. Since the number of charge carriers is directly proportional to both σ and κ_e, and the Seebeck coefficient inversely, as $S \propto n^{-\frac{2}{3}}$, it is necessary to optimize the number of charge carriers to optimize ZT. S and σ are interrelated and often difficult to optimize individually without the expense of the other, so they are often coupled together and described as the "power factor," $PF = S^2\sigma$, of a material. Additionally, because an increase in charge transport results in an increase in $\kappa_{total} \propto \kappa_e$, κ_e is often "subtracted" from the material optimization process. Therefore, for a material to exhibit a large value of ZT, it needs to possess a low lattice thermal conductivity, κ_L, and a large power factor. Slack termed a material with this combination of properties as a "phonon-glass electron-crystal" (PGEC) in 1995, which has become a critical paradigm for achieving high-performing TE materials.[39] The reduction of the lattice thermal conductivity (while preserving electrical properties) is essential to achieving high-performing thermoelectric materials.[15,40–44]

With many recent advances in enhancing ZT due to nanoscale phenomena,[45,46] carbon nanoparticles (NPs) such as graphene, carbon nanotubes, and nanodiamond have been utilized to increase the performance of TE materials. This was first demonstrated by Zhang *et al.* in their work on Bi_2Te_3.[8] Nano-compositing (creating a composite material with nanoscale structural characteristics, such as grain boundaries, defects, or secondary phases) tends to result in an increase in PF over the pure, bulk material, due to a combination of quantum confinement effects, energy filtering, carrier-pocket engineering, and other effects.[45] Although often positively affecting charge transport, nanoscale structures also strongly interact with heat-carrying phonons, typically reducing κ_L over the pure, bulk material.

Figure 2 demonstrates this possible enhancement in transport properties by comparing the total thermal conductivity and electrical conductivity of the pure matrix (σ_m and κ_m, respectively) with that of the same matrix composited with a carbon NP (σ_c and κ_c). In most of these examples, a significant reduction in κ coincides with an increase in σ, resulting in enhanced TE performance. However, it is not always

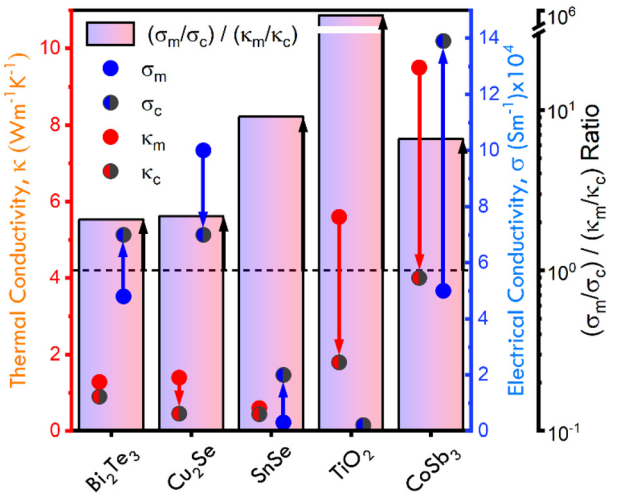

FIG. 2. Comparison of thermal conductivity (red) and electrical conductivity (blue) of pure matrix materials (subscript "m," filled circles) with those composited with carbon NPs (subscript "c," half-circles). A ratio of σ to κ for the matrix and composite is also shown to demonstrate the relative changes in heat and charge carriers (see the text) (blue-red bars). The examples given are for matrix (NP): Bi_2Te_3 (single-walled nanotubes),[47] Cu_2Se (graphene),[48] SnSe (graphene),[49] TiO_2 (graphene),[50] and $CoSb_3$ (C_{60}).[51]

the case that a reduction of κ with the addition of carbon NPs coincides with an increase in σ since the NPs can themselves negatively affect charge transport by acting as charge scatterers. Such a case might suggest that the reduction in κ_{total} is simply due to poor electrical performance (recall that $\kappa_{total} = \kappa_e + \kappa_L$). However, it is often the case that the reduction in σ is far less than the reduction in κ, and compositing can still result in a net positive TE performance enhancement. To illustrate this point, Fig. 2 also includes the ratio of σ_m/σ_c to κ_m/κ_c. This ratio indicates the relative changes in κ to σ from the matrix material to the composite, such that a value >1 (dashed line) indicates a larger decrease in κ than σ. In all of the examples shown in Fig. 2, $(\sigma_m/\sigma_c)/(\kappa_m/\kappa_c) > 1$, indicating an enhanced TE performance, originating in some significant part due to a reduction in κ_L.

To provide an overview of the effect of carbon NP doping on κ in TE materials, Fig. 3 shows κ_m and κ_c for various TE matrix systems doped with a range of carbon NPs.

Evidently, a variety of carbon NPs have a significant impact on κ for many TE systems. In multiple cases, $\kappa_c/\kappa_m < 0.5$. However, it is not obvious whether the type of carbon NP is of significant consequence, as each NP has varied effects within and across TE classes. To understand κ_c in carbon NP-doped composites more deeply, we need to turn to current theoretical frameworks, starting with an overview of the thermal properties of carbon NPs themselves.

C. Nanocomposite thermal conductivity theory

1. Thermal conductivity of (nano)carbon

Before considering composite systems, it is necessary to first describe the properties of isolated carbon phases. This section reviews the principles of thermal transport in carbon allotropes. The thermal conductivity, κ, of carbon materials has a spectacular range of values,

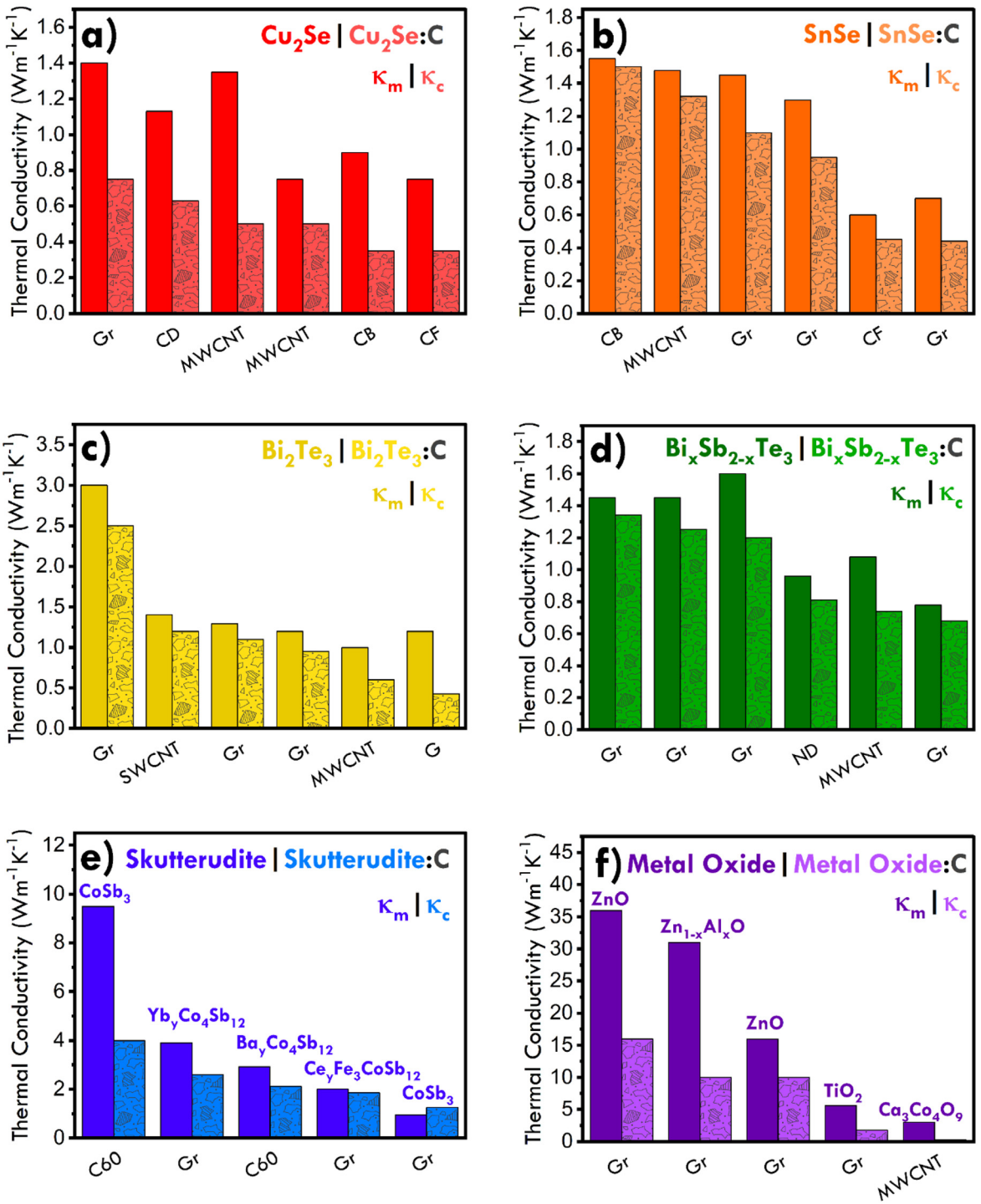

FIG. 3. Comparative overview of the total thermal conductivity of TE matrix materials (solid, dark bars, κ_m) with the same material composited with various carbon NPs (patterned, light bars, κ_c). Each set of samples, corresponding to a pair of matrix and composite bars, is prepared with the same synthesis technique (spark plasma sintering, hot pressing, etc.), is for data taken at 300–330 K, and is for the lowest κ in series taken of doping levels (typically in the range of 0.1–5 wt. %). The host matrices are (a) Cu_2Se,[52–56] (b) SnSe,[49,57–61] (c) Bi_2Te_3,[8,62–65] (d) $Bi_xSb_{2-x}Te_3$,[66–71] (e) skutterudite,[51,72–75] and (f) metal oxide.[50,76,77] The carbon NPs used for compositing are graphene (Gr), carbon (quantum) dots (CD), multi-walled (MW) and single-walled (SW) carbon nanotubes (CNT), carbon black (CB), carbon (micro) fiber (CF), micro graphite (G), nanodiamond (ND), and Buckminsterfullerene (C_{60}).

owing to the many structures that can be formed by different C–C bonding schemes [sp, sp^2, sp^3, van der Waals (vdW)], different atomic-scale "lattice" structures (cubic, hexagonal, amorphous), microstructural dimensions (nano, micro, macro), and different particle geometries (tubular, planar, spherical, etc.). Figure 4 illustrates the diverse range of $\kappa(T)$ values achieved for a variety of carbon materials spanning over five orders of magnitude. Phonons are typically the dominant heat carriers in carbon allotropes and are, therefore, critical to understand their thermal transport. Below, a brief overview of the main features of the phonon transport in carbon is provided.

Phonons are described by a frequency wavevector and energy relationship (band structure), which defines a group velocity, providing a picture that is closely analogous to the transport of ideal gas molecules, photons, and electrons. To link these properties to the thermal conductivity, a common starting approximation is that of an "ideal" gas of non-interacting phonons, where κ is determined by the speed and scattering rates of the phonons at a given temperature (described mathematically later in Sec. I C). In carbon systems, both the speed and scattering of phonons are closely related to the chemical bonding in the lattice. As a general rule, the phonons in carbon materials extend to very high energies (>100 meV or ~25 THz) because of the combination of a light atomic mass, and strong atomic forcefields. However, most of the heat is typically carried by the acoustic phonons, which lie below 50 meV, as these have the highest group velocities. For systems that contain both covalent and van der Waals (vdW) bonding schemes, κ is typically linearly proportional to the percentage of covalent sp^x bonds (as well as elastic modulus and density), because such bonds are typically strong and harmonic (i.e., the atomic forcefields linking two atoms are like that of an ideal spring), giving rise to acoustic phonons with higher group velocity and lower scattering rates. For example, the high thermal conductivity in the basal plane directions (in-plane) of graphite (sp^2) is also due to the harmonically bonded carbon on a well-ordered periodic lattice. In contrast, the thermal conductivity in graphite across the vdW bonded layers (along the hexagonal c-direction, out-of-plane) is significantly lower because vdW gaps are characterized by weak, anharmonic interactions that lead to short phonon lifetimes. Aside from intrinsic features of the lattice and atomic forcefields, κ can also be significantly reduced through phonon scattering by extrinsic defects of various dimensionalities such as grain boundaries, vacancies, and interstitials (described later in Sec. I C). Some common factors that increase or decrease thermal conductivity in carbon are illustrated schematically in Fig. 4. Stronger scattering leads to a transition from ballistic to diffusive transport. At the extreme lower limit in strongly disordered "glassy" systems with aperiodic atomic structures, the phonon picture breaks down and diffusive heat transport via the so-called "diffusons" begins to occur.[78] Thus, at the low extreme, the minimum thermal conductivity of any bulk carbon is in the glassy, amorphous carbon black structures, offering values below 0.1 W m^{-1} K^{-1}.

When carbon phases are formed into nanosized components, they display exceedingly complex thermal behavior. Carbon nanomaterials can be viewed as descendants of their bulk equivalents and,

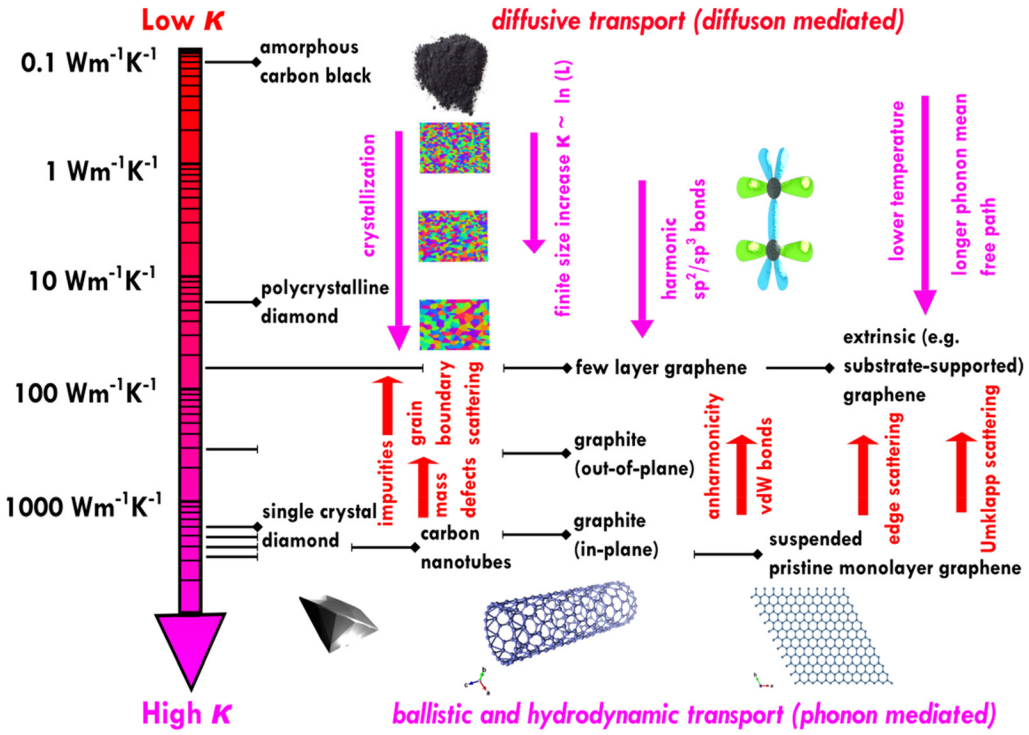

FIG. 4. The intrinsic thermal conductivity of carbon allotropes varies widely over five orders of magnitude, ranging from ~0.1 for amorphous carbon black through to 5000 W m^{-1} K^{-1} for pristine, suspended monolayer graphene. As illustrated schematically, a multitude of physical mechanisms contribute to the diverse behavior including crystallinity, harmonic sp^2/sp^3 and anharmonic vdW bonds, grain boundary scattering, and anisotropy. Figure design inspired by Balandin.[5]

therefore, inherit many of the phononic properties of their bulk parent structure. Examples include graphene, which can be viewed as a single atomic layer of graphite, nanotubes (rolled/tubular graphene), and nanodiamonds (nanometer-scale diamond particles). While nanocarbons share some features with their parent compounds, they also display several unique properties linked to their unique geometry, size, and topology and display a high level of sensitivity to microstructure and defects. The thermal conductivities of nanocarbons are broadly in the same range as bulk carbons, but can sometimes exceed their limits (from 0.1 to 5000 $W\,m^{-1}\,K^{-1}$), as shown in Fig. 4. It is fair to say that many of the factors influencing κ in nanocarbons are far less understood than for their relatively well-studied bulk equivalents. It is worth noting that even when the chemical bonding and atomic-structural motifs are similar, the phonon dispersions of nanomaterials differ from the bulk dispersions. Taking graphene as a representative example, monolayer forms of the carbon allotropes have distinctive acoustic flexural (zA) modes in the low energy region <8 meV (2 THz),[79] whereas graphite has flat, low-energy optical modes in the same frequency range. This is because out-of-plane optical modes are forbidden for a monolayer thick material since optical modes require two layers of atoms to move in an opposite sense. In monolayer graphene, these motions give way instead to the zA modes, which correspond to "wrinkling" in the out-of-plane direction. Despite these differences at low energies, the group velocities of the majority of phonon modes in graphite and graphene are very similar at higher energies, as established in past studies,[79,80] to the extent that graphite data are often used to compare with graphene simulations.

The primary difference between bulk and nanocarbons determining their distinct thermal conductivities tends to be from the altered scattering rates in the compounds. Again, taking graphene as an example, zA modes are found to carry the majority of heat[81] and have reduced scattering compared to the acoustic modes in graphite, such that the mean-free path of phonons in graphene is often very large (500–1000 nm). The first indication of this appeared when the initial measurements of the thermal conductivity of exfoliated, suspended graphene flakes were published in 2008,[82,83] showing that pristine graphene has an enormously high thermal conductivity of 2000–5000 $W\,m^{-1}\,K^{-1}$. While these numbers are undeniably impressive, even exceeding that of bulk diamond, it is difficult to routinely observe such values in practice in graphene nanostructures, as this requires suppressing all defects and substrate interactions. In the literature, there is an enormous range of reported κ values for graphene owing to slight changes in the graphene form and environment, which both influence phonon lifetimes. For example, the presence of multiple-stacked graphene layers drops the κ value to 1000 $W\,m^{-1}\,K^{-1}$,[84] the presence of a SiO_2 substrate interaction typically lowers this to 600–800 $W\,m^{-1}\,K^{-1}$,[85] and the effects of strain and wrinkles can reduce this further to the range of 300–800 $W\,m^{-1}\,K^{-1}$.[86,87] Importantly, partial oxidation of graphene, forming reduced graphene oxide (rGO), can result in structures with a thermal conductivity as low as 8.8 $W\,m^{-1}\,K^{-1}$, which is 300 times lower than that of pristine graphene.[88] In the context of this work, it is worth noting that even when graphene is highly defective, its thermal conductivity is still much higher than many other materials, e.g., polymers or standard thermoelectrics, which have conductivities in the range 0.05–5 $W\,m^{-1}\,K^{-1}$. Evidently, chemical and microstructural defects and interfacial interactions can have a drastic effect on the phonon transport in graphene, and similar features are expected to apply universally in nanocarbons. These factors are expected to have significant implications for carbon NPs in composites, which undergo various treatment procedures and take on various local chemical environments.

The particle nature of nanocarbons, i.e., their finite size, geometry, and large fraction of surface atoms, further influences their lattice dynamics via unique whole-particle resonances, surface modes, and surface scattering. For crystalline nanoparticles, ballistic phonon transport is expected to dominate within the internal nanoparticle for structures in the range of 10–100 nm, as these have a size that is smaller than the intrinsic phonon mean-free path. It is also well-known that finite-sized macroscopic objects exhibit size and shape dependent mechanical resonances, such as breathing modes in isotropic elastic spheres (spheroidal Lamb modes).[89] Such resonant modes have been observed in various NPs, including nanodiamond,[90] and are expected to contribute to their thermal properties.[91–93] Atoms within a few monolayers of NP surfaces also participate in distinctive vibrational modes, which give rise to an excess of low-energy vibrations over the bulk phonon modes, and also high-energy surface modes above the normal bulk cutoff.[94–96] The high surface area offers a host of guest molecules (e.g., H) to form the so-called riding modes, which involve coupling between the particle's normal phonon modes and those of the guest molecule.[97,98] Internal stresses from NP surfaces also cause shifts in energy of phonon modes, and disorder and discontinuity at NP surfaces cause mode broadening often associated with reduced phonon lifetimes.[96] It is worth noting that the features listed above have mainly been observed in non-carbon NPs or only via simulation. Direct experimental evidence in nanocarbons is still lacking in some cases, and more experimental work using advanced spectroscopies (e.g., neutron spectroscopy) is required. Furthermore, understanding the role of these features in the thermal conductivities of NPs and their composites is an emerging area.

For the purpose of this review, we focus on experimental trends for the most common nanocarbons used in thermoelectric and metallic composites. Most of these composites are primarily composed of carbon nanotubes, nano-graphene, nanodiamond, various forms of amorphous carbon, or carbon (micro) fiber. We point interested readers to works by Balandin,[5] Xu *et al.*,[99] and Han and Fina,[3] for further reading on the intrinsic thermal properties of isolated (non-composite) carbon nanomaterials. Importantly, understanding the properties of the composite requires an understanding of both constituent phases and the synergistic new effects that occur because of the introduction of interfaces (e.g., via thermal boundary resistance) or other phonon effects in the composite.

2. Composite models for thermal conductivity

When secondary phases are introduced into a host matrix, a common approach to modeling the thermal conductivity of the resulting composite is to consider the composite as having some sort of mixed contribution of thermal conductivity from the matrix, κ_m, and dopant/filler, κ_f, in their bulk forms, giving an effective thermal conductivity (ETC) of the composite, κ_c. This is called the effective medium approach (EMA). While EMA models have been successfully applied to describe the behavior of composites where both phases are present as macro or microphases, their suitability for nanoparticle composites is still open to debate. Nevertheless, since many works still

invoke such models, and the general framework is still valuable, we introduce some relevant EMA models here.

The contribution of κ_m and κ_f on the ETC will depend on their respective volume fractions, $V_f = 1 - V_m$. The two most basic composite/mixture models are the parallel and series models, which generally represent the upper and lower bounds, respectively, of the thermal conductivity of a mixture. In the parallel model, perfect contact between the matrix and dopant and percolation is assumed, and each material is expected to contribute independently to the ETC: $\kappa_c = \kappa_m V_m + \kappa_f V_f$. In other words, the parallel model assumes parallel layers of host and dopant, with respect to the direction of heat flow. The parallel model is equivalent to the so-called "law of mixtures." The series model, however, assumes no contact between the dopant particles, i.e., layers of material perpendicular (in series) to the direction of heat flow, giving: $\kappa_c = \frac{1}{(\kappa_m/V_m + \kappa_f/V_f)}$.[3] In addition to the parallel and series models, one other model forms the basis for which most composite EMA models are derived from:[100] Maxwell Garnett (M-G) model.[101] The M-G model has been expanded upon and altered to suit many varying two-phase composite systems. One or more considerations, such as particle size, shape/geometry, and, importantly, thermal boundary resistance, are introduced in models by Fricke,[102] Hasselman–Johnson,[103] Bruggeman–Hanai,[104] Bruggeman–Landauer,[105] Every,[106] and Nan.[107] A comprehensive review of analytical and numerical EMA models can be found in Refs. 11 and 108.

EMA models are commonly applied to polymer–matrix and metal–matrix carbon composite (PMC and MMC, respectively) systems, where the goal of compositing is to benefit from the intrinsic thermal properties of the carbon additive. Indeed, these two systems are primarily responsible for the continued use and development of these models. Typically, EMA models overestimate the ETC of well-characterized composite systems. This overestimation is usually attributed to the existence of thermal boundary resistance (also commonly known as thermal interface resistance or Kapitza resistance, R_K), due to the imperfect transfer of heat through the host–dopant interface. The physical origins of thermal boundary resistance are detailed in Sec. I C 3. As we have seen in Secs. I B and I C, however, the ETC of thermoelectric composites (TECs) with carbon dopants do not seem to reflect the intrinsic properties of the carbon dopants, which typically have thermal conductivities orders of magnitude larger than the host TE material. TEC studies generally tend to focus on how compositing specifically affects phonon transport in the Boltzmann transport framework (see Secs. I C 3–I C 5), treating the carbon particles merely as scattering sites and not (primarily) considering their intrinsic thermal properties. However, EMAs are still used to understand changes in ETC upon doping, typically using a thermal boundary resistance term as a fitting parameter to characterize, at least phenomenologically, the magnitude of phonon scattering originating from the dopant. Herein, we aim to bridge the apparent gap in understanding that exists between these paradigms.

One of the most commonly invoked EMA models for understanding the thermal properties of carbon nanoparticle (NP) composites in PMCs, MMCs, and also TECs, is the model developed by Nan *et al.*[107] This model is derived from the M-G model but also includes the effect of the thermal boundary resistance. The most general form of this model considers particles with arbitrarily spheroidal geometry, uniformly embedded in composites with arbitrary orientation. When special limiting cases are applied, other EMA models are recovered. For example, when considering long, continuous, aligned fiber-shaped particles, Hassleman and Johnson's result is recovered (perpendicular to the fibers),[103] as is the rule of mixtures for a simple parallel model (parallel to the fibers). Laminated flat plates, spheres, and misoriented ellipsoidal particles are other available limiting cases that also return results from other EMA models.[107] Additional work has been done to specifically apply Nan *et al.*'s model to carbon nanotube (CNT)[109,110] and graphene (Gr) particle composites,[111] with increased accuracy and simplicity. Applying the limiting case for high aspect ratio prolate spheroids with highly anisotropic thermal conductivity, the ratio of the ETC to the undoped matrix thermal conductivity of a CNT composite is given by[109]

$$\frac{\kappa_c}{\kappa_m} = 1 + \frac{V_f \alpha}{3} \frac{\kappa_f/\kappa_m}{\alpha + (2R_K\kappa_f/d)}, \tag{2}$$

where α is the CNT aspect ratio and d is the CNT diameter. This model assumes well-dispersed, perfectly straight CNTs in a uniform matrix, which is usually best approximated in the dilute limit ($V_f < 2\%$). Similarly, applying the limiting case for an oblate spheroid with highly anisotropic thermal conductivity, we obtain the following form of Nan *et al.*'s model, which describes the ratio of the effective thermal conductivity, κ_c, to the undoped matrix thermal conductivity, κ_m, applicable for few-layer thick Gr:[112]

$$\frac{\kappa_c}{\kappa_m} = \frac{3\kappa_m + 2V_f(\kappa_f - \kappa_m)}{(3 - V_f)\kappa_f + V_f\kappa_m + \left(\frac{V_f R_K \kappa_m \kappa_f}{t}\right)}, \tag{3}$$

where V_f is the volume fraction, κ_f is the intrinsic in-plane thermal conductivity of Gr, and t is the Gr thickness, assuming well-dispersed, randomly oriented, perfectly straight nanoplates in a uniform matrix. These variants of Nan *et al.*'s model provide an attractively simple and powerful framework for understanding the thermal conductivity of CNT and Gr composites. Further iterations/advances of these and other models include other terms such as more complex geometric factors (e.g., straightness), particle-end (e.g., tube-end) thermal interfacial resistance, and agglomeration effects.[108,113,114]

Another approach that is of interest to TECs, MMCs, and PMCs, is Every's application of Bruggeman EMA (B-EMA) theory, where a large fraction of highly thermally conducting (with respect to the matrix) spherical dopants are incorporated into a matrix.[106] This is an attractive model for approximately spherical carbon inclusions such as micro- or nanodiamond. It takes the simple form:

$$\frac{\kappa_c}{\kappa_m} = \frac{1}{(1 - V_f)^{3(1-a)/(1+2a)}}, \tag{4}$$

where $a = R_K\kappa_m/d$, and d is the diameter of the spherical particle ($R_K\kappa_m$ is often referred to as the Kapitza radius).

While there has been success in applying these models to PMC and MMC systems that result in an increase (or a minor decrease) in κ_c with the addition of highly conducting carbon nanoparticles, there have been few convincing successes by directly applying these models to TECs where the addition of a small amount of carbon NP filler results in a major decrease in κ_c (see Sec. I B). To illustrate the limits of these models from this point of view, we have applied them to TE–carbon composite systems, taking realistic values of relevant material properties from the literature. Figure 5(a) shows the B-EMA model

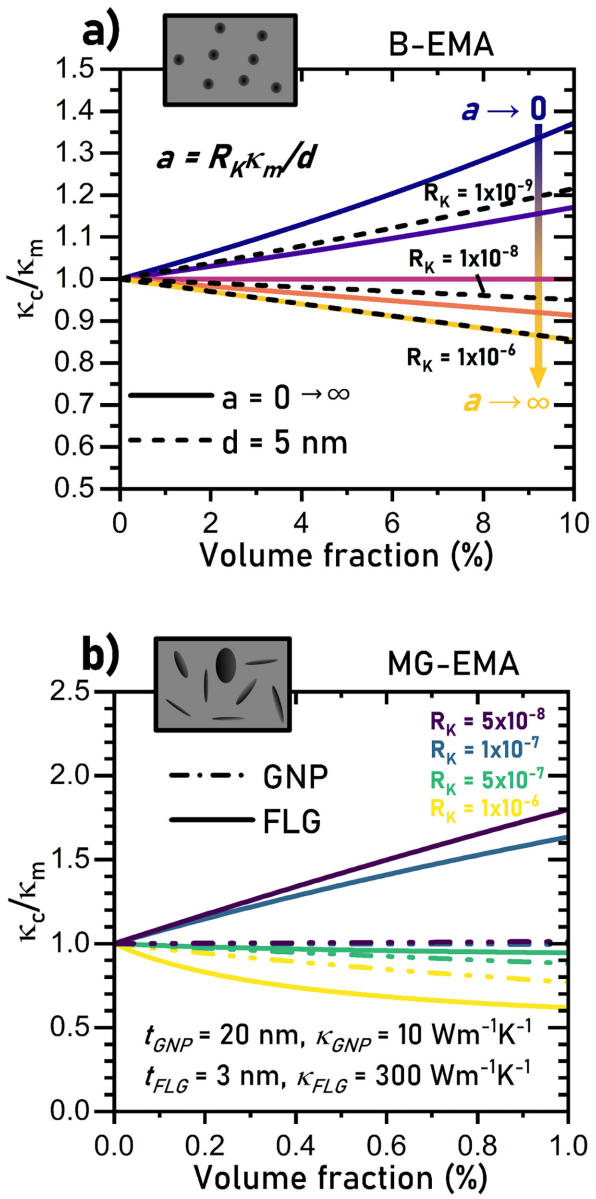

FIG. 5. Demonstration of the limits of commonly used EMA models for carbon NP composites. (a) The limits of Every's application of the Bruggeman (B-) EMA model [Eq. (4)] over the range of 10% V_f by varying a from $0 \rightarrow \infty$ (solid lines), and applied to a system resembling a nanodiamond (5 nm diameter) composite with varying interfacial resistance values (R_K, in units of $m^2\,K\,W^{-1}$) (dashed lines). (b) Nan's application of the Maxwell Garnet (M-G) EMA model for randomly oriented oblate spheroids [Eq. (3)] applied to a composite system consisting of a host with $\kappa_m = 2\,W\,m^{-1}\,K^{-1}$ doped with Gr nanoparticles (GNPs) (dashed lines) and few-layer Gr (FLG) (solid lines) with varying interfacial resistance values (R_K, in units of $m^2\,K\,W^{-1}$) (see the text for rationalization of the values used).

[Eq. (4)] applied to a composite system containing spherical inclusions approximating nanodiamond. Note that, due to the assumptions in the model, only the radius of the dopant, the host thermal conductivity, and the host–dopant thermal boundary resistance are required as inputs. The upper and lower bounds of κ_c/κ_m at the limits of a (where $a \rightarrow 0$ as $R_K \ll d$, and $a \rightarrow \infty$ as $R_K \gg d$) are shown up to a 10% volume fraction. Even in the case of approaching infinite a values (completely thermally insulating nanovoids), a 10% V_f of dopant only decreases κ_c/κ_m by ~15%. For a 5-nm particle such as a nanodiamond, a R_K value of 1×10^{-6} is needed to approach this limit. Despite this value of R_K for a diamond–semimetal interface being larger than would be expected,[115] it still drastically underestimates the reduction in thermal conductivity that can be achieved by doping $Bi_{0.5}Sb_{1.5}Te_3$, for example, with nanodiamond ($\kappa_c/\kappa_m = 0.69$ at $V_f = 0.4\%$).[68]

Figure 5(b) shows Nan *et al.*'s model (MG-EMA) in the limiting case of a thin oblate spheroid, which approximates the shape of a Gr nanoparticle [Eq. (3)]. Two composite systems are presented: a matrix with $\kappa_m = 2\,W\,m^{-1}\,K^{-1}$ doped with few-layer graphene (FLG) and the same matrix doped with graphene nanoparticles (GNP). Volume fractions typical of nanocarbon TECs, which demonstrate significant reductions in κ_m, are presented (up to 1%), as well as R_K values that span from larger-than-expected for (semi)metallic-graphite/graphene interfaces, to realistically small (see Fig. 7; $R_K[1 \times 10^{-6} \rightarrow 5 \times 10^{-8}\,m^2\,K\,W^{-1}] = K_\perp[1 \rightarrow 20\,MW\,m^{-2}\,K^{-1}]$). Combining the wide range of reported values for R_K (spanning ~2 orders of magnitude for TE–C interfaces for similar materials) with the large range of reported values for κ_{Gr} (spanning ~3–4 orders of magnitude for the many types of Gr particles with different thickness values), and possible particle thicknesses, t (typically spanning ~2–3 orders of magnitude), there exists an enormous range of possible values for κ_c/κ_m. Considering $R_K = 1 \times 10^{-6}$ as an upper limit (for further reference, R_K was estimated to be in the range of $\sim 7 \times 10^{-7}\,m^2\,K\,W^{-1} \rightarrow 1 \times 10^{-6}\,m^2\,K\,W^{-1}$ for Gr–skutterudite interfaces by fitting κ_c to a parallel conductance model which includes a boundary resistance term originating from grain boundaries—further discussed in II C),[75] we investigated conditions that resulted in a decrease in κ_m (i.e., $\kappa_c/\kappa_m < 1$), according to Eq. (3). For Gr sheets with $\kappa_{Gr} > 1000\,W\,m^{-1}\,K^{-1}$, a particle thickness of $t \lesssim 2$ nm is necessary to reduce κ_c with respect to κ_m. While these are accepted properties for a Gr particle, we are not aware of any papers that report a composite containing Gr NPs with an average $t < 2$ nm and estimated $\kappa_{Gr} > 1000\,W\,m^{-1}\,K^{-1}$. For Gr with $1000 > \kappa_{Gr} > 100\,W\,m^{-1}\,K^{-1}$, a particle thickness of $t \lesssim 10$ nm is necessary to reduce κ_m, which corresponds to accepted values for few- or multi-layered graphene (FLG/MLG).[112] Finally, for $100 > \kappa_{Gr} > 10\,W\,m^{-1}\,K^{-1}$, a particle thickness of $t \lesssim 50$ nm is necessary to reduce κ_m, which corresponds to the size of GNPs with comparatively low estimations for κ_{Gr}. Evidently, characterizing the properties of the Gr used is essential if Eq. (3) is to be used. Accordingly, the values of κ and t used for the Gr particles in Fig. 5(b) were chosen to represent potentially realistic cases that could result in a significant decrease in κ_c/κ_m. However, despite using generous assumptions, the EMA model still predicts a decrease in κ_c/κ_m that is much smaller than what is observed in most experimental TE systems.

When we recall that carbon nanoparticles of other geometries induce similar reductions in thermal conductivity, despite closely related EMA models not being able to predict this behavior, it is hard to have confidence that the EMA picture is representing the primary thermal transport physics at play in these composite systems. For example, Eq. (2), which describes the limit of prolate spheroids (representing CNTs) in the same EMA scheme as Eq. (3), cannot yield values of κ_c/κ_m below 1. This stands in direct opposition to the established

experimental fact that TE–CNT composites exhibit similar reductions to other carbon nanoparticles (recall Sec. I B). Clearly, a more nuanced picture is required to understand the thermal properties of these composite systems. One assumption that is often made when applying these EMA models is that κ_m remains unaffected by the doping process. In Sec. II, we illustrate the extent to which this assumption does not hold, and we suggest that this is one of the primary misuses of EMA models that has led to their apparent failure to describe TEC nanocomposites. As a second point, EMA models, by their nature, are macroscopic models assuming two well-defined phases as found in composites with microscale or millimeter-scale heterogeneity such that the length of the phonon wavelength is negligibly small by comparison. The application of EMA models to nanoscale composites is questionable because the important phonon wavelengths (1–1000 nm) in these systems are comparable to the composite microstructure dimensions, making it difficult to rationalize a clean separation between heat flow in the host and dopant. As a first attempt to address this, Minnich and Chen presented a modification to Nan *et al.*'s generalized EMA for composites where the characteristic length of the inclusion is on the order of or smaller than the phonon mean free path by taking into account the increased interface scattering in the different phases of nanocomposites and the thermal boundary resistance between the phases.[116] However, we find for TE materials with intrinsically low thermal conductivity that the modification factor is negligible, offering similar results to those presented in Fig. 5. In Sec. I C 3, we will provide a more complete picture of the nature of thermal boundary resistance, which becomes increasingly important at smaller dimensions with increasing numbers of interfaces. Following this, more detailed approaches for understanding thermal transport in nanoscale composites are presented.

3. Thermal interfaces

Various models have been developed to describe the physical processes occurring at interfaces (grain boundaries, matrix–nanoparticle interfaces, etc.) to understand how heat flows across them. The resistance of heat flow across an interface is often called thermal boundary resistance (TBR), or Kapitza resistance, R_K, after Kapitza who pioneered thermal interface studies with his work in 1941 on interfaces of liquid helium and solids.[117] Understanding R_K has been a historically challenging task since the ability to measure the heat flow across a single interface requires specialized equipment and techniques such as ultrafast time-domain thermoreflectance (TDTR).[118] Additionally, the research community has only recently started to effectively implement computational tools such as molecular dynamics (MD) simulations to understand the most fundamental phonon and electron interactions involved in TBR and thus surpass simple models of TBR.[119] A recent review by Zhang *et al.*[115] on interfacial thermal transport at the nanoscale provides an insightful overview, parallel to our discussion here.

The physical mechanisms of TBR can generally be described by elastic processes; acoustic impedance mismatch, interfacial strain fields, mass density variance, and force constant variance, or inelastic processes; phonon coupling to interfacial vibrational modes.[120] The transmission of phonons across a boundary by *elastic* processes is often modeled by one of two main approaches; a semi-classical Landauer-type model, or a quantum interfacial perturbation model. The Landauer approach considers all interactions at the interface to be described by a phonon-dependent transmission probability, $t(\omega)$, which governs the thermal boundary conductance, $h_B(t,\omega)$, such that the total thermal resistivity is given by $\kappa(\omega)^{-1} = \kappa(\omega)_{bulk}^{-1} + (L_Z h_B(t,\omega))^{-1}$, where L_Z is the spacing between boundaries.[121] Meanwhile, perturbation models essentially apply Boltzmann's transport theory to the composite in an analogous way to single-phase materials, merely treating the interface as an additional scattering site with a specified relaxation time (this approach is discussed in detail in Secs. I C 4–I C 5).[120]

The transmission probability used in the widely deployed Landauer approach can be determined by various models. Most widely used, and generally considered as the upper and lower limits of transmission, respectively, are the acoustic mismatch (AMM)[122] and diffuse mismatch (DMM)[123] models (Fig. 6).[124] The AMM model considers thermal interfaces as perfectly planar, allowing for either completely specular reflection or transmission, analogous to Snell's law for optical interfaces [Fig. 6(a)]. The probability of phonon transmission is determined by the ratio of acoustic impedances, $Z_i = \rho_i v_i$, at the interface, where ρ is the mass density, v is the (acoustic) phonon velocity, and the subscript i denotes the material phase (i.e., material 1 or 2):

$$t_{AMM,1\to2} = \frac{4Z_1Z_2}{(Z_1+Z_2)^2}. \tag{5}$$

The DMM model, on the other hand, considers a completely disordered/rough interface whereby phonons scatter diffusely, losing all

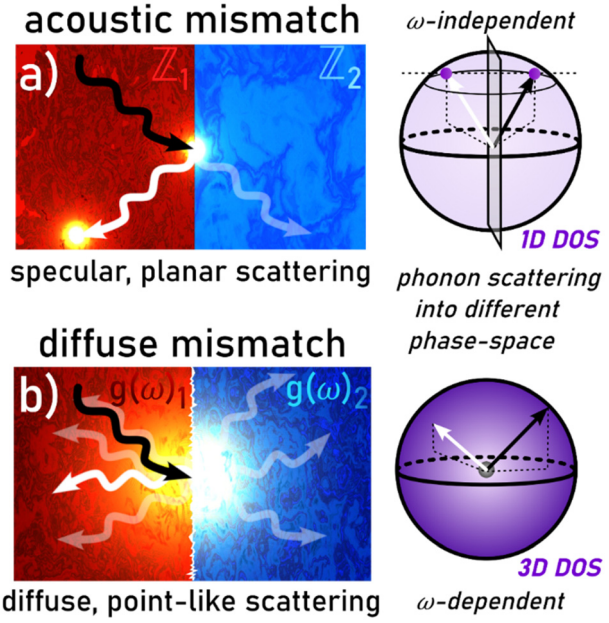

FIG. 6. Illustrations of phonon scattering for commonly used thermal boundary scattering models: (a) acoustic mismatch model (AMM) and (b) diffuse mismatch model (DMM). Incoming phonons (black) are either reflected or transmitted (white or pale white) at the interface of materials 1 and 2, depending on a transmission probability, t. For the AMM, t depends on the difference in acoustic impedance, Z, between materials 1 and 2 and is independent of the phonon frequency (left). The phonon is scattered into the 1D phonon density of states (DOS) due to the planar nature of the scattering (right). For the DMM, t depends on the difference in phonon DOS, $g(\omega)$, between materials 1 and 2, which is dependent on the phonon frequency (left). The scattered phonon is scattered into the 3D DOS due to the point-like nature of the scattering (right).

"memory" of their incoming polarization as if scattered from a point source, as shown in Fig. 6(b). The phonon transmission probability is, therefore, determined by the mismatch of phonon density of states, $g_i(\omega, T)$, summed over all phonon modes (longitudinal and transverse), since only the available phase space on either side of the interface is considered:[124]

$$t_{DMM,1\to2}(\omega) = \frac{g_2(\omega, T)}{g_1(\omega, T) + g_2(\omega, T)}. \quad (6)$$

Unlike the AMM and DMM models, which tend to neglect the detailed structure and properties of the interface in question, the interfacial perturbation approach captures the dimensionality, spatial extent, and physical origin of the interface, following the phonon scattering analysis outlined above. Nonetheless, the differences between the Landauer and perturbation models can demonstrate negligible differences in transmissivity.[120,125] Elastic processes due to the static structure are not the whole picture, however, and cannot account for important local vibrations at the interface, which have been shown to significantly impact TBR.[126] MD simulations have proven to be invaluable in our understanding of the inelastic, dynamical processes at interfaces.[119] For example, it has been shown that vibrational modes in the bulk can couple to modes local to the interface, resulting in a change in TBR.[127]

The TBR term is very sensitive to chemical composition and layer interactions and can vary over orders of magnitude. This is exemplified by comparing interface conductance ($1/R_K$) data for graphene and CNTs. The thermal boundary conductance of single-layer graphene (SLG), few-layer graphene (FLG), graphite, treated SLG (with hydrogen or oxygen), and carbon nanotubes (CNTs) interfaced with various materials were compiled by Xu *et al.* and are shown in Fig. 7.[99] In general, according to both the AMM and DMM models, R_K is expected to be the smallest for PMCs, larger for MMCs, and largest for TECs interfaced with carbon materials. This progression follows the average increase in atomic weight and reduction of bond strength and harmonicity going from polymer to metal to thermoelectric materials. This leads to a greater mismatch of acoustic impedances and phonon density of states between the light, strongly and harmonically bonded carbon atoms in the NPs and the host. Experimental cases are presented and discussed in Sec. II B. Next, we establish the necessary fundamentals to understand thermal transport in a lattice dynamics paradigm and demonstrate the effect of various scattering terms, highlighting those induced by carbon NPs.

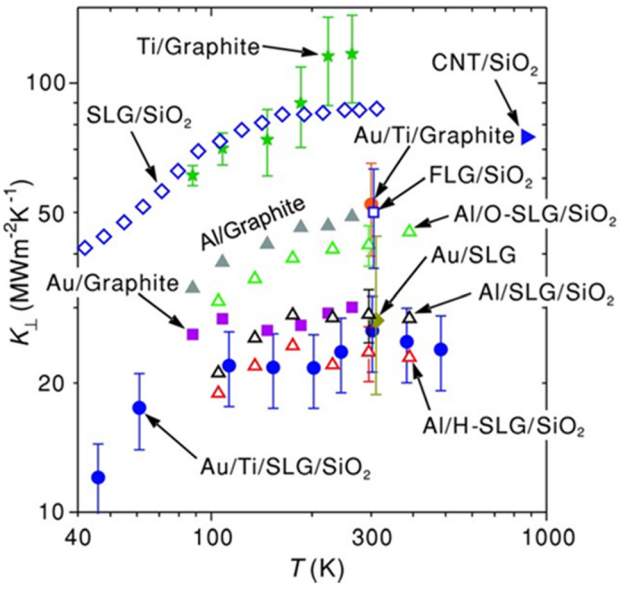

FIG. 7. Experimental thermal interface conductance $K_\perp$ ($1/R_K$) vs temperature for various types of carbon with different interfaces. Reprinted from Xu *et al.*, Small **10**(11), 2182–2199 (2014). Copyright 2014, with permission from John Wiley and Sons.[99]

4. Lattice thermal conductivity in the phonon gas approximation

In most semiconductors and insulators, phonons—quantized lattice vibrations—prevail as the dominant contributor to the thermal conductivity (κ_L). While thermal conductivity from charge carriers (κ_e) is sometimes non-negligible for more conductive materials, such as some highly conducting semiconductors—including high-performing thermoelectric materials—and metals, understanding the role of phonons in thermal transport is critical to all material systems.

A simple and common approach to understanding the lattice thermal conductivity of an isotropic crystalline material is given under kinetic theory, which describes a "gas" of phonons with total heat capacity, C, velocity, ν, and relaxation time, τ:[128]

$$\kappa_L = \frac{Q}{\Delta T} = \frac{1}{3} C \nu^2 \tau, \quad (7)$$

where Q is the heat flux and ΔT is the temperature gradient. More generally, each phonon mode with wave vector, q, and polarization, s, needs to be considered. The equilibrium phonon distribution function, i.e., the average number of phonons with wave vector q, at equilibrium can be written as

$$N_q^0 = \frac{1}{\exp\left(\hbar\omega_q / k_B T\right) - 1}. \quad (8)$$

The total heat flux, with contributions from all q modes, can be substituted into the Boltzmann transport equation under the relaxation time approximation to yield[128]

$$\kappa_L = \frac{1}{3}\sum_{q=1}^{N} \hbar\omega_q \nu_q^2 \tau_q \frac{\partial N_q^0}{\partial T}, \quad c_q = \hbar\omega_q \frac{\partial N_q^0}{\partial T}, \quad (9)$$

where c_q is the heat capacity of a phonon of mode q. In reality, it is difficult to implement Eq. (9) due to the complexity of phonon dispersion curves and frequency spectra of real solids. The Einstein and, subsequently, Debye models for the temperature-dependent heat capacity provide a simple approximation of real systems, where the optical phonon populations are negligible and acoustic phonons dominate as the heat carriers.[129] The Debye model assumes a linear phonon dispersion, $\omega = \nu q$, essentially averaging phonon modes as acoustic branches with group velocity the speed of sound, $\nu = \nu_s$.[130] Within the Debye approximation, the lattice thermal conductivity is given as[128]

$$\kappa_L = \frac{1}{3}\int_0^{\frac{\theta_D}{T}} C(x)\nu^2 \tau_q(x) dx, \quad (10)$$

$$C(x) = 9Nk\left[\frac{T}{\theta_D}\right]^3 \int_0^{\frac{\theta_D}{T}} \frac{x^4 e^x}{(e^x - 1)^2}\, dx, \tag{11}$$

where $x = \hbar\omega/k_B T$ and $\theta_D = \hbar\omega_D/k_B$ is the Debye temperature, chosen so that the total number of phonon modes per unit volume in the integral is $3N$, where N is the number of atoms per unit volume. Equation (10) is analogous to that of the result of a "gas" of phonons [Eq. (7)]. In the high-temperature limit, Eq. (11) tends toward the value of $3R$ (where R is the gas constant), i.e., the Dulong–Petit law,[131] and the thermal conductivity is determined by $\tau_q(x)$. While the Debye model is a good approximation to the heat capacity in many solids, it fails for solids with low energy optical modes and van Hove singularities. For this reason, the Debye model provides a questionable approximation for determining the thermal conductivity and/or mean scattering time for some thermoelectric and polymer compounds that have many low-lying, nondispersive modes. This is particularly true at high temperatures where these nondispersive modes become significantly occupied.

5. Phonon scattering

The inverse relaxation time (i.e., scattering rate) due to various scattering mechanisms can be represented as follows, according to Matthiessen's rule:[132]

$$\frac{1}{\tau_q(x)} = \sum_i \frac{1}{\tau_i(x)}, \tag{12}$$

where $\tau_i(x)$ is the relaxation due to the i th scattering process. A significant effort has been made to identify various phonon scattering mechanisms and their frequency or temperature dependence to help guide the engineering of thermal conductivity in materials. Phonon scatterers are typically categorized in terms of their dimensionality. In general, the frequency dependence of the scattering rate, τ^{-1}, due to different scattering channels will have a ω^2 contribution from the mass difference scattering potential, and a dimensionally dependent component, ω^{n-1}, where $n = 3 - d$ is the codimension of the defect and d is the dimensionality of the scattering site, due to phase space considerations.[120]

Even in a pure, defect-free, crystal, where one would assume that there is no phonon scattering, thermal resistance is present due to the anharmonic bonding in the crystal lattice. Typically, thermal resistance due to anharmonicity is described in the paradigm of three-phonon normal (N) scattering processes, which are momentum conserving, and Umklapp (U) scattering processes, which are not momentum conserving, although these ideas can only truly be held within the Debye model of phonon dispersion.[133] While U-processes directly contribute to thermal resistivity, N-processes indirectly contribute through the redistribution of energy between phonon modes and hence do not restore the phonon equilibrium distribution. Although models have been developed to incorporate N-processes—most famously by Callaway,[134] and recently by Allen[135]—N-processes are usually negligible in terms of proportional contribution to $\tau_q(x)$.[136,137] The U-scattering contribution to the total phonon scattering term is ${\tau_U}^{-1} \propto \omega^2$.[138]

Point defects (0D) are the most elementary defects, consisting of atomic dopants: substitutions, interstitials, and vacancies. Phonons elastically scattered by a 0D defect will not conserve phonon momentum in any direction in phase-space [Fig. 6(b)], leading to a ω^2 phase space contribution to τ^{-1}; the total relaxation time is then proportional to the phonon energy as $\tau_{PD}^{-1} \propto \omega^2 * \omega^2 = \omega^4$,[139] strongly scattering higher frequency phonons.

Linear defects (1D) consist of three primary forms: edge, screw, and mixed dislocations, with edge dislocations being the most commonly considered. The cores of dislocations are linear and scattered phonons conserve momentum in the dislocation direction, which contributes ω^1 to the scattering rate, giving a total rate of $\tau_{DC}^{-1} \propto \omega^3$. The strain field induced by the dislocation itself has a different scattering potential to the mass-contrast and causes scattering as $\tau_{DS}^{-1} \propto \omega^1$.[139] Hence, 1D dislocations are considered to strongly scatter mid-frequency phonons.

Planar defects (2D) are typically characterized as interfaces at grain boundaries, phase boundaries, and stacking faults. Phonons scattered elastically by a plane conserve momentum within the plane and are thus independent of ω [Fig. 6(a)]. In a single-phase compound, planar boundaries (e.g., grain boundaries) also have negligible mass contrast and, therefore, scatter independently of frequency, $\tau_B^{-1} \propto \omega^0$.[139] Planar defects are considered to most strongly scatter low-frequency phonons relative to other mechanisms.

Body defects (3D) are defects that are considerably sized in three dimensions and typically have a considerable mass difference from the host such as (nano)precipitates, secondary phases, and large pores. Because of their relevant scales, the phonon interactions with these 3D defects are often considered at the 2D interface [Fig. 6(a)]. As a result, the scattering rate frequency dependence is like that of a grain boundary but with the scattering potential contribution from the mass contrast, giving $\tau_{BD}^{-1} \propto \omega^2$.[120]

As we will see, compositing with carbon nanoparticles can alter a material's microstructure in multiple ways (we refer to these as induced host properties), such that each of these scattering mechanisms is important to consider. Additionally, we have already demonstrated in Sec. I C that it is insufficient to only consider heat scattering at the host–particle interface in order to explain the drop in thermal conductivity observed in some carbon NP composite systems. To illustrate the effect of these various scattering mechanisms, we have modeled the phonon-energy-dependent scattering rates and (spectral) lattice thermal conductivity (κ_s) for TE $Bi_2Te_{2.7}Se_{0.3}$ with various phonon scattering contributions, using relevant parameters from the literature.[140]

Figure 8(a) shows the scattering rates from eight different contributions: Umklapp scattering, point defects, dislocation strain, grain boundaries, and four different NP systems—nanodiamonds with two different diameters (5 and 20 nm) and doping concentrations (0.1 and 0.2 wt. %). While different material systems will have different contributions from various phonon scattering mechanisms, this selection is representative of the materials discussed in Sec. II. We present these scattering rates with phonon energies up to 50 meV, corresponding to a thermal energy of 580 K. It should be noted, however, that the phonon scattering rates described by these models are only valid for linearly dispersive (Debye) acoustic modes. Typically, TE-type materials only have acoustic modes reaching to 20–30 meV. Higher energies are displayed here in order to relate to a wider range of materials at relevant temperatures. For the NP scattering rate, ${\tau_{NP}}^{-1}$, we implement a model that considers mass and bond stiffness differences between a host and spherical NPs for the scattering cross section in the Rayleigh

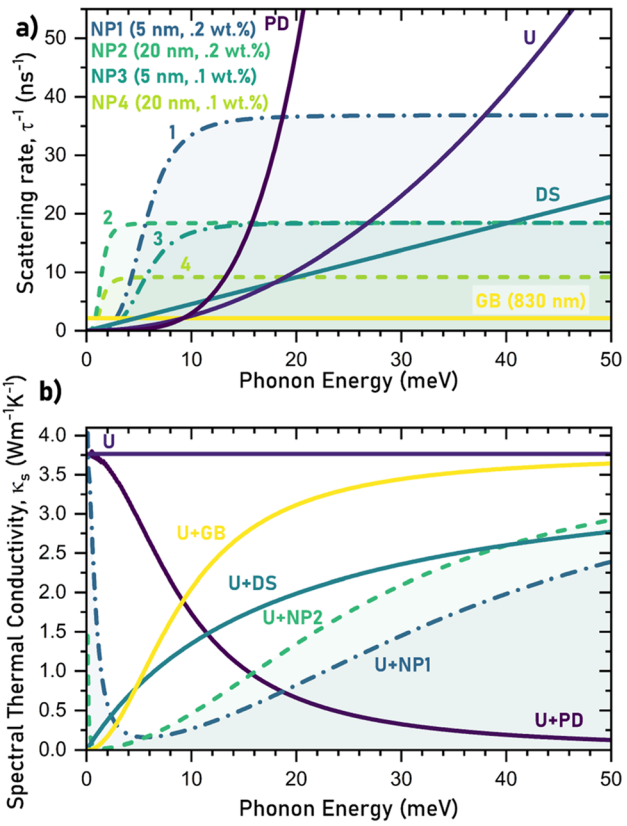

FIG. 8. (a) Phonon scattering in $Bi_2Te_{2.7}Se_{0.3}$ due to point defects (PD), Umklapp scattering (U), dislocation strain (DS), and grain boundaries (GB), calculated using data and equations from Ref. 140 as well as from carbon nanoparticles with diameters of 5 (dash-dot line) and 20 nm (dashed line) of two different concentrations, using Eq. (13). (b) Spectral thermal conductivity, κ_s, of the same material calculated using Eq. (16) with various combinations of contributions to τ.

limit (small size parameter, short wavelength), ${\sigma_s}^{-1}$, and the van de Hulst approximation for anomalous diffraction as a function of acoustic impedance mismatch for the scattering cross section in the long wavelength (large size parameter) limit, ${\sigma_l}^{-1}$:[141,142]

$$ {\tau_{NP}}^{-1} = \nu\left({\sigma_s}^{-1} + {\sigma_l}^{-1}\right)^{-1}\rho, \tag{13} $$

where

$$ \sigma_s = 2\pi R^2, \tag{14} $$

$$ \sigma_l = \pi R^2 \frac{4}{9}\left(\frac{\Delta D}{D}\right)^2\left(\frac{\omega R}{\nu}\right)^4, \tag{15} $$

and ν is the average speed of sound of the host, ρ is the number density of NPs in the host, R is the radius of the NPs, D is the density of the host, ΔD is the difference between the host and the NP densities, and ω is the phonon frequency. It is clear from Fig. 8(a) that even a small number of carbon nanoparticles can very effectively scatter phonons over a wide range of energies and that the size and number of the particles greatly affect the phonon scattering rates. Compared to other scattering mechanisms, according to Eq. (13), NPs are very effective at scattering low-frequency phonons.

To illustrate the effect of these scattering mechanisms on the thermal conductivity, Fig. 8(b) shows the corresponding "spectral" thermal conductivity, which takes the form[134]

$$ \kappa_s = \frac{k_B}{2\pi^2\nu}\left(\frac{k_B T}{\hbar}\right)^3 \frac{x^4 e^x}{\left(e^x-1\right)^2}\tau_q. \tag{16} $$

Evidently, C NPs can greatly suppress the contribution of low-energy phonons to κ. While the differences between NP1 (5 nm diameter) and NP2 (20 nm) seem relatively minor overall, the significantly reduced κ_s for NP2 at energies of <5 meV could be significant since this energy range typically covers most acoustic phonons in TE and similar materials. Compared to grain boundaries and dislocation strain, C NPs, in these instances, do a relatively good job of phonon scattering across this energy range, which covers the most accessible phonon modes in most TE materials. Point defect scattering, however, dominates at energies above ~20 meV, highlighting the benefit of engineering materials with multiple scattering types to cover a range of heat-carrying phonons.

6. Diffuson-mediated thermal conductivity

Before moving on to discussing experimental works, it is important to highlight that the applicability of the phonon gas model has been under scrutiny for some time in amorphous and disordered materials that do not have long-range (with respect to phonon wavelength or lifetime) periodicity, and new frameworks are being developed to account for other transport mechanisms such as diffusive thermal transport. In such disordered materials, anomalous behavior of $\kappa(T)$ is observed, with the usual $\kappa \propto T^{-1}$ relationship expected from Umklapp scattering being replaced with near temperature independence of κ and a minimum κ value much lower than predicted by the standard Cahill limit, which uses the Boltzmann transport equation.[78] The origin of this change in $\kappa(T)$ behavior and lower $\kappa_{minimum}$ originates from the breakdown of the phonon-gas model in the energy regime where heat begins to propagate via diffusive mechanisms, instead of phonons. This energy region is often considered to be above the Ioffe–Regel limit, i.e., where the wavelength and mean free path are comparable.[143] This particular criterion is easily accessible in glassy materials or materials with complex unit cells where there is a lack of long-range structural order or a small number of available propagating (acoustic) phonon modes.[144,145] Allen and Feldman (AF) developed a theoretical framework rooted in Green–Kubo theory involving three types of heat carriers: localized modes (i.e., "locons"), propagating plane wave-like modes (i.e., "propagons" or phonons), and non-plane wave-like, non-localized, diffusive carriers of heat coined "diffusons."[146] The total lattice thermal conductivity in the AF-framework is considered to be $\kappa_L = \kappa_{propagon} + \kappa_{diffuson} + \kappa_{locon}$, where $\kappa_{diffuson}$ is given by

$$ \kappa_{diffuson} = \frac{1}{3}\sum_{q=1}^{N} c_q D_q, \tag{17} $$

and

$$ D_q = \frac{\pi V^2}{3\hbar^2 {\omega_q}^2}\sum_{q\neq n}\left|S_{n,q}\right|^2\delta(\omega_q-\omega_n) \tag{18} $$

is the diffusivity of the q th diffuson of total N modes.[147] $\boldsymbol{S}$ is the heat–current operator that determines the thermal coupling between modes n and q, and the other symbols have the same meaning as previously defined. The relative contributions of $\kappa_{diffuson}$ and $\kappa_{propagon}$ to κ_L have been investigated in various systems, including simple monoelemental crystalline and amorphous Si and Ge,[148] and materials with complex (large) unit cells like Tl_3VSe_4,[149] Yb_{14} $(Mn,Mg)Sb_{11}$,[150] and Nowotny chimney ladder silicides of the form Mn_nSi_{2n-m},[151] which are candidates for TE applications. It is clear that for materials with large unit cells or disorder, $\kappa_{diffuson}$ becomes dominant with increasing temperature, especially at temperatures common for TE applications (κ_{locon} is usually negligible). Additionally, it only takes a small amount of disorder for thermal conduction in a crystal to transition from propagon-mediated to diffuson-mediated.[148] Since, as we will show, C NPs introduce a large amount of disorder—beyond simply the presence of the NPs—we believe that analyzing κ_L in terms of the diffuson framework will lead to an improved understanding of thermal transport in C NP doped TECs.

With the goal of engineering TE materials away from propagating/ballistic transport and toward diffusive thermal transport, it is valuable to consider the theoretical framework for materials that are engineered in the opposite direction: thermally conductive polymers. Polymers, which typically have a spaghetti-like structure, primarily conduct heat diffusively through weak inter-chain interactions.[152] There are two primary approaches to improving κ in polymers: (1) engineering the polymer structure by choosing polymer chains with intrinsically large κ and improving crystallinity through various processing techniques and (2) compositing with thermally conductive materials.[153] In both cases, propagon-mediated transport is promoted through the introduction of long-range order, either intra-chain, inter-chain, or through percolating networks of crystalline secondary phases. These approaches are analogous to those used in TE engineering, but with opposite goals. Approach (1) is analogous to the chemical engineering of TEs, which reduce κ by using weakly bonding elements, creating large unit cells, or by reducing crystallinity through various defects. Likewise, approach (2) is analogous to compositing with carbon or other NPs to reduce κ. Both approaches in TEs promote diffuson-mediated transport by reducing long-range order. In the case of conducting polymer composites, ideal compositing to increase propagon transport involves (a) a minimum number of interfaces (i.e., percolation), (b) interfaces with minimum TBR, (c) minimum influence on any existing crystallinity or long-range order of the polymer, and (d) a dopant with maximum intrinsic κ.[154] On the other hand, TE composites desire the opposite, i.e., (a) a maximum number of interfaces, (b) interfaces with maximum TBR, (c), maximum defects in the crystallinity of the TE, and (d) a dopant with minimum intrinsic κ. Of course, each of these ideally needs to not deleteriously impact other desired properties, such as electrical conductivity. As we will see from the experimental works, small amounts of C NPs are extremely effective at achieving factors (a)–(c), resulting in significant reductions in κ for many TECs.

II. CASE STUDIES OF FACTORS INFLUENCING THERMAL CONDUCTIVITY IN CARBON NANOCOMPOSITE MATERIALS

This section reviews (primarily) experimental works that study the effects on the thermal conductivity of materials compositing with carbon nanoparticles, in light of the theoretical considerations presented in Sec. I. It is divided into sub-sections, each of which highlights the role of a different physical parameter.

A. Particle inclusion (geometry)

1. Dispersion

The nature in which a carbon dopant is dispersed into the host material has crucial implications for the thermal properties of the composite and the applicability of various thermal conductivity models—most of which assume a homogenous dispersion.[108] An increased homogeneity of dispersion of carbon dopant typically results in an increased number of host–dopant interfaces, and decreased agglomeration. Whether a dopant will increase or decrease the thermal conductivity of its host can depend on the thermal properties of the particle agglomerates, percolation, and thermal interface (Kapitza) resistance. Typically, the relatively strong van der Waals attraction between carbon nanoparticles makes including more than a few volume percent difficult without significant agglomeration for most synthesis methods and most host systems. In the case of carbon TECs, the lattice thermal conductivity will typically decrease with a small amount of added carbon and then begin to rise again as the number of thermal interfaces is reduced and the intrinsic thermal conductivity of the carbon—which is usually much larger than the host—begins to contribute more significantly as more contacts between particles are made. However, the relationship between the amount of dopant and the thermal conductivity is also affected by the relationship between dopant concentration and pore formation, grain boundary formation, and the thermal properties of agglomerated particles/bundles, making the effects of dispersion difficult to study in isolation.[3]

Liu *et al.* separated carbon–thermoelectric compositing methods into two categories: *in situ* and *ex situ*.[4] Solid-state *ex situ* methods use ball-milling or mechanical blending or grinding to mix the host and dopant and then a sintering process, such as spark plasma sintering (SPS), to consolidate the mixture. Solution *ex-situ* methods utilize solvent mixing media with stirring and ultrasonication, followed by drying and then consolidation. Often, solution-based *ex situ* synthesis also utilizes solid-state methods (e.g., ball milling). *In situ* compositing can provide high homogeneity via the adherence or growth of part or all of the host directly on the dopant. Assuming that there is no significant diffusion of particles, this ensures that each dopant particle is surrounded by the host during consolidation, minimizing dopant contact. Solid state or other solution-based *ex situ* methods are typically utilized after *in situ* synthesis to perform consolidation of powders or gels into dense solids required for property characterization.

Many attempts have been made to improve the solubility of carbon nanomaterials to aid solution-based *ex situ* mixing. More details and effects on the ETC of the composite are discussed in Sec. II B 2. Briefly, carbon nanoparticle surface functionalization can be separated into covalent and non-covalent routes.[155,156] Covalent functionalization involves the formation of functional groups on the surface of the particles, leading to higher solubility in polar solvents. Non-covalent functionalization aims to achieve this same goal by adsorbing molecules onto the surface of the particles (e.g., via hydrogen bonding, π–π stacking, electrostatic interactions). After improved mixing, samples are dried, and powders consolidated with improved dispersion.

The first *in situ* method for compositing carbon nanomaterials—molecular level mixing—was demonstrated by Hwang *et al.* to

effectively disperse reduced graphene oxide (rGO) flakes in copper.[157] Reduced graphene oxide powders, which contain functional groups such as hydroxyl and carboxyl groups, render the particles hydrophilic, improving dispersion in solution and enhancing the bonding between the rGO and host via covalent oxygen–metal bonds, effectively bridging the carbon and metal atoms. GOs and metal ions are first mixed in de-ionized water, after which the NaOH is used to create GO/CuO powders so that the functional groups on the GOs are not reduced before chemical bonds can be made with the Cu ions. The solution is then dried, and the resulting powder is reduced to rGO/Cu. Finally, the powder is consolidated using SPS. A schematic of this process is shown in Fig. 9. Variations of this process are now widely used, and their effects on thermal conductivity are discussed in Sec. II B 2.

Kim *et al.* reported a synthesis route to create $Bi_{0.5}Sb_{1.5}Te_3$ nanodiamond (BST/ND) composites with highly dispersed NDs by utilizing synthesis conditions that avoid full sintering and grain growth, which would cause ND agglomeration at grain boundaries.[68] As shown in Fig. 10(a), three internal (BST/ND) Gibbs free energy states exist going from a powdered mixture to a fully densified and sintered sample, where G_0 represents the un-sintered powder, G_1 represents the metastable, densified, and sintered sample, and G_2 represents the fully sintered sample with significant grain growth. The ideal, metastable state, G_1, can be achieved by sintering at low temperatures (in this case, below 623 K) and using a sufficiently small amount of ND powder (<0.2 vol. %). It is possible that the point-defect zones surrounding the NDs—assisted by the deformation of the powders via high-energy ball milling—also aid with the stability of the intermediate G_1 state. The thermal conductivity of this system is discussed further in Sec. II C 3.

Islam *et al.*[52] recently developed an interesting solution-based *ex situ* strategy to achieve nanoscale dispersion of amorphous carbon inside of Cu_2Se using grape juice. In their fabrication process, shown in Fig. 11(a), they simply mixed grape juice with Cu_2Se powder and dried the solution on a hot plate. The dried sample was then heated inside an evacuated sealed silica tube, up to 1200 °C. The microstructural analysis using STEM [Figs. 11(b) and 11(e)] revealed a well-dispersed carbon phase inside the Cu_2Se grain boundaries with a Cu_2O phase inside the C and Cu_2Se matrix. Furthermore, Raman analysis showed enhanced disorder of carbon atoms inside the composites [Fig. 11(f)]. The carbonaceous materials inside the Cu_2Se matrix drastically reduce thermal conductivity [Fig. 11(g)].

As mentioned by Han and Fina,[3] it is particularly difficult to provide general rules for the relationship between the dispersion of carbon nanomaterials and the thermal conductivity of their composites. This is because the degree of dispersion is a relative concept, and often only a small amount of evidence (e.g., one TEM or SEM image) is provided. To further complicate the matter, thermal conductivity itself is often used as a metric for dispersion, with the assumption of good agreement with a particular thermal conductivity model. However, as has been discussed and will be discussed further, there are many co-existing factors affecting thermal conductivity. Techniques to disperse nanomaterials more effectively, such as surface treatment, functionalization, or the mixing method, often alter the thermal properties of the host and nanomaterials themselves. Nonetheless, there have been attempts to quantify some of the complex effects of dispersion. The effect of dispersing carbon nanotubes (CNTs), for example, is particularly significant, due to their high aspect ratio. Recently, Wang *et al.* used a micromechanical approach to derive an analytical model for the ETC of CNT composites, which includes a parameter for agglomeration, as well as for waviness, interfacial resistance, CNT alignment, volume fraction, length, and diameter [scheme shown in Fig. 12(a)].[114] Figure 12(b) shows the dependence of the ETC on the degree of agglomeration, c_1 (where $c_1 = 1$ corresponds to fully homogeneously dispersed CNTs, i.e., no agglomeration) as a function of volume fraction, V_f.

2. Orientation and alignment

Due to their highly anisotropic geometry, and hence, properties, the orientation of CNTs, CFs, and graphene/graphite flakes in a

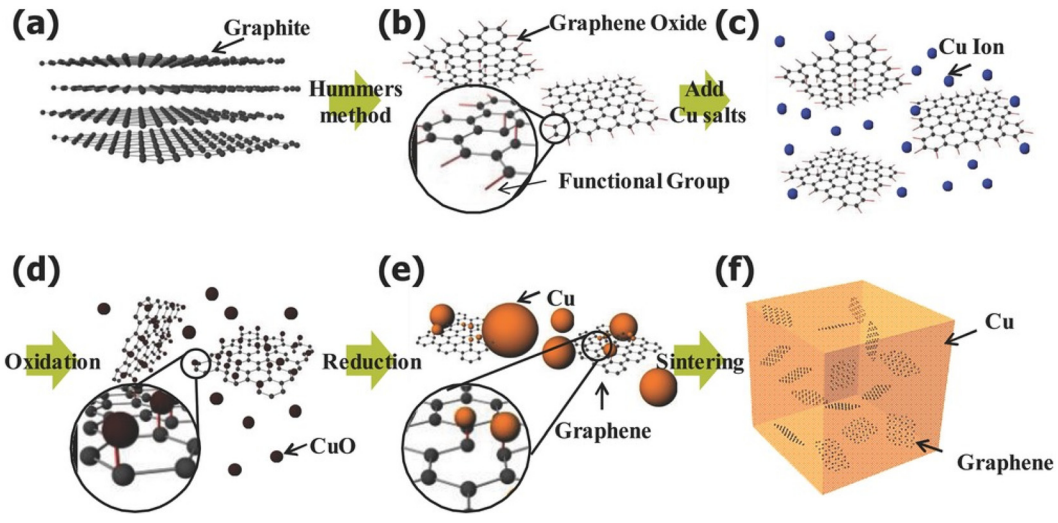

FIG. 9. Schematic of fabrication process of rGO/Cu nanocomposites. (a) Pristine graphite. (b) Graphene oxide by the Hummers method. (c) Dispersion of Cu salt in graphene oxide solution. (d) Oxidation of Cu ions to Cu-oxide on graphene oxide. (e) Reduction of Cu-oxide and graphene oxide. (f) Sintered rGO/Cu nanocomposite powders. Reprinted from Hwang *et al.*, Adv. Mater. **25**, 6724–6729 (2013). Copyright 2013, with permission from John Wiley and Sons.[157]

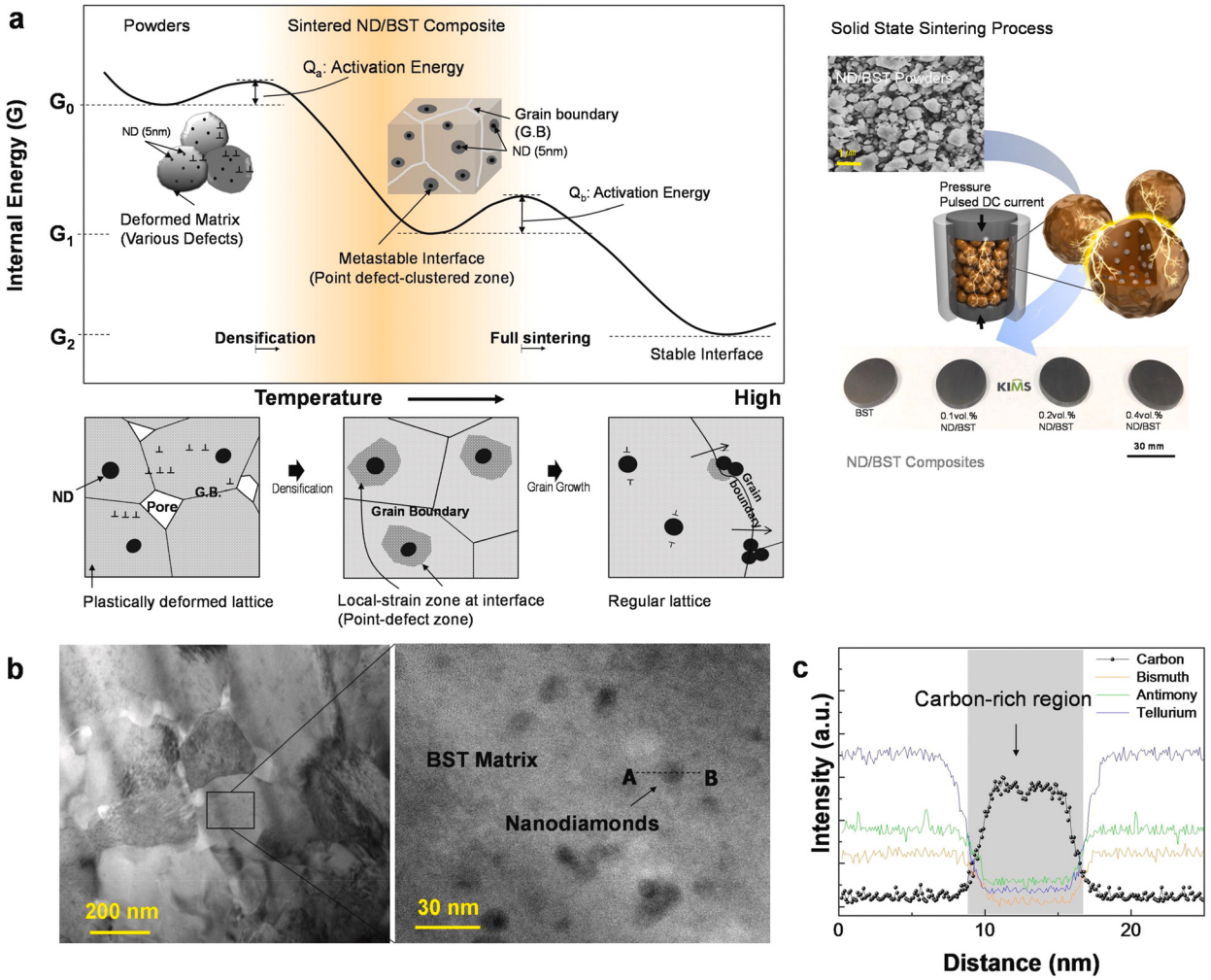

FIG. 10. Concept of point-defect zones formed at the ND/BST interface. (a) Illustrations of the formation mechanism of an interfacial defect region prepared from nanodiamond-dispersed BST matrix composite powders and schematic illustration of the synthetic process of the ND/BST composite with point-defect zones. (b) An HAADF-STEM image and a highly magnified HAADF-STEM image showing ND powders embedded in the BST matrix grain of the 0.2 vol. % ND/BST composite. (c) EDS results of the AB line to confirm the presence of nanodiamond, indicated as a carbon-rich region with a diameter of about 5 nm. Reprinted from Kim *et al.*, Nano Energy **55**, 486–493 (2019). Copyright 2019, with permission from Elsevier.[68]

composite will greatly affect the effective thermal conductivity (ETC) of the composite for a given direction of heat conduction.[158] However, realizing the alignment of anisotropic carbon nanomaterials in different matrices as desired is not simple to achieve nor is the characterization of the particle orientations. Various alignment techniques have been demonstrated in PMCs such as utilizing melt processing, using preformed particle arrays, or aligning with an external magnetic or electric field.[3] Aligning nanoparticles in MMCs and TECs, however, proves to be more difficult.[159] While magnetic field alignment has been demonstrated in Mg CNT composites, there are a few pioneering studies in this area.[160] Here, we discuss studies that investigate the effect of typical synthesis routes for MMCs and TECs on carbon nanomaterial orientation and relate that to the composite's thermal properties.

From our observations, the most commonly invoked model for the ETC of anisotropic-dopant composites is the model by Nan *et al.*[107] The micromechanical approach by Wang *et al.*, mentioned previously, also captures the effect of orientation on the ETC.[114] Their model shows how, for a Cu–CNT composite, ETC changes for aligned vs randomly oriented CNTs with and without interfacial thermal resistance (Fig. 13).

Recently, the orientation dependent transport properties of single-walled (SW) CNT and graphene–ZnO composite materials were studied by Liang *et al.*[161] Their work highlights the anisotropy of the thermal and electrical properties of carbon composites when the orientations of nanoparticles are not completely random due to consolidation procedures involving pressing, such as spark plasma sintering (SPS), demonstrating that significant alignment (also known as

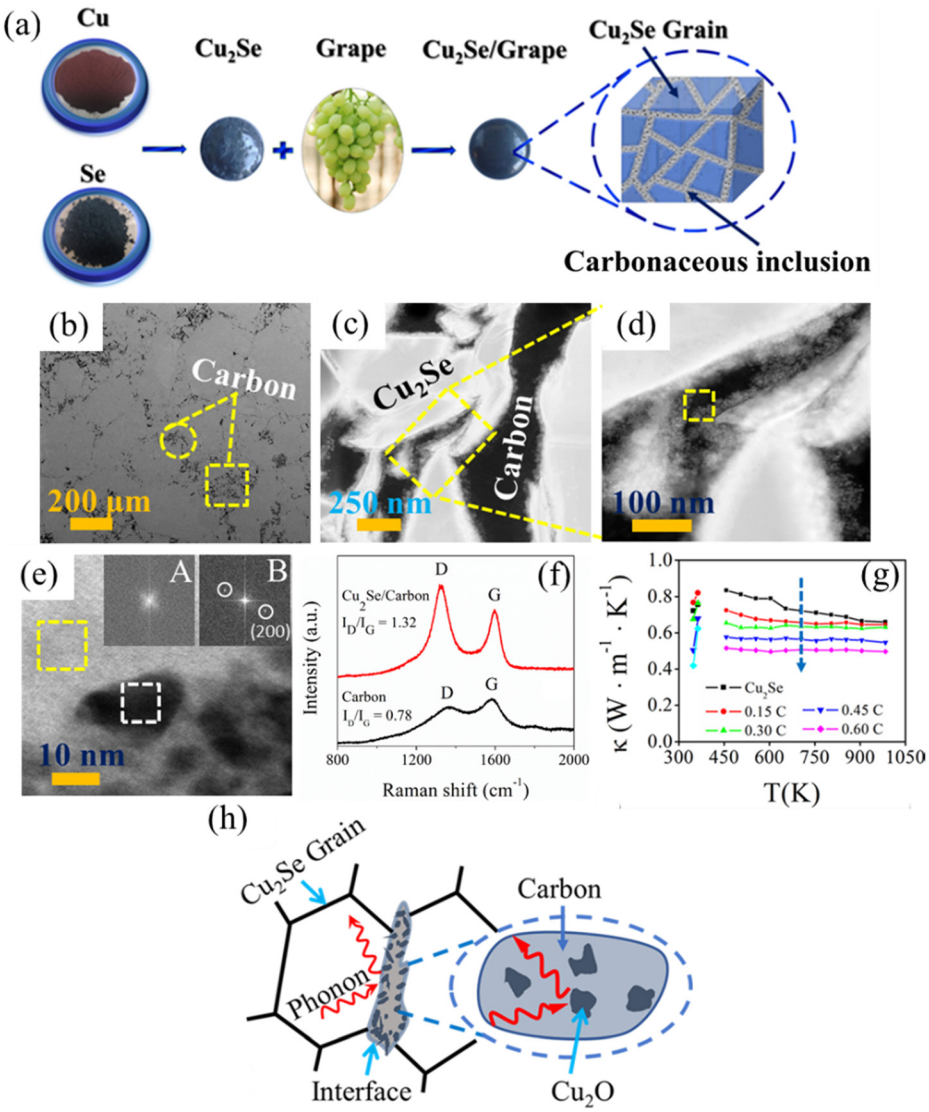

FIG. 11. (a) Schematic illustration of the fabrication process of Cu_2Se/Carbon matrix. (b) Secondary electron SEM imaging showing the carbon inside the Cu_2Se grain boundaries. (c) STEM analysis demonstrating the carbon phase inside the Cu_2Se grain. (d) High-resolution images of the selected region of (c). (e) Amorphous carbon along with Cu_2O phase (dashed squares) is identified by the FFT patterns as shown in the inset. (f) Raman spectra of Cu_2Se/C and pure carbon. (g) Temperature dependence thermal conductivity of pure Cu_2Se and carbon. Reprinted from Islam *et al.*, J. Mater. Chem. A **8**, 16913–16919 (2020). Copyright 2020, with permission from the Royal Society of Chemistry.[52]

"texture") occurs in low dimensional carbon materials during the pressing stage. When measured perpendicularly to the pressing direction, the thermal conductivity of ZnO-SWCNT (1–2 wt. %) composites show negligible differences compared to pure ZnO [Figs. 14(a) and 14(b)]. In the direction parallel to pressing, however, there is a significant reduction in the thermal conductivity across the entire temperature range (∼0–800 °C). A similar result is observed for graphene, with the difference in thermal conductivity between the samples with different dopant concentration being more pronounced. Utilizing their microstructural and thermal conductivity data, Liang *et al.* determined the Kapitza resistance, R_K, by employing Nan *et al.*'s model for the ETC of composite materials [Eq. (3)].[107] Values of R_K are calculated for both the parallel and perpendicular pressing directions and thus associated with side-on/radial and tube-end/axial thermal interface resistance for the CNTs, respectively, and the in-plane and cross-plane thermal interfaces for the graphene, respectively. A schematic illustrating this is shown in Fig. 14(c), with the calculated values for R_K shown in Fig. 14(b). For the CNTs, at 1 wt. %, the radial R_K is significantly larger than the axial R_K, with the difference becoming smaller at 2 wt. %, while the average remains approximately the same. The authors highlight that this is likely due to the increased agglomeration at higher weight percent, confirmed by electron microscope images, which results in a higher probability of phonons seeing both the radial and axial interfaces. The values for the in-plane and cross-plane R_K for the graphene composites are consistent across the two different concentration samples—with the in-plane boundary resistance being much larger than the cross-plane—suggesting that the nanoparticles are similarly dispersed.

Vallet *et al.* compared the anisotropic ETC of Cu-CNT MMCs synthesized via two different routes: a "solid route" (SR) process, where CNTs were simply mixed with the Cu powder, and a "liquid route" (LR) process, where the CNTs were dispersed in a Cu salt solution

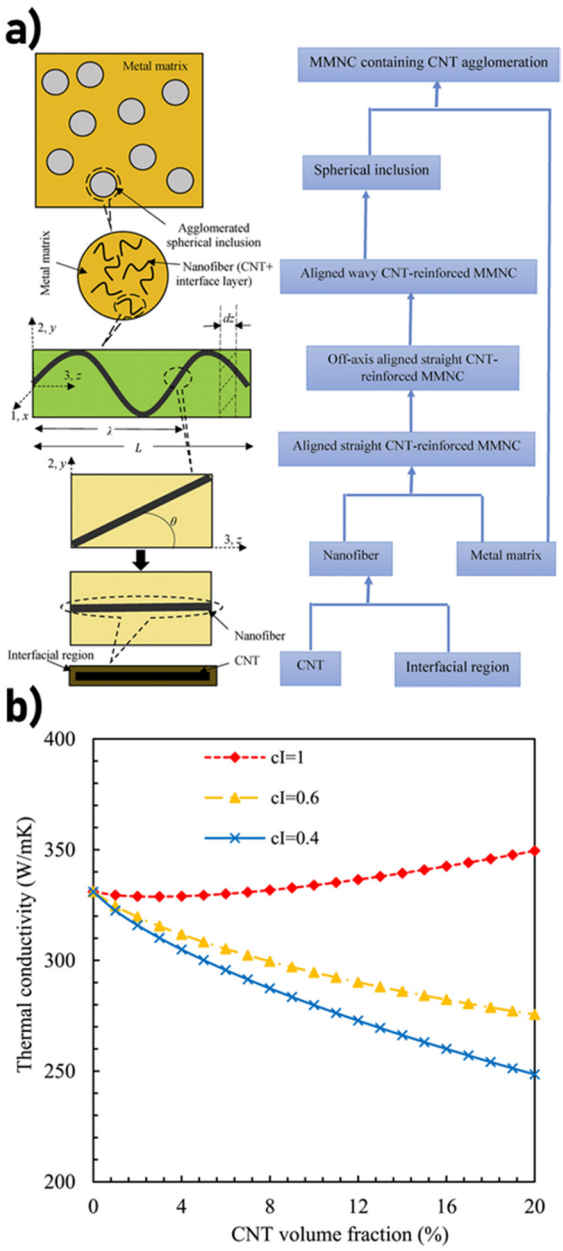

FIG. 12. (a) Schematic representation of the computational approach for estimating the effective thermal conductivity of CNT-reinforced MMCs, including effects from agglomeration, spherical inclusions containing randomly oriented CNTs, aligned wavy CNTs, straight CNTs at an angle, straight CNTs, and CNTs surrounded by an interfacial region, and (b) the effect of the degree of CNT agglomeration, c_I, on the effective thermal conductivity of CNT-reinforced Cu MMCs. Reprinted from Wang *et al.*, J. Alloys Compd. **793**, 191–201 (2019). Copyright 2019, with permission from Elsevier.[114]

(molecular level mixing) and then mixed with the Cu powder.[162] Both routes then used uniaxial hot pressing to consolidate the CNTs and Cu. In their work, they present the CNT volume fraction dependence of the thermal conductivity of the SR and LR fabricated composites and use Nan *et al.*'s generalized model in the limits of different particle orientation ($\langle \cos^2\theta \rangle = 1$ for perfectly aligned CNTs in the direction of alignment, and $\langle \cos^2\theta \rangle = 1/3$ for randomly oriented CNTs) [Fig. 15(a)].[107] Up to 0.5 vol. %, composites from both routes demonstrate a similar ETC value parallel to the pressing direction and match the calculated theoretical value when assuming a random orientation factor and estimated CNT intrinsic thermal conductivity $= 3000\,\mathrm{W\,m^{-1}\,K^{-1}}$ [Fig. 15(b)]. The LR samples continue to follow the model up to 1.5 vol. %, while the SR samples reduce in ETC significantly in comparison. In the direction perpendicular to pressing, the LR samples follow the model with an aligned orientation factor up to 1 vol. % reasonably well, with the 1.5 vol. % sample dropping significantly below the calculated value. The authors suggest that complete alignment of the CNTs is not realistic, and mention that it has been demonstrated previously that they align randomly in a 2D plane perpendicular to the pressing direction. To account for this, the authors modify the CNT thermal conductivity in the model to be the approximate average of the main tube axis ($3000\,\mathrm{W\,m^{-1}\,K^{-1}}$) and the perpendicular radial axis ($10\,\mathrm{W\,m^{-1}\,K^{-1}}$) [Fig. 15(c)].

Comparing the work of Liang *et al.* and Vallet *et al.*, both demonstrate the anisotropic thermal properties of CNT composites arising from processing by hot pressing and SPS methods and are understood using Nan *et al.*'s effective medium model for the ETC.[161,162] However, two different approaches are taken to rationalize similar results. Liang *et al.* invoke changes in the CNT/graphene–matrix interface resistance (side-on/radial and tube-end/axial interfaces, and in-plane and cross-plane interfaces) as the responsible mechanism(s) for anisotropic ETC in ZnO–CNT/graphene and suggest that agglomeration is likely responsible for deviating evidence.[161] Meanwhile, Vallet *et al.* invoke the differing spatial orientation of the CNTs in the matrix as the responsible mechanism in Cu–CNT, with differing intrinsic radial and axial CNT thermal conductivity accounting for deviations in their data.[162] The results of these works and their differing analyses demonstrate the need to perform careful characterization and analysis in order to understand the origins of anisotropic ETC in CNT composites. If this can be done, Nan *et al.*'s model can potentially be used as an indirect method of determining CNT dispersion and orientation. However, this approach is limited by the bundling of all the responsible physical mechanisms of thermal conductivity reduction into R_K. Nonetheless, it is clear that typical consolidation techniques such as SPS and hot pressing considerably affect the anisotropic ETC of TEC and MMC CNT composites, and other processing techniques that align nanoparticles such as mechanical drawing/extruding will likely demonstrate similar anisotropic thermal properties.

B. Thermal boundary resistance

1. Phonon mismatch

The probability of a phonon transmitting through an interface in the Landauer approach (see Sec. I C 3) relies on the phonon density of states (PDOS) of each material at the interface. In the acoustic mismatch model (AMM), a small ratio (large mismatch) of acoustic impedance results in a low phonon transmittance, while in the diffuse mismatch model (DMM), a large mismatch of the PDOS results in a low phonon transmittance. A few studies—presented here—have been conducted to investigate the role of "phonon mismatch" to describe

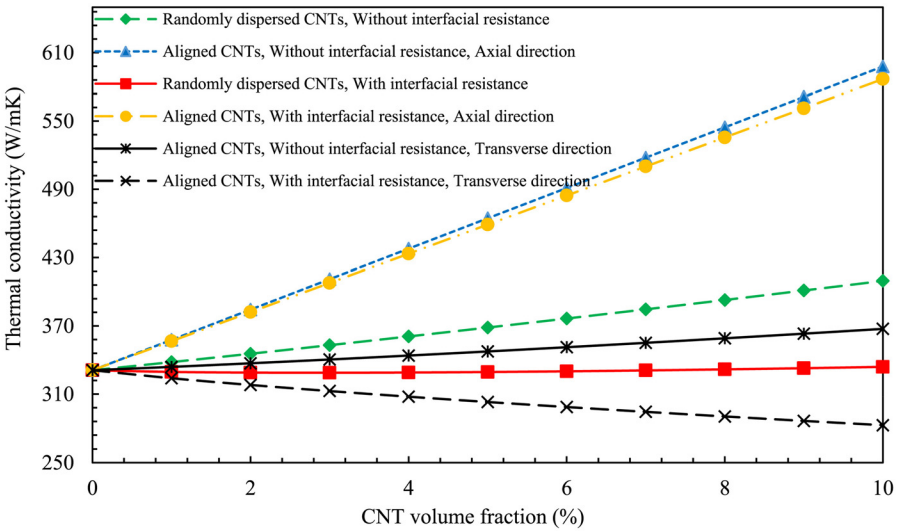

FIG. 13. Effect of CNT arrangement, with and without interfacial thermal resistance, on the effective thermal conductivity of Cu MMCs. Reprinted from Wang *et al.*, J. Alloys Compd. **793**, 191–201 (2019). Copyright 2019, with permission from Elsevier.[114]

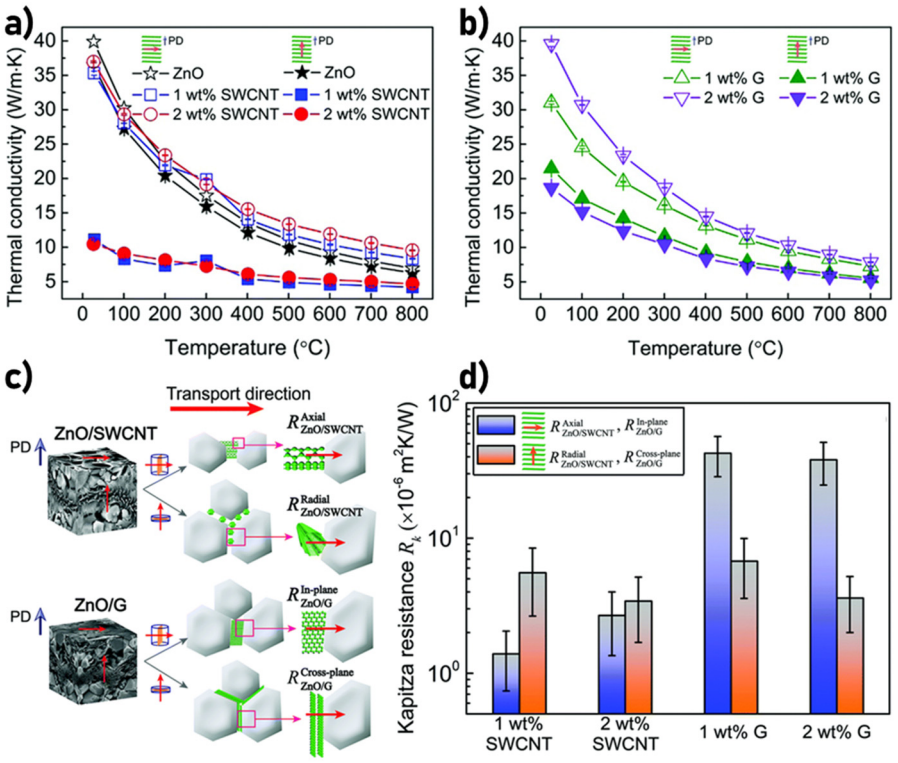

FIG. 14. Temperature-dependent thermal conductivity for (a) SWCNT/ZnO and (b) G/ZnO bulk nanocomposites with different pressing directions. (c) Illustration of the ZnO/carbon thermal interfaces for in-plane and cross-sectional thermal conductivity measurement directions. (d) Interfacial thermal (Kapitza) resistance for the ZnO/SWCNT and ZnO/G interfaces derived from the thermal conductivity measured for in-plane (blue bar) and cross-sectional (orange bar) transport directions. Reprinted from Liang *et al.*, J. Mater. Chem. C **7**, 1208–1221 (2019). Copyright 2019, with permission from the Royal Society of Chemistry.[161]

the significant reduction in lattice thermal conductivity observed in carbon-composited thermoelectric and metallic materials.

Li *et al.* adopted phonon-mismatch analysis in their work on nano-graphene Cu_2Se composites to explain the significant reduction in lattice thermal conductivity over pure Cu_2Se (Fig. 16).[48] As revealed by inelastic neutron spectroscopy, the thermoelectric phase has most of its available vibrational states at low energies (frequencies); below 30 meV (~7 THz). In contrast, graphene has phonon modes extending beyond 100 meV (~24 THz). Because the PDOS overlap between these materials is very low at low energies, the primary heat-transporting modes in Cu_2Se, which exist at low energies (acoustic phonons), have a low transmission probability through the Cu_2Se–graphene interface. The resulting composites exhibit values of κ_{total} that are ~1/3 of the pure matrix value. A similar analysis was performed by Zhou *et al.*,

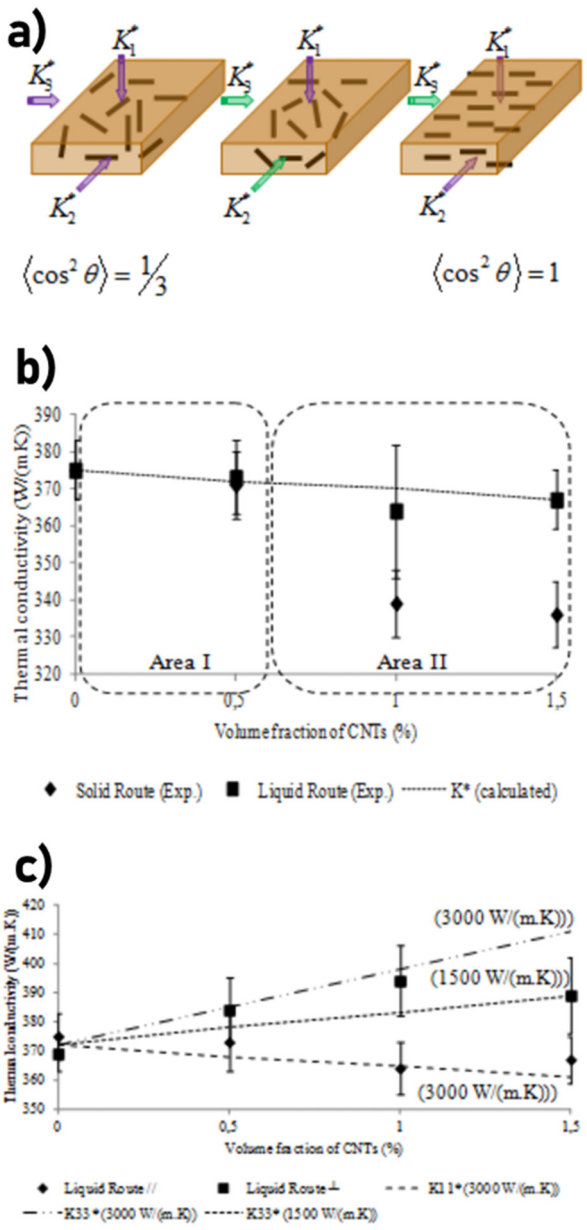

FIG. 15. (a) Schematic demonstrating various particle orientations and corresponding geometric terms. (b) Measured thermal conductivities of Cu–CNTs composite materials parallel to the pressing direction and predicted thermal conductivities for $\langle \cos^2\theta \rangle = 1/3$. (c) Thermal conductivity of Cu–CNTs composite materials in the direction parallel [liquid route (para)] and perpendicular [liquid route (perp)] to the axis of compression and predicted results (K_{11}^* and K_{33}^*) for $\langle \cos^2\theta \rangle = 1$ and $\kappa_{CNT} = 3000\ W\ m^{-1}\ K^{-1}$ and $\kappa_{CNT} = 1500\ W\ m^{-1}\ K^{-1}$. Reprinted from Universal Vallet *et al.*, J. Mater. Sci. **3**, 55—61 (2015). Copyright 2015, with permission from Horizon Publishing (CC-BY).[162]

extending the strategy to composites containing multiple compounds of Cu_2Se, BiPbCaCuSeO, and graphene (Cu_2Se-BPCCSO-GR).[163] The optimization among the three compounds not only enhanced the electric properties but also further reduced the thermal conductivity to the

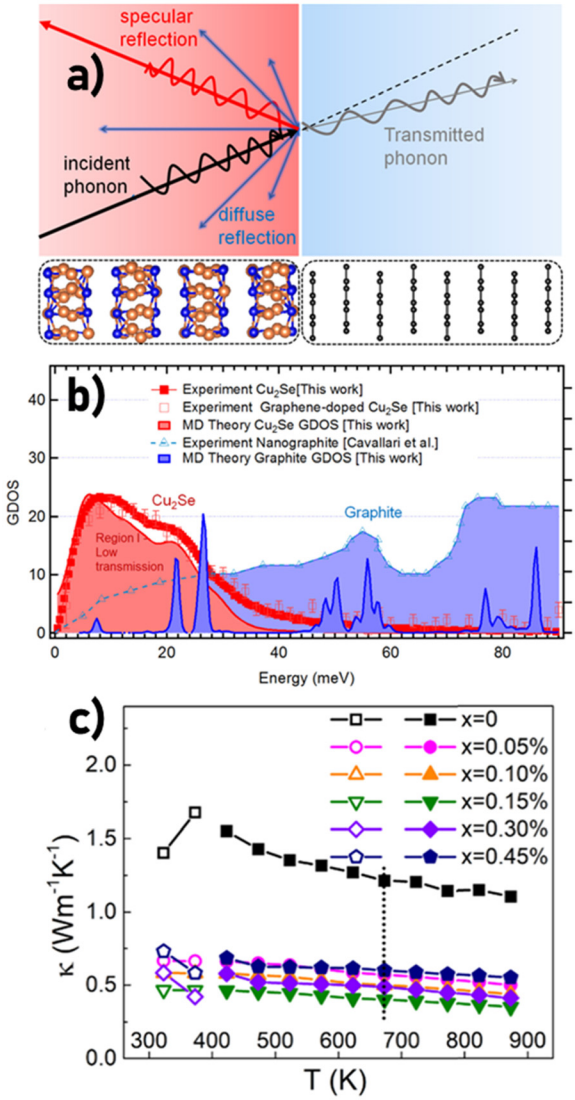

FIG. 16. (a) Schematic illustration of two different scattering processes: specular reflection and diffuse scattering, for a phonon at the Cu_2Se/C interface. (b) The density of states of Cu_2Se measured via a neutron spectroscopy experiment at 550 K and calculated with *ab initio* molecular dynamics. (c) Thermal conductivity of Cu_2Se and its nano-graphene composites. Reprinted from Li *et al.*, Nano Energy **53**, 993–1002 (2018). Copyright 2018, with permission from Elsevier.[48]

level of $0.11\ W\ m^{-1}\ K^{-1}$, resulting in a record high performance amongst thermoelectric materials. The significant reduction of the thermal conductivity results from the strong phonon scattering due to multiple interfaces and large phonon mismatch of the composites. The latter was further corroborated by the small overlapping factor of the phonon density of states. Of the three-compound composites, Cu_2Se-BPCCSO-GR has the lowest overlapping factor as compared to the corresponding two-compound composites of Cu_2Se-GR and BPCCSO-GR.

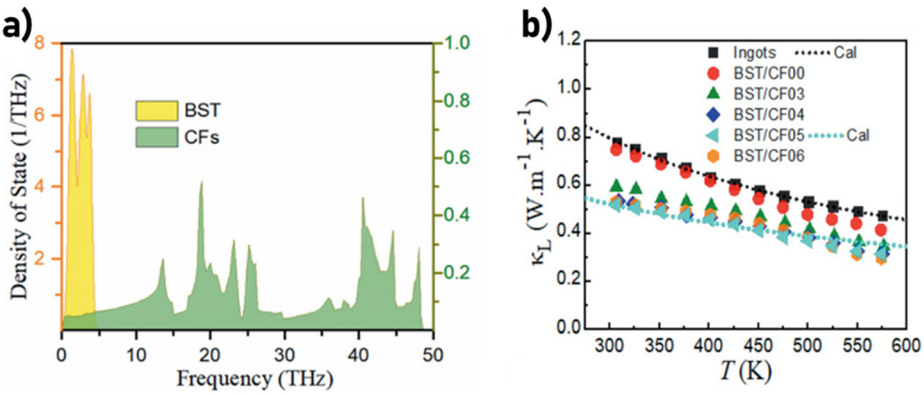

FIG. 17. (a) The phonon mismatch between BST and carbon fibers calculated via DFT. (b) The lattice thermal conductivity of the different BST/CF samples. Reprinted from Yang *et al.*, Adv. Funct. Mater. **31**, 12 (2021). Copyright 2021, with permission from John Wiley and Sons.[164]

Yang *et al.* also used the phonon-mismatch approach to analyze the thermal conductivity of their carbon–fiber Bi–Sb–Te (BST) composites (Fig. 17).[164] As shown in Fig. 17(b), with the addition of carbon fiber, the lattice thermal conductivity of the composites decreases significantly. Similar to the Cu_2Se–graphene system, BST exhibits a large phonon density of states below 5 THz (20 meV), while CF has a very low phonon density of states below 5 THz [Fig. 17(a)], indicating a low probability of transmission for phonons below 5 THz according to the DMM model. Above 5 THz, the phonon density of states of the CFs is still widely distributed, whereas that of BST is negligible, indicating transmission of high-energy phonons will be forbidden if a direct one-phonon process is assumed. The low probability of phonon transmission leads to the large interfacial thermal resistance between CF–BST interfaces, thereby suppressing the heat conduction in BST/CF composites. Utilizing the AMM and DMM models, values of thermal boundary resistance, R_K were calculated to be 1.4×10^{-6} and 1.2×10^{-6} m^2 K W^{-1}, respectively.

Non-equilibrium molecular dynamics simulations were used by Wang *et al.* to model how the interfacial thermal conductivity (ITC—inversely proportional to R_K) changes in a Cu–CNT composite with the addition of various metal additives at the CNT surface (Fig. 18).[165] It was found that a few layers of Co and Ti atoms significantly enhanced the ITC across the Cu–CNT interface, while Au and Ag both decrease the ITC. The results were understood in two paradigms. First, the ITC is proportional to the metal–CNT bond strength. Cu itself bonds relatively weakly to carbon (nanotubes) through physisorption, leading to a high thermal barrier. While Ag and Au bond to carbon slightly more strongly—also by physisorption—the extra thermal barrier that their presence creates at the Cu–Ag or Cu–Au interface is larger than any increase in ITC at the Ag–CNT or Au–CNT interface. Co and Ti, on the other hand, have a much stronger bonding with carbon by chemisorption and also with Cu itself. This results in more effective thermal transport at the Cu–Co or Cu–Ti interface and the Co–CNT or Ti–CNT interface. Second, the PDOS was calculated for each material and the PDOS overlap, S, calculated, in accordance with the DMM.[124] The calculated values for S follow the same series as the metal–C chemical bonding strength and ITC: Co > Ti > Cu > Ag > Au.[165] This work demonstrates the potential for ITC (R_K) engineering for both TEC and MMC applications and provides a helpful quantitative description of the ITC in carbon–metallic systems.

The results from several studies, as discussed above, show that the diffuse mismatch model (DMM) is a helpful tool to explain the large thermal boundary resistance in carbon composites. Providing an estimate for R_K from a theoretical point of view can greatly enhance the understanding of the ETC in composite systems when combined with models, which contain a thermal boundary term. In most carbon (nano)materials, highly dispersive phonon modes arising from strong C–C bonding and light C atoms result in a large density of phonon states at high energies. Comparatively, systems consisting of relatively heavier and weakly/anharmonically bonded atoms, such as TE materials and some metals, are weakly dispersive and are only able to sustain relatively low energy phonon modes. This analysis provides insight into the origin of large phonon scattering by various carbon dopants in many material systems. However, there is much work to be done in developing this theory to accurately predict the thermal conductivity of composites. For example, it is not yet obvious whether the differences in PDOS between various carbon dopants is significant enough to impact κ_L in a composite with the same host material. Additionally, as we explored in Sec. I C 2, it is not clear whether a large R_K can be considered as the primary origin of the significant reduction in κ_L exhibited by some composite systems. According to the models shown in Sec. I C, even infinitely large R_K can only have a limited effect for some particle configurations. Molecular dynamics simulations and neutron spectroscopy have proven to be useful probes for phonon modes in nanoparticles, bulk materials, and their composites, and we predict that further studies with these tools will provide great insight into relevant physical phenomena.

2. Surface treatment and functionalization

Various methods have been developed to functionalize or otherwise treat the surfaces of carbon nanomaterials in order to alter their surface thermal properties and improve their incorporation into the host matrix. This has been achieved via chemical, plasma, and electro-/mechanochemical procedures.[166–170] These methods can usually be separated into two categories: covalent and non-covalent functionalization.[155,156] Covalent functionalization is achieved by the direct addition of functional groups to the surface of the nanoparticles. Generally, this is an oxidation process involving heat treatment or exposure to acids, which cause the formation of carboxyl groups on the surface that can then be further chemically altered for the desired functional group. The structure of the carbon material is also often altered during covalent processing. For example, surface-modifying carbon nanotubes (CNTs) can cause many of the sp^2 hybridized bonds to transform into

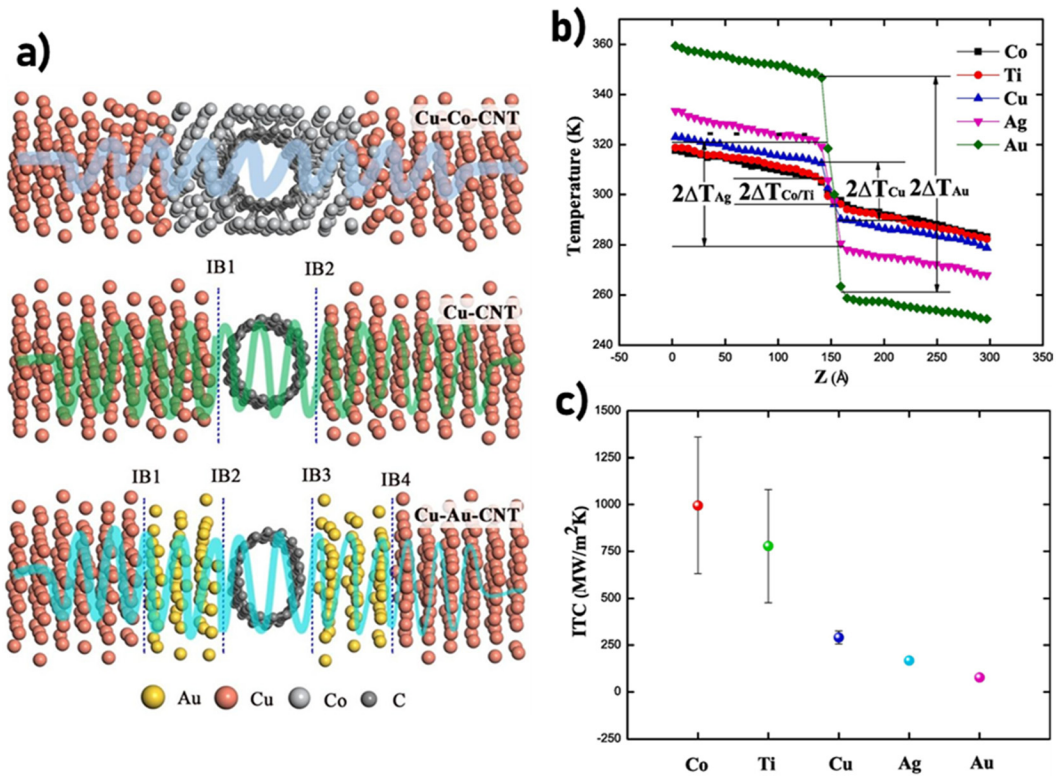

FIG. 18. (a) The dominant phonon transmission mechanism for Cu–Co–CNT, Cu–CNT, and Cu–Au–CNT interfaces and (b) the effect of metal additive on the temperature gradients for the Cu–M–CNT composites and the (c) ITC for the corresponding systems. Reprinted from Wang *et al.*, Chem. Phys. **542**, 111019 (2021). Copyright 2021, with permission from Elsevier.[165]

sp^3 bonds, resulting in many defects in the tubes. The main attraction of covalent functionalization is the superior dispersity of functionalized particles in polar solvents and thus the host matrix, reducing bundling and agglomeration.[156] Additionally, the C–matrix interfacial adhesion or bonding is also often improved. The latter is usually beneficial for MMCs and PMCs, but not necessarily beneficial for TECs as interfacial bonding strength is directly proportional to interfacial conductance. Non-covalent methods consist of the adsorption of organic or inorganic molecules (including chains) onto the surface of particles by non-covalent bonding, i.e., hydrogen bonding, π–π stacking, and electrostatic interactions. This is generally preferred over covalent bonding since it offers similar benefits to covalent functionalization while preserving the nanoparticle's condition. However, there is the risk of desorption because of the weaker non-covalent bonds involved and the interfacial bonding might not have the same magnitude of desired effect.[156] Here, we discuss relevant studies that have investigated the effect of functionalization on thermal transport in TECs and MMCs. We have included a discussion specifically on metal functionalized composites in Sec. II B 3.

In their study investigating CNT–Bi_2Te_3 composites for TE applications, Zhao *et al.* measured the effects of argon plasma treating CNTs before growing Bi_2Te_3 onto the CNT scaffold and then consolidating via SPS [Fig. 19(a)].[171] Their work shows that CNTs can be treated to significantly suppress the lattice ETC while leaving the electrical conductivity largely unaffected (Figs. 19(b) and 19(c)]. This "decoupling" of phonon and carrier transport leads to a ∼50% increase in the ZT compared to the untreated composite. The origin of reduced phonon transport in the Ar-plasma treated composite is rationalized by the amorphization of carbon and the creation of point defects on the CNT surfaces resulting from the Ar bombardment. The damaged CNTs cause a roughened CNT–Bi_2Te_3 interface, which strongly scatters mid-to-long wavelength phonons. This roughness results in diffuse phonon reflection at the interface. Transmitted phonons into the CNTs are also diffuse since the mean free path of phonons in amorphized carbon is on the atomic scale. With increasing treatment time, the CNTs are damaged more—at a decreasing rate—causing stronger scattering and further reducing the lattice thermal conductivity.

Acid treatment of CNTs is a form of covalent functionalization that has been investigated in CNT TECs and MMCs. Cho *et al.* studied the effects of acid treatment on CNTs aiming to increase the thermal conductivity of Cu–CNT MMCs.[172] After finding the optimal ratio of acids and treatment time, they used H_2SO_4 and HNO_3 to functionalized MWCNTs and consolidated them with Cu via SPS after mixing the Cu and CNT powders in ethanol and drying. They show that the total ETC is greatest when using treated CNTs, with an increase in the thermal conductivity of the copper being achieved below 1 vol. %. The authors fitted a simple thermal conductivity model that does not consider

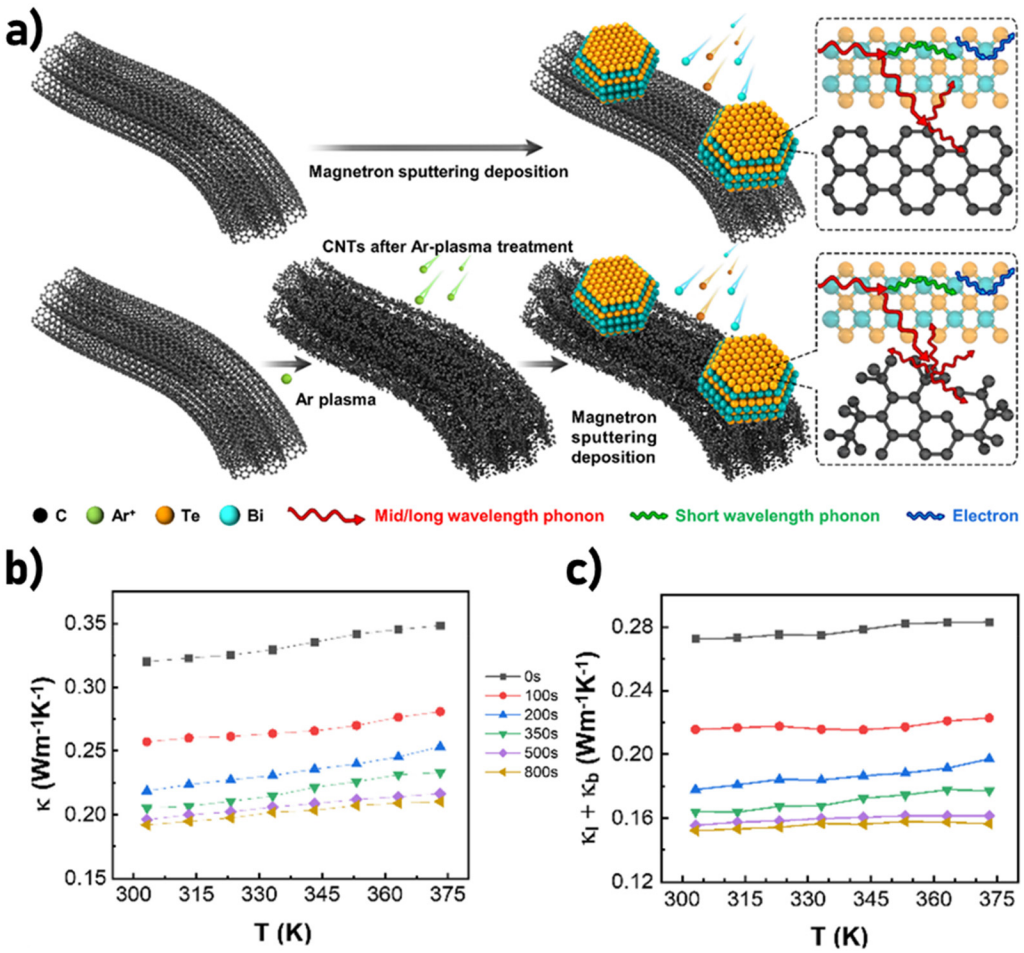

FIG. 19. (a) Illustration of the fabrication and structure of flexible Bi_2Te_3–CNT hybrids using an untreated CNTs scaffold and an Ar-plasma-treated CNTs scaffold. A high density of defects is generated on CNTs due to ion bombardment. (b) Total and (c) lattice + bipolar thermal conductivity for different plasma treatment times. Reprinted from Zhao *et al.*, Carbon **170**, 191–198 (2020). Copyright 2020, with permission from Elsevier.[171]

thermal interface resistance, assuming that this is negligible in this vol.% region [Fig. 20(a)] for these types of interfaces. The untreated CNTs cause a significant reduction in the total ETC at all volume percent and for the treated samples beyond ∼5 vol. %. The electron microscope images of their samples reveal that the untreated CNTs contain a few-nanometer-thick amorphous layer which, after consolidation, is incorporated into the Cu grain boundaries. The treated samples, however, have significantly reduced amorphized carbon on the surface, allowing them to form better contact with the Cu matrix, and the Cu grain boundaries are relatively clean. They propose a diffusion mechanism responsible for the inclusion of amorphous carbon into the Cu grain boundaries, which involves the oxygen atoms present from CuO on the surface of the powder [Fig. 20(b)]. The amorphous carbon acts as both an effective thermal interface in the grain boundary and increases the thermal interface resistance at the CNT–Cu interface. This could explain Kim *et al.*'s result for reduced lattice thermal conductivity for the weakly treated tubes compared to the strongly treated tubes if a similar mechanism is at play in their Bi_2Te_3–CNT composites.

Covalent functionalization with H_2SO_4 and HNO_3 is compared with non-covalent functionalization with polymer wrapping using cationic sodium polystyrene sulfonate (PSS) by Firkowska *et al.* in Cu–MWCNT MMCs,[173] and Pal and Sharma in Ag–MWCNT MMCs.[174] Both studies use very similar synthesis routes, with Firkowska *et al.* using SPS to sinter their powders, while Pal and Sharma use a horizontal tube furnace. Firkowska *et al.* found that both forms of functionalization improve the ETC of the composite compared to the as-received CNTs, particularly at higher weight percent, although an enhancement of the thermal conductivity over the pure Cu sample was not achieved in any of the composites [Fig. 21(a)].[173] Additional CNTs proved more and more detrimental to the ETC over the range of 0.2–10 wt. %. The authors use the model developed by Nan *et al.* [Eq. (3)] to calculate the Cu–CNT ETC and found that even using a Kapitza resistance an order of magnitude larger than is expected, the Cu–CNT

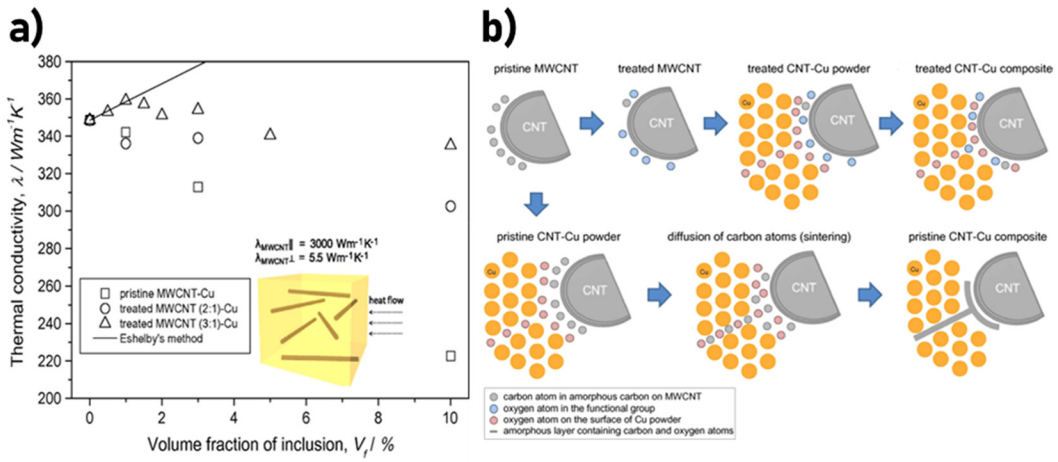

FIG. 20. (a) Thermal conductivities of MWCNT–Cu composites as a function of CNT content in a direction perpendicular to the compression axis. (b) Possible schematics of the interfacial characteristics of the treated MWCNT–Cu composite and amorphous layer formation in the pristine MWCNT–Cu composite. Reprinted from Cho *et al.*, Acta Mater. **60**, 726–736 (2012). Copyright 2012, with permission from Elsevier.[172]

composites have significantly lower ETC than calculated [Fig. 21(b)]. Pal and Sharma achieved starkly different results with Ag–CNT with PSS functionalized composites, achieving increasing thermal conductivity at 3 and 6 vol. % compared to the pure Ag sample [Fig. 21(c)].[174] Untreated SWCNT–Ag composites showed the next highest ETC, with slightly reduced values compared to pure Ag, where the ETC decreased further from 3 to 6 vol. %. The covalently functionalized CNTs showed the lowest ETC, which also reduced further from 3 to 6 vol. %. Pal and Sharma employed various versions of the model developed by Nan *et al.* [including Eq. (3)] and found that the PSS functionalized Ag–CNT composite fit the simplest form—which does not include interfacial thermal resistance—remarkably well [Fig. 21(d)]. The ETC of the other composites, however, fall well below the calculated values of the models including Kapitza resistance. They deduce that the non-covalently functionalized (via π–π stacking) CNTs with PSS assist in the transfer of heat from both phonons and electrons at the CNT–Ag interface. In contrast, it is thought that the more covalent nature of bonding between the CNT and Ag matrix that is achieved by covalent functionalization reduces the number of available electrons to transfer heat while the induced defects from the acid treatment reduce phonon propagation in the CNTs. The reduced ETC of the SWCNT composites is thought to arise predominantly from additional agglomeration, since the individual tubes should have higher intrinsic TC compared to both treated MWCNTs, and theoretically offer a better transfer of electronic thermal conductivity compared to the covalently treated MWCNTs. The temperature dependence of the ETC for each type of CNT composite shows markedly different behavior—indicating the dominance of different thermal transport mechanisms in each.

Overall, plasma treatment of CNTs shows great promise for the further reduction of ETC and increase in ZT in CNT composites by enhancing the CNT–matrix thermal barrier through amorphization of the outer tube, while retaining good electronic transport.[171] While this has only been achieved in magnetron-sputtered Bi_2Te_3, more conventional methods of dispersing carbon nanomaterials into the host, such as in solution, are also expected to benefit from plasma treatment. In particular, homogeneous dispersion of CNTs in solution can be achieved via the creation of polar functional groups on the outer CNT wall by oxygen and ammonia plasma treatment.[175] Acid treatment has been shown to reduce the amount of inherent amorphized carbon on the exterior of pristine CNTs and increase interfacial bonding, resulting in an increase in ETC in MMCs.[172] However, this enhancement of ETC is not a consistent result across studies using different synthesis techniques, even for the same host system.[173] Furthermore, it is thought that the increased covalency of bonding between the covalently functionalized CNTs and the metal matrix can result in reduced electronic thermal conductivity. This is consistent with results observed in TE Bi_2Te_3–CNT composites, where covalently functionalized CNT composites show lower total thermal conductivity but higher lattice thermal conductivity, compared to untreated (or weakly treated) CNT composites.[8,176] Non-covalent functionalization by polymer wrapping is a promising treatment method for enhancing the lattice thermal interface between CNTs and metal matrices, resulting in increased ETC.[174] However, this has only been realized in Ag and not Cu systems.[173,174] While these interfacial enhancements are solely detrimental to TECs, there is some promise for ETC enhancement in MMCs via covalent and non-covalent functionalization.

3. Alloying

The effect of alloying with various other metallic elements has also been investigated and is found to modify the thermal boundary resistance at the C-matrix interface.[177–184] This can take the form of coating the carbon nanomaterial with a metal different to the host before consolidation (e.g., by electrodeposition, chemical vapor deposition) as a form of non-covalent functionalization, or simply synthesizing an alloyed host. Typically, the presence of another metal is introduced to act as a thermal bridge between the carbon dopant and host matrix, increasing interfacial thermal conduction (ITC) (see Sec. II B 1). The most well studied matrix in this context is Cu, since it is

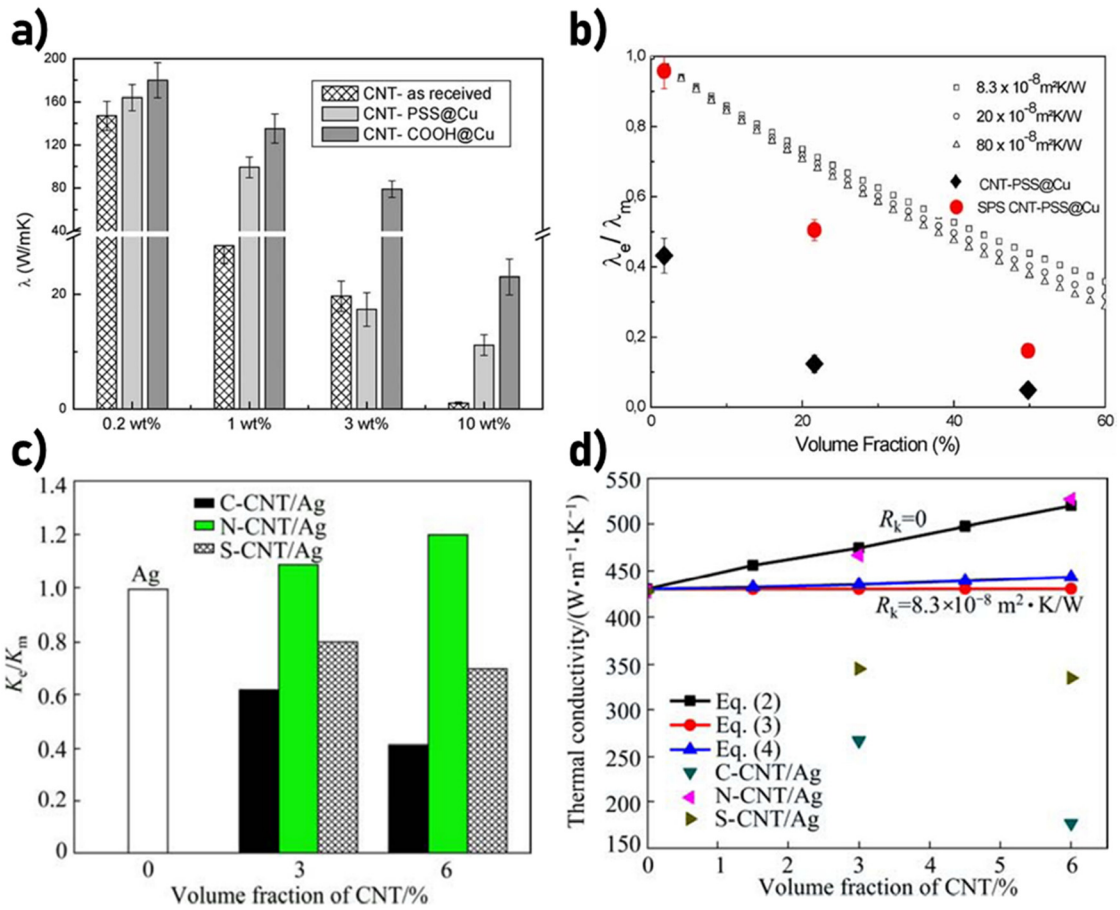

FIG. 21. Results from Firkowska *et al.* showing (a) a comparison of the effective thermal conductivities of CNT/Cu nanocomposites and (b) the normalized (to the host) thermal conductivities of the composites up to 50 vol. %, compared with an EMA with various interface resistance terms. Results from Pal and Sharma showing (c) a comparison of average normalized effective thermal conductivities of CNT/Ag nanocomposites with unreinforced Ag and (d) comparison between predictions given by various EMA models and experimental data for thermal conductivity of CNT/Ag composites as a function of CNT volume fraction. Reprinted from Firkowska *et al.*, Phys. Status Solidi B **248**, 2520–2523 (2011). Copyright 2011, with permission from John Wiley and Sons,[173] and Pal and Sharma, Trans. Nonferrous Metals Soc. China **25**, 154–161 (2015). Copyright 2015, with permission from Elsevier.[174]

not wettable with carbon and overall bonds very weakly to it.[185] Although few such studies have been conducted on TECs in an attempt to *decrease* the ITC, the results from MMC studies bring great insight and prospects for TEC and other composite systems.

Experimentally, various metals have been used to decorate carbon CNTs before incorporating them into metal matrices in order to enhance interfacial thermal conductivity, including Al, W, Mo, and Fe.[182,183,186,187] In all of these cases, the ETC of the composite with metalized CNTs increased compared to the host matrix (Cu in all cases) and the composites using un-treated CNTs. The significant increase in ETC in the metalized CNTs is primarily due to improved dispersion and the formation of metal (W, Al, Mo, Fe, etc.) carbides at the metalized CNT interface, which act as a thermal bridge, as described in Ref. 165.

Alternatively, simply alloying the matrix with carbide-forming elements can alter the thermal boundary between the CNT and the host. Chu *et al.* compared the ETC of CNT composites of pure Cu and Cu-Ti(0.85%) [Fig. 22(a)].[179] In their study, they show the clear formation of Ti carbide layers at the matrix–CNT interface, contributing to a significantly reduced CNT–matrix thermal interface resistance: $R_{K,Cu} = 8.4 \times 10^{-7}\,\mathrm{m^2\ K\ W^{-1}} \rightarrow R_{K,Cu-Ti} = 6.5 \times 10^{-8}\,\mathrm{m^2\ K\ W^{-1}}$, calculated using the model developed by Nan *et al.* [Eq. (3)] [Fig. 22(b)]. The formation of TiC is shown to be thermodynamically spontaneous with a Gibbs free energy of −157.6 kJ/mol at a sintering temperature of 1053 K. Additionally, defects such as unstable dangling bonds on the CNT surfaces caused by milling and surface treatment are highly reactive and are more likely to form carbides. Similar results have been achieved in Cu–W[184] and Cu–Cr[188] CNT composites, by the formation of W–carbides and Cr–carbides, respectively.

Both the dispersion of CNTs into a metal host and the interface of the metal host matrix with CNTs can be improved with the thoughtful addition of other metals, either by pre-coating the CNTs or by alloying the host. In particular, carbide-forming elements significantly improve the thermal interface in Cu–CNT composites through

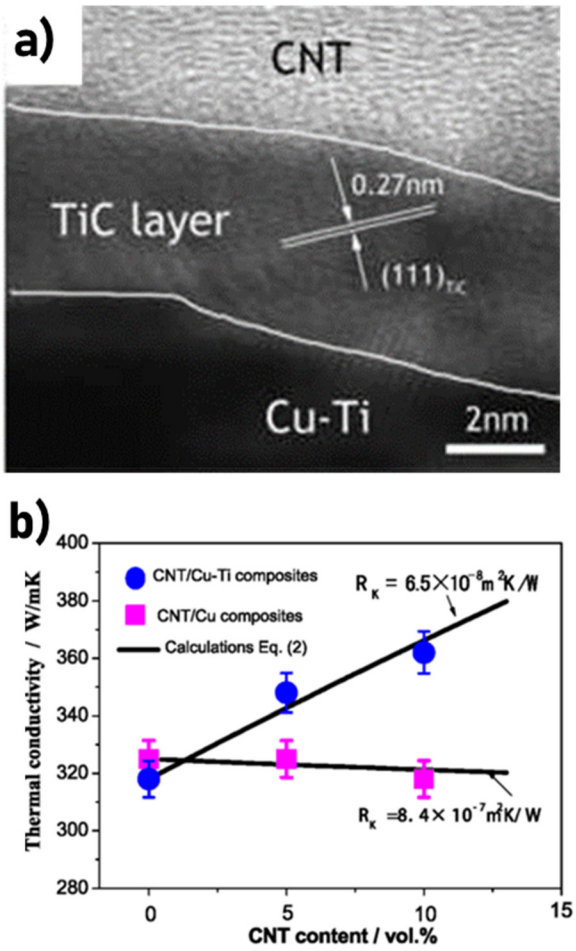

FIG. 22. (a) HRTEM image of the interface in CNT/Cu–Ti composites. (b) Thermal conductivity measurements and predictions of CNT/Cu–Ti and CNT/Cu composites vs CNT content. Reprinted from Chu *et al.*, Appl. Phys. A: Mater. Sci. Process. **110**, 269–273 (2012). Copyright 2012, with permission from Springer Nature.[179]

the formation of carbide layers, which act as a thermal bridge between Cu and CNTs.[179,184,188] It has been shown by simulation that the opposite effect can occur by choosing a coating element that bonds even more poorly to the CNT than the host, increasing the CNT–host interfacial thermal resistance.[165] As far as we are aware, no such study has been conducted for a TEC, and we encourage this as an avenue for exploration. Yuan *et al.* did incorporate CNTs into a Cu–Ni alloy (constantan) to reduce thermal conductivity for thermoelectric applications.[189] They showed a significant reduction in the thermal conductivity of the composite due to the large formation of CNT aggregates, pores, and Cu/Ni–CNT interfaces. Although the physical properties demonstrated in their work are promising, the presence of Ni on the Cu/Ni–CNT interface was not detected directly, and it would have been beneficial to have high-resolution transmission electron microscope images of the CNT–host interface. For the desired effect of a layer of Ni acting as an additional thermal barrier between the host and the CNTs, the Ni would possibly need to be pre-coated onto the CNTs before sintering.

C. Induced host phonon scattering mechanisms

1. Porosity

The addition of carbon nanoparticles (NPs) can also cause the formation of additional pores during the sintering process, which act as additional scattering sites for phonons.[189] The thermal conductivity of porous materials has been studied for various applications such as for integrated circuits, sensors, solar cells, photoluminescence, and, of course, thermoelectrics.[190,191] The degree of thermal conductivity reduction from pores depends on multiple factors including the number of pores, their size (and size distribution), and shape—factors, which also affect thermoelectric performance due to their influence on electronic transport (i.e., power factor).[191,192] For TE applications, the impact of porosity on the electronic transport needs to be carefully considered.

Yuan *et al.* studied Cu–Ni (constantan) alloys doped with CNTs and Se (CNT/$Cu_{55}Ni_{45}Se$) for thermoelectric applications and achieved a significant reduction of the composite lattice thermal conductivity due to the large CNT–matrix interface resistance, significant agglomeration of CNTs, and the resulting porous structure.[189] A large number of nanoscale pores (50–150 nm) were observed in SEM images at fractured sites, with the porosity of the spark plasma sintered product increasing from 2% to 14% with 0–3 wt. % CNT addition, respectively. Additional porosity originates from the hollow structure of the CNTs themselves (2 nm diameter) and the highly agglomerated SWCNTs. The resulting total thermal conductivity decreased from $\kappa_{tot} \approx 45\,W\,m^{-1}\,K^{-1}$ for the pure sample to κ_{tot} (ETC) $\approx 5\,W\,m^{-1}\,K^{-1}$ for the 3 wt. % CNT composite at high temperatures (800–900 K), with similarly sized contributions coming from both the electronic and lattice components.

Tang *et al.* demonstrated ultralow thermal conductivity in the thermoelectric ceramic $Ca_3Co_4O_{9+\delta}$ (CCO) by the addition of CNTs, also resulting in a porous structure.[77] Their pure CCO sample demonstrated a k_{tot} value of $3.14\,W\,m^{-1}\,K^{-1}$ at room temperature while the 6 wt. % CNT composite fell just below the disordered crystal limit proposed by Cahill ($0.319\,W\,m^{-1}\,K^{-1}$) with $\kappa_{tot} = 0.3\,W\,m^{-1}\,K^{-1}$. It is believed that this 91% reduction in thermal conductivity is due to a wide range of phonon scattering mechanisms caused by the CNTs and nanopores since the charge contribution to κ_{tot} is thought to be <1%. To make their composites, they used a combination of regular CNTs and helical/chiral CNTs. Interestingly, they showed that the helical CNTs created significantly more nanoscale voids at the CNT–CCO boundary. The influence of pores on thermal conductivity has also been recognized by Zhang *et al.* in TE Bi_2Te_3 composited with CNTs.[193] They used cryogenic grinding of the composite (CNT and Bi_2Te_3) powders before SPS. Cryogenic grinding significantly improves the dispersion of the CNTs into the matrix by truncating them and no agglomeration is seen in the composite samples. Additionally, the grain sizes are significantly reduced and pores on the order of 10–100 nm are formed due to both the cryogenic grinding and the presence of CNTs during sintering (Fig. 23). The total thermal conductivity is reduced from $\kappa_{tot} = 1.14\,W\,m^{-1}\,K^{-1}$ for the pure Bi_2Te_3 sample to a minimum of $\kappa_{tot} = 0.32\,W\,m^{-1}\,K^{-1}$ at 475 K for the 3 vol. % CNT composite, with the majority of κ_{tot} coming from the lattice component.

Highly porous $Bi_2Te_{2.7}Se_{0.3}$–CNT composites have been synthesized by Li *et al.* via a novel sacrificial template method, which

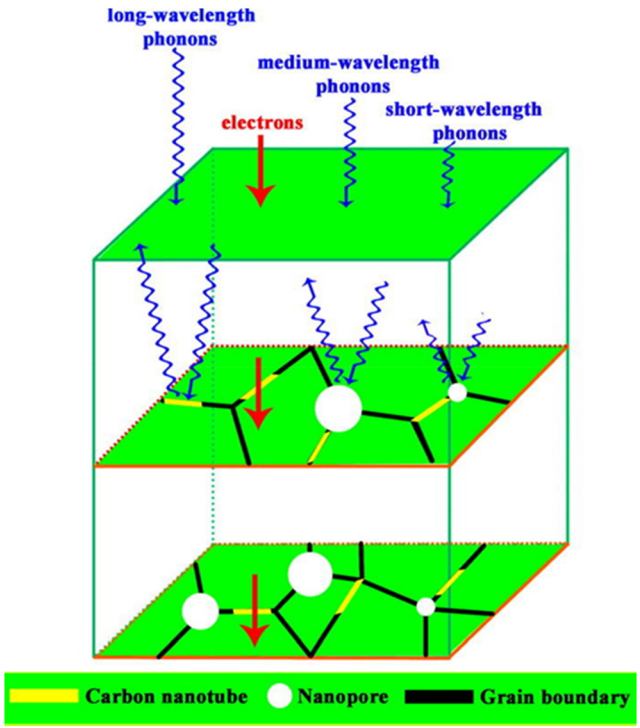

FIG. 23. Schematic drawing of the CNT/Bi_2Te_3 composites with nanopores in different sizes shows the strong scattering of phonons with multiscale mean free paths along with the benefit to electron transport. Reprinted from Zhang *et al.*, J. Appl. Phys. **121**, 055104 (2017). Copyright 2017, with permission from AIP Publishing.[193]

significantly reduces thermal conductivity while leaving charge carrier transport relatively unaffected.[194] Instead of using traditional MW or SW CNTs, Li *et al.* demonstrated a unique synthesis technique for CNT composites, which involves coating Te nanowires with carbon through a hydrothermal process with glucose. During consolidation via SPS, the Te is liquefied and penetrates the porous CNTs and creates a new, few-layer BTS–CNT interface [Fig. 24(a)]. The result is a BTS–CNT composite with highly dispersed, straight, porous, amorphous CNTs with a layer of BTS on the CNT surface, which allows for enhanced charge transfer and mobility. Additionally, high-density and uniform nanopores are located throughout the BTS grains, originating from the expulsion of Te from the nanowires. Two different composite series were synthesized to compare the effect of the BTS/CNT interface/microstructure on the TE properties. The primary samples were made with 60–100 nm diameter CNTs (1.5–5% weight or volume—not specified) and are labeled BTS/CNT1. A secondary set, for reference, was made with a CNT with a diameter ≈10 nm. To understand the role of the nanopores on the lattice thermal conductivity, the authors of the study employed an effective medium theory (EMT) model, which considers the shape, diameter, and number of pores [Fig. 24(b)]. The EMT model significantly overestimates the BTS/CNT1 composite lattice thermal conductivity, which has a minimum of $\kappa_L = 0.19\,\mathrm{W\,m^{-1}\,K^{-1}}$ for the 4% CNT sample—lower than the estimated Debye–Cahill minimum. This is rationalized by the hierarchical scattering of phonons by the sub-nano-BTS layer and the amorphous carbon wall, in addition to the considered pores, which are on the scale of approximately 5, 10, and 60–100 nm, respectively. The values for κ_L for the BTS–CNT2 samples with ultrathin CNTs are relatively well predicted by the EMT model (besides the 1.5% sample, which is shown to have more large pores), suggesting that κ_L is dominated by phonon scattering by the nanopores due to the change in microstructure and morphology compared to the composites with larger CNTs.

In summary, the promotion of the formation of nanopores by carbon NPs during sintering—deliberate or accidental—can provide a significant reduction in lattice thermal conductivity through the hierarchical scattering of low to medium wavelength phonons.[77,189,193,194] While these pores also deleteriously affect charge transport, such reduction in electronic conductivity can be minimized if the incorporated NPs significantly benefit charge transport.[189,193,194] Further studies that explore the formation of pores with various carbon NPs and matrix combinations and synthetic techniques combined with modeling of the thermal conductivity would be greatly beneficial for the development of TE and other carbon NP composites.

2. Grain boundaries

As previously mentioned, grain boundaries can act as effective, frequency-independent, phonon scatterers. The thermal resistance of a grain boundary can be considered by its Kapitza resistance, R_K, and effective grain size, d_{eff}, as follows:[195]

$$\kappa_{poly}{}^{-1} = \kappa_{bulk}{}^{-1} + \frac{R_K}{d_{eff}}, \tag{19}$$

where $\kappa_{poly}{}^{-1}$ is the thermal resistance of the polycrystalline sample and $\kappa_{bulk}{}^{-1}$ is the bulk thermal resistance (i.e., single crystal/grain resistance). Carbon NPs are typically found to agglomerate at, or coat, grain boundaries during sintering and densification.[68,75,196] For this reason, phenomenological models have been developed, which consider the *coupled* grain boundary and NP–host boundary resistance. By doing so, an effective R_K value can be obtained that is primarily due to the carbon–host interface resistance but also includes contributions from the grain boundary and other phonon-scattering defects. While this effective R_K provides less specific information about the NP–host interaction, it provides a helpful picture of the effective thermal resistance introduced by the nanoparticles, which can be compared to other host–dopant systems.

To suppress thermal conductivity in n-type ($Yb_yCo_4Sb_{12}$) and p-type ($Ce_yFe_3CoSb_{12}$) skutterudites, Zong *et al.* incorporated reduced graphene oxide (rGO).[75] In their work, they suggest that the rGO effectively wrapped the grains of the skutterudite, as depicted in Fig. 25(a). By deducing the average grain size (d_{eff}) and thermal conductivity of their pure samples, they were able to fit effective grain R_K values of $3.8 \times 10^{-7}\,\mathrm{m^2\,K\,W^{-1}}$ for both of their n- and p-type skutterudites with ∼20% uncertainty. After compositing with rGO, the authors used a parallel conductance model to calculate the effective thermal resistance of the grains with rGO, giving significantly increased values of $R_K = 1.7 \times 10^{-6}\,\mathrm{m^2\,K\,W^{-1}}$ and $R_K = 1.1 \times 10^{-6}\,\mathrm{m^2\,K\,W^{-1}}$ for the n- and p-type composites, respectively, as shown in Figs. 25(b) and 25(c) ($\kappa_g{}^{-1}$ is the in-plane thermal resistance of the rGO). Without further deconvolution of the contributions to the thermal resistance, it is not possible to differentiate the origin of the different values of R_K for these two composites, i.e., it cannot be understood whether the difference originates because of their different

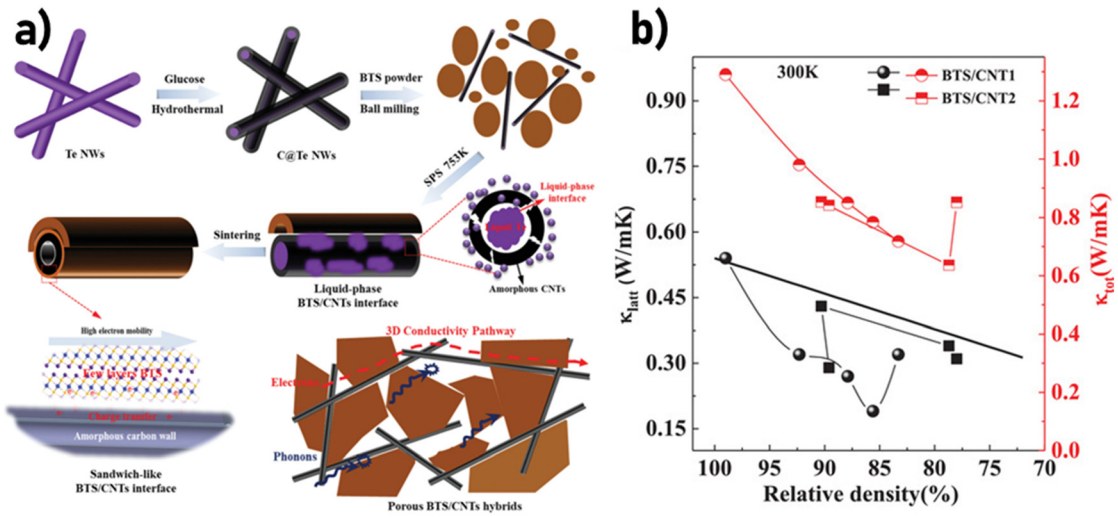

FIG. 24. (a) Fabrication process and formation mechanism of BTS/CNT porous hybrid bulk. (b) Total and lattice thermal conductivity dependence on the relative density of the porous BTS/CNT1 and BTS/CNT2 hybrids at 300 K. Reprinted from Li *et al.*, Adv. Electron. Mater. **6**, 2000292 (2020). Copyright 2020, with permission from John Wiley and Sons.[194]

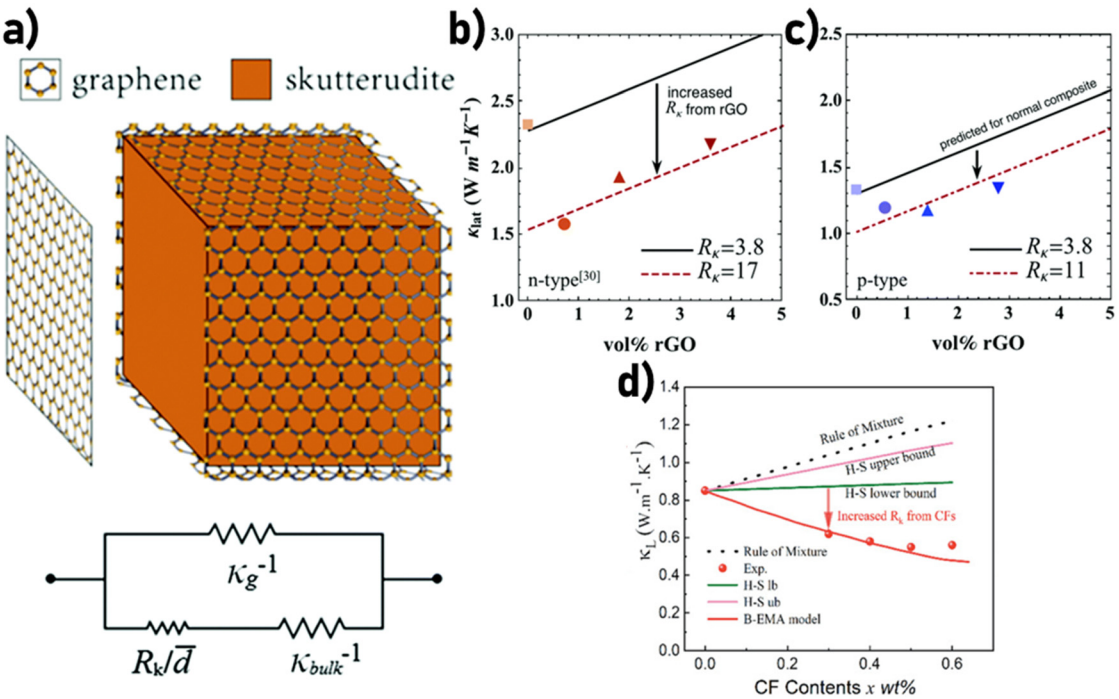

FIG. 25. (a) Diagram of the thermal circuit representing the thermal resistance of grain boundaries wrapped in graphene with the resistance elements labeled by their respective thermal resistivities. Lattice thermal conductivity (κ_L) at 300 K with varying amounts of rGO for both (b) n- and (c) p-type skutterudite/rGO composites. Upon the introduction of rGO, κ_L was predicted via the thermal circuit model and κ_L (dashed lines) was calculated via the thermal circuit model with fitted R_K values. (d) Lattice thermal conductivity of BST at 300 K with varying amounts of CF content. The thermal conductivities are predicted by the "rule of mixtures" model, Hashin–Shtrikman bound model ("H–S lb" and "H–S ub"), and Bruggeman's asymmetric model (B-EMA) taking into account interfacial thermal resistance between CFs and BST. Reprinted from Zong *et al.*, Energy Environ. Sci. **10**, 183–191 (2017). Copyright 2017, with permission from the Royal Society of Chemistry,[75] and from Yang *et al.*, Adv. Funct. Mater. **31**, 12 (2021). Copyright 2021, with permission from John Wiley and Sons.[164]

phonon DOS of the two materials, because different defects are produced during synthesis, or some other reason. Yang *et al.* took a similar approach in their work on carbon fiber (CF) doped bismuth antinomy telluride (BST) composites, where BST grain boundaries were observed to be highly decorated with CFs.[164] They calculated the grain boundary resistance for their pure BST sample to be $R_K = 6.17 \times 10^7\,\mathrm{m^2\,K\,W^{-1}}$ and then used an effective medium approach (Bruggeman's asymmetric model) to obtain the effective boundary resistance (including CFs) of $R_K = 2.2 \times 10^6\,\mathrm{m^2\,K\,W^{-1}}$, which is only ~15% larger than the sum of the R_K values of the grains and the CF–BST interface ($R_K \cong 1.3 \times 10^6$) as calculated using the acoustic and diffuse mismatch models [Fig. 25(d)]. We note that we were unable to reproduce the B-EMA values reported (see our discussion in Sec. I C 2).

As well as increasing the effective resistance across grain boundaries, carbon NPs have also been shown in many works, including those just discussed, to effectively suppress grain growth, resulting in composites with high densities of nano-sized grains. For example, carbon (quantum) dots (CDs) were used as a dispersant to enhance the thermoelectric performance of liquid-like Cu_2Se materials in a work by Hu *et al.*[53] The Cu_2Se/CDs hybrid materials were fabricated by hydrothermal synthesis followed by hot pressing. Figure 26(a) shows a high-magnification image of CDs at grain boundaries, where the areas in the circle of white spots are CDs surrounded by Cu_2Se nano-grains. This indicates that the grain size of Cu_2Se is greatly suppressed because the CDs can act as nucleation centers and suppress the recrystallization of Cu_2Se. As a result, the phonon thermal conductivity shown in Fig. 26(b) is greatly reduced due to the newly formed interfaces between the CD dispersant and Cu_2Se matrix and overall reduced grain sizes.

3. Atomic disorder and strain

Strain fields introduced into lattices by point defects, dislocations, or other defects in the crystal lattice have unique scattering potentials, which tend to scatter mid-frequency phonons. Ordinarily, any carbon dopant will cause some degree of stress or atomic disorder at the interface of the dopant and the host. However, this can be enhanced by choosing specific synthesis methods.

Min *et al.* reported the thermal properties of nanodiamond-dispersed $Bi_2Te_{2.7}Se_{0.3}$ composites (BTSe/ND), which are fabricated by high-energy mechanical alloying.[197] As shown in Fig. 27(a), with the addition of ND powders, the total thermal conductivity of the composite increases (due to the increase in electrical conductivity), while the lattice thermal conductivity decreases. Figures 27(b) and 27(c) show TEM images of the interfaces between the BTSe and NDs in the composites and an atomically disordered lattice at the BTSe/ND interface, which is different from the ordered lattice of the BTSe matrix is observed. It is suspected that the interfacial defect region was the result of the high-energy mechanical alloying with the NDs. The large density of extrinsic interfacial regions created between the BTSe matrix and NDs results in strong phonon scattering, thereby reducing the κ_L of the composites.

Similar results were reported for polycrystalline p-type bismuth telluride,[68] from which an additional reduction in κ_L is achieved by incorporating NDs into BiSbTe (BST) alloys [Fig. 28(a)]. The TEM characterization [Fig. 28(b)] suggests that dispersed NDs generate locally concentrated-strain fields in the matrix, leading to the generation of point-defect clustered zones (PDZs) around the ND/BST interface. The addition of the NDs not only causes the interfacial defect regions of the matrix but also modifies the grain size and orientation.

4. Multi-scale hierarchical structures

We have seen that the inclusion of carbon NPs into thermoelectric materials results in strong phonon scattering from not only the particles themselves but also the significantly altered microstructure of the host material due to the compositing process. This is summarized nicely by the transmission electron microscope images taken by Yang *et al.* of the multi-featured micro-structuring of their carbon microfiber–BiTeSe composites (Figs. 29(a) and 29(f)].[198] The composites show significantly reduced lattice thermal conductivity due to phonon scattering at multi-scale boundaries and the considerable interfacial thermal resistance arising from phonon mismatch between the constituent phases. Through STEM analysis, a wide range of microstructural features in the BTS/CF samples were observed, such as refined micron or sub-micron multi-grains (BTS), fine-scale nanometer to micrometer length carbon particles, nanoscale oxide precipitates, amorphous–crystalline heterophase (C/BTS) interfaces, and crystalline–crystalline heterophase interfaces (Bi_2O_3/BTS). Microstructures with at least (but certainly not limited to) some combination of these features are common to TECs synthesized by standard mixing and sintering methods

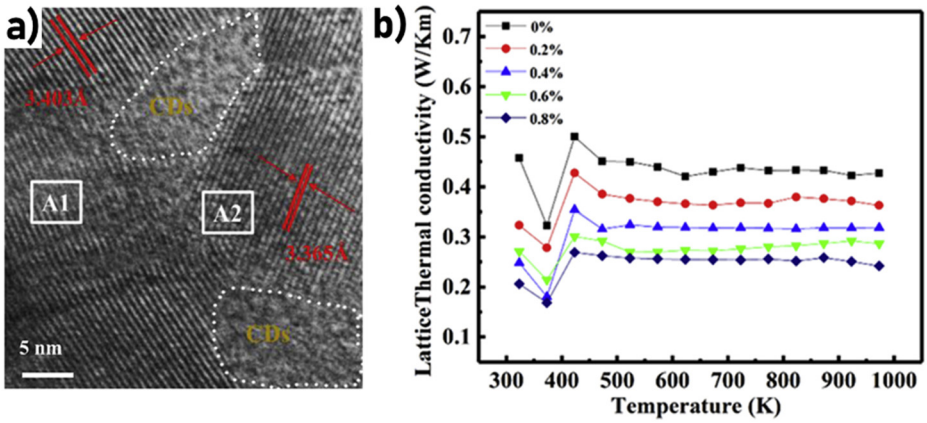

FIG. 26. (a) High-magnification image of CDs at Cu_2Se grain boundaries. (b) Temperature-dependent lattice thermal conductivity of Cu_2Se/x wt.% CDs samples. Reprinted from Hu *et al.*, J. Alloys Compd. **813**, 152204 (2020). Copyright 2020, with permission from Elsevier.[53]

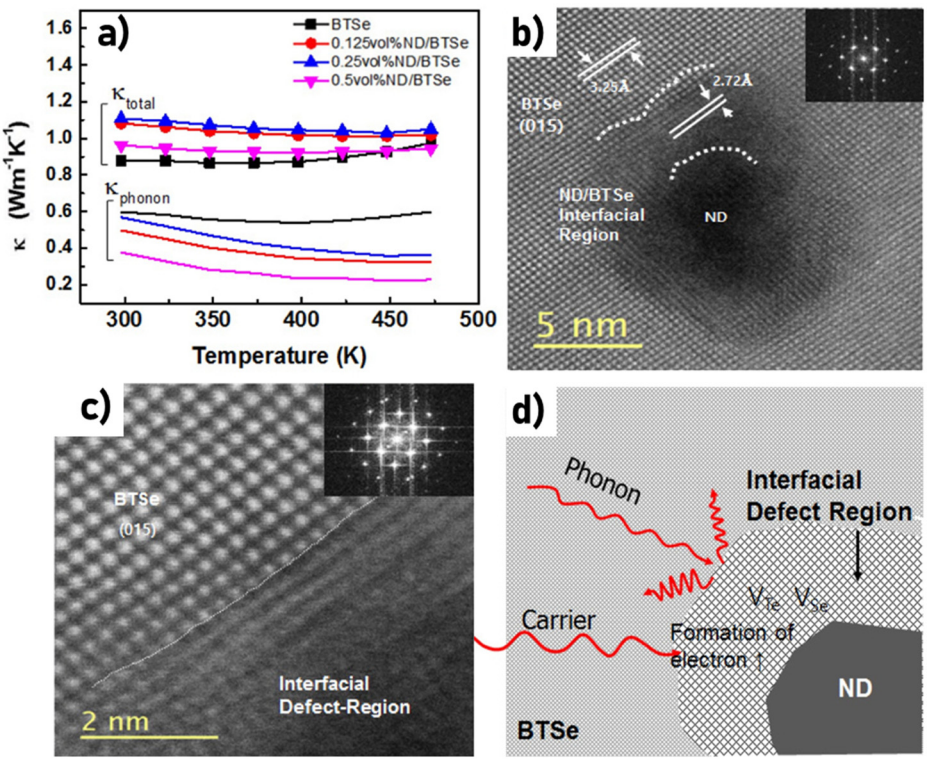

FIG. 27. (a) Thermal conductivity for BTSe with x vol% ND contents (x = 0.0, 0.125, 0.25, 0.5). (b) HR-STEM image showing the interfacial region and (c) HR-TEM images indicating the atomically disordered interface between the BTSe matrix and ND. The inset in (b) and (c) shows reduced FFTs of the BTSe matrix and interfacial region, respectively. (d) A conceptual illustration of the newly formed interfacial-defect region. Reprinted from Min *et al.*, Appl. Surf. Sci. **415**, 109–113 (2017). Copyright 2017, with permission from Elsevier.[197]

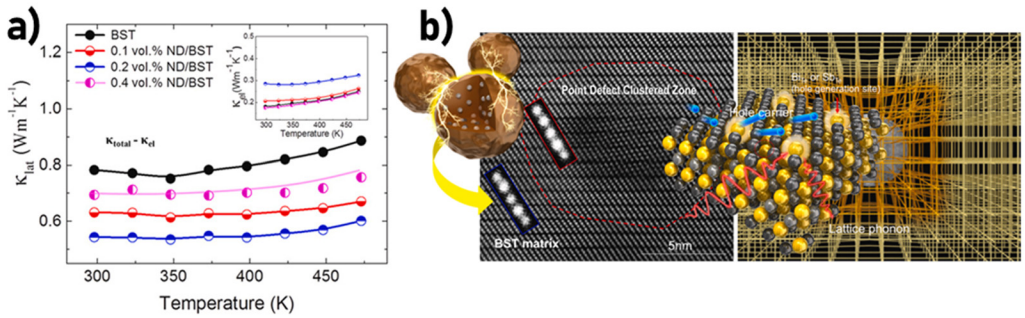

FIG. 28. (a) Comparison of the contributions by the lattice thermal conductivity in BST and ND/BST composites. (Inset shows the electronic contribution calculated from $L\sigma T$, where L is the Lorentz number, σ is electrical conductivity, and T is the temperature.). (b) The conceptual illustration of a strained point defect clustered zone induced by the addition of carbon nanodiamond. Reprinted from Kim *et al.*, Nano Energy **55**, 486–493 (2019). Copyright 2019, with permission from Elsevier.[68]

outlined throughout this article. This highlights the multi-faceted nature of the wide-spectrum suppression of phonon transport by compositing thermoelectric materials with carbon NPs.

D. Comparing carbon nanoparticle dopants

1. Different carbon nanoparticles in the same host matrix

We have presented and analyzed the results of many combinations of carbon nanoparticle additives (NP) and host matrices. However, very few of these studies compare different additives to the same host in a systematic way. Based on the thermal transport theory that we have presented, the type of carbon NP should have a significant impact on the resulting composite lattice thermal conductivity. For example, the intrinsic thermal conductivity of carbon nanoparticles varies over orders of magnitude, and interfacial thermal resistance between different NPs and hosts differs since the phonon density of states of carbon NPs vary significantly, as does their surface chemistry. Additionally, the nature of the carbon NP will affect how it is dispersed into the host material and can affect the final microstructure, given a particular synthesis route, both of which significantly impact the lattice thermal conductivity. In this section, we present of this review, we present a few thermoelectric composite (TEC) works that compare the effects of doping the same materials with different types of carbon NPs.

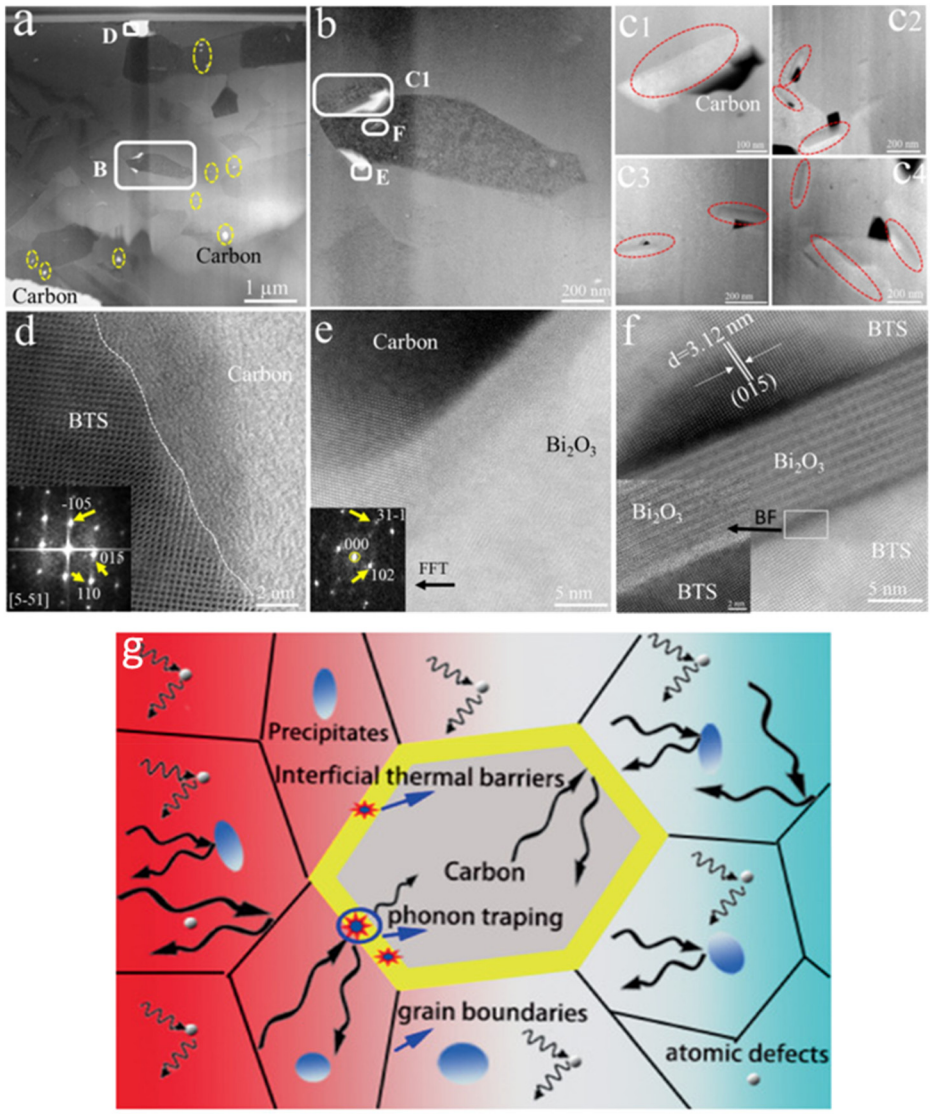

FIG. 29. STEM images of BTS/CF05 specimen. (a) Low magnification bright-field (BF) image showing the BTS matrix (dark) and carbon phase (light, yellow circles). (b) Medium-magnification BF image of the boxed region B in (a) showing the nanoscale carbon located at the grain boundaries. (c) A series of high-angle annular dark-field (HAADF) images showing nanoprecipitates (red ellipses) nucleated at the carbon particles. (d) Atomic-resolution BF image of the boxed region in (a) showing the interface between carbon and BTS. Inset is the diffractogram of the BTS phase showing a [5 – 51] zone axis. (e) HAADF image of the boxed region in (b), showing the interface between carbon (dark, upper left) and Bi_2O_3 (light, lower right), with the inset diffractogram pattern of Bi_2O_3. (f) High-resolution HAADF image showing details of a nanoprecipitate in the boxed region in (b). The inset BF image shows a detail of the interface between the BTS matrix and the Bi_2O_3 precipitate. (g) Schematic of multiple phonon scattering sites induced by compositing with nanocarbon. Reprinted from Yang *et al.*, Chem. Eng. J. **428**, 131–205 (2022). Copyright 2022, with permission from Elsevier,[198] and from Yang *et al.*, Adv. Funct. Mater. **31**, 12 (2021). Copyright 2021, with permission from John Wiley and Sons.[164]

First, we consider the effect of doping with carbon nanotubes (CNTs) that are either single-walled (SW) or multi-walled (MW). SWCNTs and MWCNTs have significantly differing thermal and electrical properties, as well as greatly different production costs—SWCNTs being considerably more expensive.[199] The reported values for the thermal conductivity (tube direction) of individual SWCNTs and MWCNTs are varied across theoretical and experimental estimates, but commonly cited values are $\sim 3500\,W\,m^{-1}\,K^{-1}$ for SWCNTs[200] and $3000\,W\,m^{-1}\,K^{-1}$ for MWCNTs[201] at room temperature.[5] Although individual SWCNTs are generally thought to be more thermally conductive, the difficulty to consistently measure the thermal conductivity of SW and MW CNTs suggests that they are highly dependent on their environment, highly varied in their individual structure across different synthesis routes, or both. Aliev *et al.* suggest that MWCNTs should be a better choice for thermal management (for high thermal conductivity applications) over SWCNTs because they offer higher phonon propagation since more optical phonon modes contribute to heat flow with increasing nanotube diameter and the additional shells can provide additional channels to bypass defect sites.[202] The inverse argument applies for TEC devices. Additional factors are also important in composites, such as how the tubes differ in their dispersion in the matrix and how they differ in interfacial bonding with the matrix. It is known, in general, that SWCNTs are more difficult to disperse homogeneously into a composite matrix, which significantly reduces their potential for enhancing thermal conductivity without precise dispersion techniques.[172] While many separate studies independently investigate the thermal conductivity of SW and MW CNTs, even for the same host material [e.g., in Bi_2Te_3[8,193] and (Bi,Sb)Te[70,203] TECs], the absence of controlled parameters between studies makes deriving meaningful conclusions about the responsible mechanisms for thermal conductivity differences difficult.

The difference in transport properties between SWCNT and MWCNT $Yb_{0.3}Co_4Sb_{12}$ skutterudite composites was included in a study by Zhang *et al.*[196] In their work, different volume percentages, up to 2 vol. % of each type of CNT, were cryogenically ground with $Yb_{0.3}Co_4Sb_{12}$ and consolidated via SPS. Their results show an effective reduction in the composite total thermal conductivity across the entire studied temperature range for both SW and MWCNTs, the latter doing so quite more significantly. When only the lattice thermal conductivity is considered [Fig. 30(a)], however, the differences between the MW and SWCNT composites are small, suggesting that the additional optical phonon modes or additional phonon channels available to avoid defects in MWCNTs do not contribute significantly. A phenomenological model was used to fit the lattice thermal conductivity component that includes resistance terms for phonon–phonon (Umklapp) scattering, a combined term for phonon scattering at grain boundaries and CNT–host interfaces (see Sec. II C 2), and a term for the bipolar thermal conduction [Fig. 30(b), see inset for model).

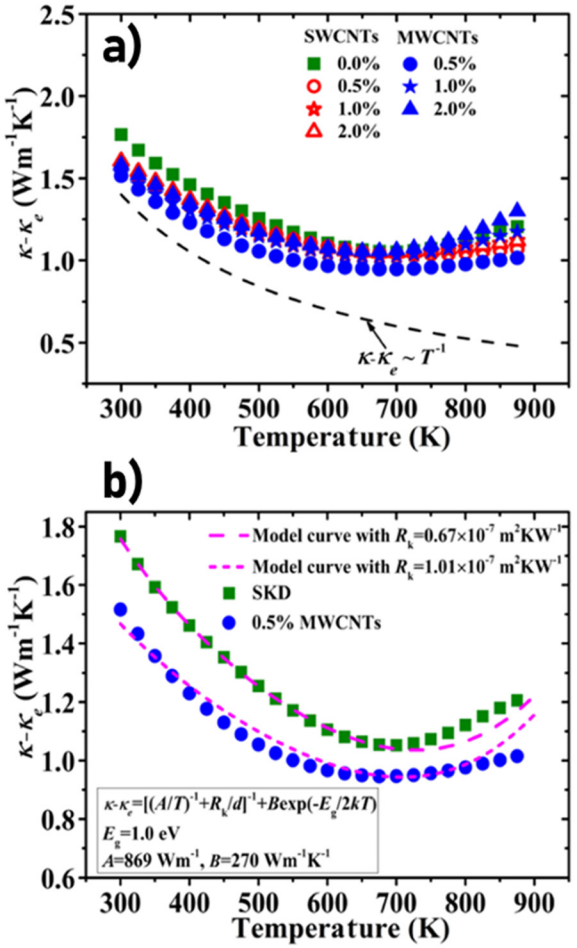

FIG. 30. Thermal transport properties of $Yb_{0.3}Co_4Sb_{12}$-based nanocomposites. Temperature dependence of (a) κ–κ_e, where κ_e is electronic thermal conductivity and (b) a comparison of modeled κ–κ_e for SKD and 0.5 vol. % MWCNTs with experimental values. Reprinted from Zhang *et al.*, Nano Energy **41**, 501–510 (2017). Copyright 2017, with permission from Elsevier.[196]

Modeling using this equation reveals that adding 0.5 vol. % MWCNT to the pure sample effectively increases the interfacial thermal resistance from $R_K = 0.67 \times 10^{-7}$ $m^2\,K\,W^{-1}$ to $R_K = 1.01 \times 10^{-7}$ $m^2\,K\,W^{-1}$. This increase in R_K is assumed to exclusively originate from the CNT–host interfaces since grain sizes are slightly increased in the MWCNT samples. Judging from Fig. 30(a), the phenomenological interfacial resistance of the SWCNT composites should be the same or only slightly smaller than for the MWCNT composites. Without more statistical information about the microstructural differences in the samples, it is difficult to determine the origin of the thermal conductivities of the composites. An extra comparison can be made, however, with work done by Zong *et al.*, who studied $Yb_{0.27}Co_4Sb_{12}$ with rGO doping and calculated R_K (effective grain boundary) values of $3.8 \times 10^{-7}\,m^2\,K\,W^{-1}$ for the pure skutterudite, and $R_K = 17 \times 10^{-7}\,m^2\,K\,W^{-1}$ for the rGO (0.56 vol. %) composite.[75] Unfortunately, the significant difference in the R_K value of the base materials (likely due to the differing synthesis routes) makes pinpointing the origins of the differences in the composites challenging. Nonetheless, we can make a clear comparison between the 1.5× increase in R_K for the $Yb_{0.3}Co_4Sb_{12}$–MWCNT (0.5 vol. %) system, and the 4.5× increase in R_K for the $Yb_{0.27}Co_4Sb_{12}$–rGO (0.56 vol. %) system when the NPs are added. Zhang *et al.* deduce that the difference in R_K for the base materials is due to the order of magnitude difference in the average grain sizes in the materials across the studies. However, the models employed by both studies do include a grain-size term.

Mixed results from studies of polymer matrix composites further highlight the difficulty in determining the physical origins of different thermal properties of MWCNT and SWCNT composites. Moisala *et al.* report reduced thermal conductivity for SWCNT/epoxy composites and increased thermal conductivity for MWCNT/epoxy composites. The authors concluded that phonons at the matrix/SWCNT interface could be damped compared to phonons at the matrix/MWCNT interface where the phonons can be carried in the inner walls,[204] in line with the theory from Ref. 202. Meanwhile, Gulotty *et al.* reported an increased thermal conductivity in SWCNT and MWCNT epoxy composites, with minimal differences between the two types,[205] and Hong and Tai demonstrated that SWCNTs can outperform MWCNTs in a polymer CNT matrix, with their SWCNT/PMMA matrix samples.[206]

One of the few systematic studies on the effects of compositing with different types of carbon NPs on the thermoelectric properties of a given host material was conducted by Zhao *et al.* in their work on Cu_2Se composites.[54] Carbon-reinforced Cu_2Se composites were fabricated by a melt solidification route through incorporating a small weight fraction of carbon nanotubes, graphite, hard carbon, and carbon black (Super P) (Fig. 31). Across most thermoelectric properties, very similar effects from compositing are reported, regardless of the carbon additive used. With regard to thermal conductivity, this is also true. Figure 31(d) shows the total thermal conductivity values of each composite with optimal doping concentrations. A similar analysis to Zhang *et al.* and Zong *et al.* (above) is provided, using Eq. (19) to calculate the effective carbon-coated grain boundary Kapitza resistance. The analysis is kept general to all of the carbon composites, with graphite used as a case study. For the pure sample, R_K has a very low value, $<1 \times 10^{-9}\,m^2\,K\,W^{-1}$, while the carbon-doped Cu_2Se samples significantly increase R_K to $0.45 \times 10^{-7}\,m^2\,K\,W^{-1}$ (approximating all of the samples' thermal conductivity to be $\sim 0.5\,W\,m^{-2}\,K^{-1}$).

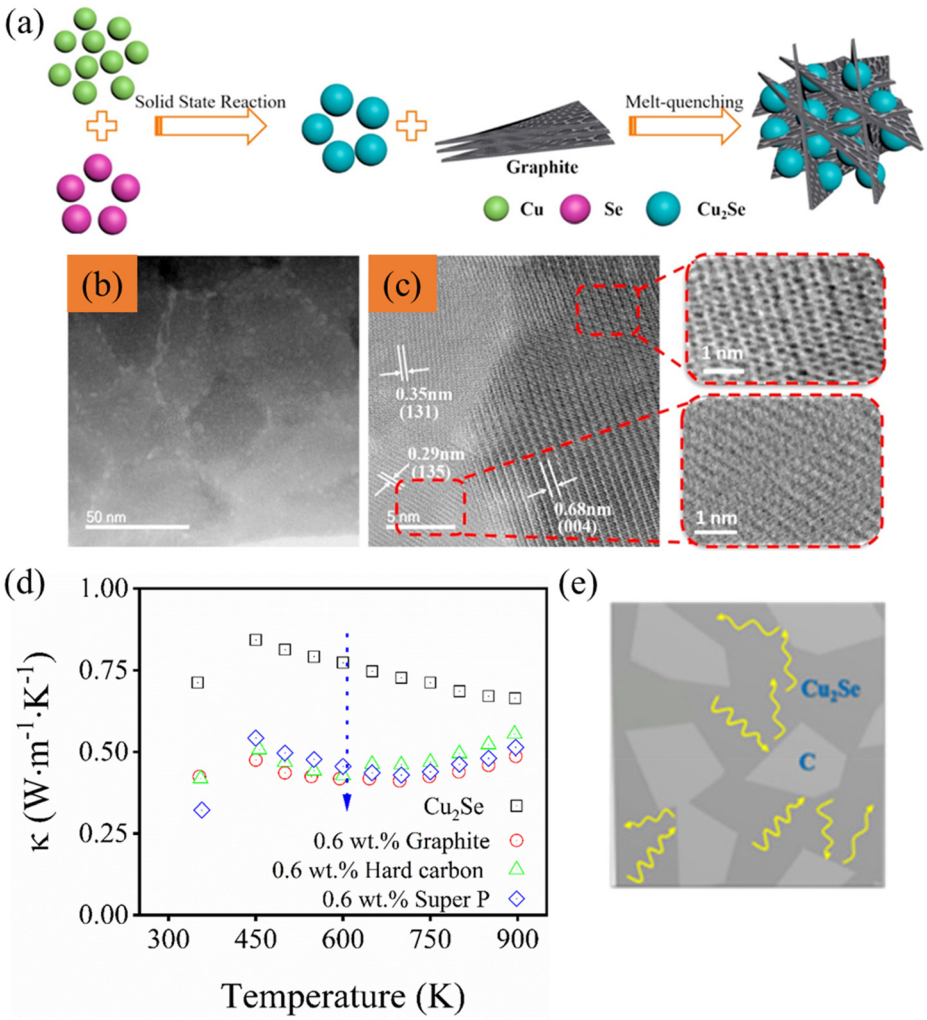

FIG. 31. (a) Schematic illustration of the fabrication process of the graphite incorporated Cu_2Se. (b) Low- (c) and high-resolution TEM images showing the lattice and interface between graphite nanoclusters and Cu_2Se. (d) Temperature-dependent thermal conductivity with the different types of carbon in Cu_2Se. (e) Phonon scattering representation in carbon incorporated Cu_2Se sample. Reprinted from Zhao *et al.*, Nano Energy **41**, 164–171 (2017). Copyright 2017, with permission from Elsevier.[54]

The increase in R_K is put into context by applying the density values and the transverse and longitudinal speeds of sound for graphite and Cu_2Se to the acoustic mismatch model to obtain a Cu_2Se:graphite acoustic impedance scaling factor of $R_K T^3 = 126\,K^4\,cm^2\,W^{-1}$, compared to other systems such as aluminum:sapphire ($21\,K^4\,cm^2\,W^{-1}$) and indium:diamond ($88\,K^4\,cm^2\,W^{-1}$). While this is a helpful comparison, a more detailed analysis of the thermal conductivity of each composite, which considers the difference in thermal properties of each of the carbon NPs and the resulting microstructure of the composite, is necessary to unveil the underlying physics governing the composite thermal conductivity.

E. Concluding Remarks and Outlook

Evidently, carbon nanoparticles (NPs) can strongly influence the thermal properties of solid-state composite materials. In thermoelectric (TE) materials, thermal conductivity can be more than halved when composited with just a small fraction of carbon NPs. It is clear from this review that this central observation has been observed and reproduced in many separate studies. This indicates great prospects for producing a new generation of TE materials with enhanced performance utilizing nanocarbon dopants. However, for optimum performance, it will be first necessary to fully identify the underlying physical transport mechanisms. This will allow for the synergistic reduction of thermal conductivity by precisely controlling the many factors outlined in this work including porosity, particle dispersion, and thermal interfaces, as well as maintaining synergy with other TE engineering strategies. Additionally, many of these considerations could be universally applicable to other types of NPs. At present, several areas require additional investigation to identify the ideal carbon and TE matrix combinations. For example, when surveying the thermal conductivity values reported in the literature for TE materials doped with different carbon NPs, the reduction in values seems to have some universal quality—not having any obvious dependence on the allotrope of carbon NP used. From the few studies that have taken a more systematic approach to measuring the effects of compositing with different types of carbon NPs in TE materials, there is little experimental evidence to support that, for a given host material and synthesis method, there is a

significant difference in the resulting thermal conductivity of composites for different carbon forms. However, the number of experimental works that investigate this hypothesis is extremely limited, and the number of parameters to control is very large.

A self-consistent, complete theory for the reduction in thermal conductivity has also proven to be elusive. So far, the thermal conductivity of carbon nanocomposites has been primarily understood in the frameworks of the effective medium approach (EMA) or the transport of a phonon-gas (Boltzmann transport). Both frameworks include the existence of a thermal boundary between the host and carbon additive, which hinders thermal transport by adding thermal resistance (R_K, in the EMA framework) or by increasing phonon scattering ($1/\tau$, in the phonon-gas framework). In TE materials, generally, however, the significant reduction in thermal conductivity achieved with the addition of carbon NPs is unable to be solely explained by thermal boundary resistance. Rather, the literature demonstrates that a combination of thermal interfaces and changes to the intrinsic host material, such as pores/voids, localized stresses and strains, and altered grain boundaries, which are induced by the presence of carbon NPs, all contribute to the drastic change in thermal conductivity. Accurately characterizing these mechanisms, however, has proven challenging. The primary challenge seems to be the deconvolution of the many contributions to the thermal conductivity with the addition of carbon NPs. From an EMA perspective, there is a lack of consideration of how the carbon NPs will alter the properties of the matrix material, with all the altered material properties and resulting physics being bundled into R_K. Convincing evidence of how the particles are included or dispersed in the matrix is also often missing in many studies. While techniques such as electron microscopy can provide imaging on the length scale that is necessary to observe important structural motifs, these techniques do not provide large statistics (without the need for a considerable investment of time). From a phonon-gas perspective, separating out all scattering contributions (Umklapp scattering, grain-boundary scattering, NP scattering, etc.) requires accurate models for the scattering processes, which often (each) rely on a highly detailed and statistically accurate description of the material on the atomic- or nano-scale. This can arguably only lead to a semi-quantitative analysis of thermal transport due to overparameterizing. Additionally, the significance of diffuson-mediated thermal transport in carbon nanocomposites is thus far unexplored, despite having been demonstrated to have a significant role in other disordered materials.

On top of the challenges presented for utilizing EMA and Boltzmann-transport frameworks, the possibility of phonons interacting coherently with the microstructure of nanocomposites, which are on the same size scale as the wavelengths of heat-carrying phonons, has largely been ignored. It is likely that analyzing phonon propagation from a meta-structure-based framework is necessary in addition to, or instead of, simply treating the phonon/heat propagation in the host and additive separately. Currently, there is a limited number of works exploring the precise lattice dynamics of nanoparticles and nanocomposite systems, which are responsible for transporting heat. A fully quantitative, self-consistent model for the thermal conductivity of carbon nanocomposites is lacking, and without this, it is not yet possible for experimentalists to fully optimize material-design procedures. As such, there is tremendous scope to improve the thermal properties of such composites beyond what is currently possible. Considering the current theoretical and other practical limitations presented, we suggest a few approaches to developing a deeper understanding of thermal transport in carbon nanocomposite materials, and nanocomposite materials in general, which will guide researchers to higher-performing thermoelectric devices, heat sinks, thermal interface materials, and more.

First, we suggest spectroscopic studies, which probe the lattice dynamics of the host, dopant (nanoparticle), and nanocomposite systems, which carefully track changes in vibrational modes in the nanoparticles and host materials upon compositing. Inelastic neutron/x-ray scattering, Raman, and infrared/THz spectroscopy have already proven highly effective lattice dynamics probes for bulk and nanoparticle materials and can be further utilized to this effect.

Second, high-performance computing is driving advances in large-scale molecular dynamics (MD), enabling simulations up to millions of atoms. In tandem, density functional theory (DFT) calculations in combination with *ab initio* MD now offer first-principles (parameter-free) descriptions of systems of several hundred atoms. Combining these two different approaches, the prospect of advanced simulation ensembles of carbon NPs in TE matrices is close at hand. The advantage of these MD theoretical methods is that they can potentially predict the thermal conductivity based on an atomic-scale structure and realistic microstructures, without resorting to simplifications or approximations inherent in, for example, the EMA or phonon gas models. Indeed, careful comparison between MD simulations and the latter models will also help refine some of the approximations inherent in the EMA and phonon gas pictures. So far, such methods have been introduced to distinguish between propagons, diffusons, and locons using the Green–Kubo framework (Green–Kubo Modal Analysis, GKMA).[148] Related calculations can also potentially be used to directly test the predictions of the underlying principles of thermal boundary resistance such as the diffuse mismatch model, and the role of elastic and inelastic processes at interfaces (Interfacial Modal Analysis, ICMA).[207,208] One challenge in past classical MD work has been the lack of suitable forcefields to rigorously describe the bonding between carbon nanoparticles and TE host matrices. For this reason, past classical MD simulations often used simplified descriptions based on force fields such as Lenard Jones interactions, which, while providing a qualitative insight into the mechanisms, can never describe the full quantum chemical details. With the arrival of machine-learning forcefields, which can be "trained" using *ab initio* methods such as DFT and then translated into classical MD simulations,[209] it is now increasingly possible to envision more accurate descriptions of carbon:TE composites for the first time.

Third, high temporal and spatial resolution thermal conductivity techniques such as (picosecond) time-domain and frequency domain thermoreflectance provide opportunities to measure thermal conductivity and resistance at nanoscale interfaces. These data can then be used to validate models for thermal conductivity, which include the interfacial terms, or to create entirely new models.

Finally, we suggest that detailed structural and compositional material characterization will greatly aid the development of models for the thermal conductivity of nanocomposite materials. Such models inevitably rely on a description of the microstructure of a given system. Hence, more accurate descriptions of the microstructure of materials will result in more accurate models. Electron microscopy (scanning and transmission electron microscopy, and their commonly combined techniques such as energy-dispersive x-ray spectroscopy and electron energy loss spectroscopy) remains a fundamental probe in this regard.

However, owing to the small probe region and time-intensive nature of such measurements, they unavoidably lack sufficient statistical information and are prone to operator and/or sample biasing. Additional techniques can be utilized to probe such structures such as x-ray diffraction combined with refinement procedures to extract changes in grain sizes, microstrain, and shifting lattice parameters. A more optimal approach is to utilize synchrotron x-ray sources and/or neutron sources to obtain diffraction and small-angle scattering patterns for higher resolution (x-ray), different atomic contrast (neutron), and measurement of solid bulk (millimeter-scale) samples for better statistical information (neutron). Given that many TE materials are comprised of heavy elements, and therefore are relatively opaque to x-rays, the penetration power of neutron techniques potentially offers an attractive way to gain high statistical information about the microstructure.

The impressive set of thermal conductivity results already available in the literature suggests that carbon compositing holds tremendous promise for the next generation of thermoelectric and heat-management materials. With increasingly developed theory and characterization, record-breaking improvements in these composite materials are inevitable.

ACKNOWLEDGMENTS

The authors would like to acknowledge the insight kindly provided by Professor Chao Zhang through helpful discussions with the authors and the revision of this work. CS acknowledges support from the Australian Government Research Training Program (RTP) through the University of Wollongong, and the Postgraduate Research Award (PGRA) provided by the Australian Institute of Nuclear Science and Engineering. The work was also supported by the Australian Research Council (No. DP210101436).

AUTHOR DECLARATIONS

Conflict of Interest

The authors have no conflicts to disclose.

Author Contributions

Caleb Stamper: Conceptualization (equal); Data curation (lead); Formal analysis (lead); Project administration (lead); Visualization (lead); Writing – original draft (lead); Writing – review & editing (equal). **David Cortie:** Conceptualization (equal); Formal analysis (supporting); Supervision (equal); Visualization (supporting); Writing – original draft (supporting); Writing – review & editing (equal). **Sheik Md Kazi Nazrul Islam:** Visualization (supporting); Writing – original draft (supporting). **Md Rezoanur Rahman:** Project administration (equal); Writing – original draft (supporting). **Dehong Yu:** Writing – original draft (supporting); Writing – review & editing (equal). **Guangsai Yang:** Writing – original draft (supporting). **Abdullah Al-Mamun:** Visualization (supporting). **Xiaolin Wang:** Writing – review & editing (equal). **Zengji Yue:** Conceptualization (equal); Supervision (equal); Writing – original draft (supporting); Writing – review & editing (equal).

DATA AVAILABILITY

The data that support the findings of this study are available from the corresponding authors upon reasonable request.

REFERENCES

[1]The Future of Cooling (International Energy Agency, Paris, 2018). https://www.iea.org/reports/the-future-of-cooling.
[2]C. Forman, I. K. Muritala, R. Pardemann, and B. Meyer, "Estimating the global waste heat potential," Renewable Sustain. Energy Rev. **57**, 1568–1579 (2016).
[3]Z. Han and A. Fina, "Thermal conductivity of carbon nanotubes and their polymer nanocomposites: A review," Prog. Polym. Sci. **36**(7), 914–944 (2011).
[4]W.-D. Liu, Y. Yu, M. Dargusch, Q. Liu, and Z.-G. Chen, "Carbon allotrope hybrids advance thermoelectric development and applications," Renewable Sustain. Energy Rev. **141**, 110800 (2021).
[5]A. A. Balandin, "Thermal properties of graphene and nanostructured carbon materials," Nat. Mater. **10**(8), 569–581 (2011).
[6]B. Kumanek and D. Janas, "Thermal conductivity of carbon nanotube networks: A review," J. Mater. Sci. **54**(10), 7397–7427 (2019).
[7]I. A. Kinloch, J. Suhr, J. Lou, R. J. Young, and P. M. Ajayan, "Composites with carbon nanotubes and graphene: An outlook," Science **362**(6414), 547–553 (2018).
[8]Y. Zhang, X. L. Wang, W. K. Yeoh, R. K. Zheng, and C. Zhang, "Electrical and thermoelectric properties of single-wall carbon nanotube doped Bi_2Te_3," Appl. Phys. Lett. **101**(3), 031909 (2012).
[9]P. Chakraborty, T. Ma, A. H. Zahiri, L. Cao, and Y. Wang, "Carbon-based materials for thermoelectrics," Adv. Condens. Matter Phys. **2018**, 3898479.
[10]X.-H. Qu, L. Zhang, M. Wu, and S.-B. Ren, "Review of metal matrix composites with high thermal conductivity for thermal management applications," Prog. Nat. Sci.: Mater. Int. **21**(3), 189–197 (2011).
[11]S. S. Sidhu, S. Kumar, and A. Batish, "Metal matrix composites for thermal management: A review," Crit. Rev. Solid State Mater. Sci. **41**(2), 132–157 (2016).
[12]J. Hong, D. W. Park, and S. E. A. Shim, "Review on thermal conductivity of polymer composites using carbon-based fillers: Carbon nanotubes and carbon fibers," Carbon Lett. **11**(4), 347–356 (2010).
[13]Y. Yin, K. Baskaran, and A. Tiwari, "A review of strategies for developing promising thermoelectric materials by controlling thermal conduction," Phys. Status Solidi A **216**(14), 1800904 (2019).
[14]B. Qin, D. Wang, and L.-D. Zhao, "Slowing down the heat in thermoelectrics," InfoMat **3**(7), 755–789 (2021).
[15]Z. Chen, X. Zhang, and Y. Pei, "Manipulation of phonon transport in thermoelectrics," Adv. Mater. **30**(17), 1705617 (2018).
[16]H. Chen, V. V. Ginzburg, J. Yang, Y. Yang, W. Liu, Y. Huang, L. Du, and B. Chen, "Thermal conductivity of polymer-based composites: Fundamentals and applications," Prog. Polym. Sci. **59**, 41–85 (2016).
[17]M. Hamid Elsheikh, D. A. Shnawah, M. F. M. Sabri, S. B. M. Said, M. Haji Hassan, M. B. Ali Bashir, and M. Mohamad, "A review on thermoelectric renewable energy: Principle parameters that affect their performance," Renewable Sustain. Energy Rev. **30**, 337–355 (2014).
[18]S. Twaha, J. Zhu, Y. Yan, and B. Li, "A comprehensive review of thermoelectric technology: Materials, applications, modelling and performance improvement," Renewable Sustain. Energy Rev. **65**, 698–726 (2016).
[19]D. Champier, "Thermoelectric generators: A review of applications," Energy Convers. Manage. **140**, 167–181 (2017).
[20]R. He, G. Schierning, and K. Nielsch, "Thermoelectric devices: A review of devices, architectures, and contact optimization," Adv. Mater. Technol. **3**(4), 1700256 (2018).
[21]S. M. Pourkiaei, M. H. Ahmadi, M. Sadeghzadeh, S. Moosavi, F. Pourfayaz, L. Chen, M. A. Pour Yazdi, and R. Kumar, "Thermoelectric cooler and thermoelectric generator devices: A review of present and potential applications, modeling and materials," Energy **186**, 115849 (2019).
[22]D. M. Rowe, *CRC Handbook of Thermoelectrics* (CRC Press, 2017).
[23]F. Ritz and C. E. Peterson, "Multi-mission radioisotope thermoelectric generator (MMRTG) program overview," In *2004 IEEE Aerospace Conference Proceedings* (IEEE, 2004), Vol. 5, pp. 2950–2957.
[24]R. G. Lange and W. P. Carroll, "Review of recent advances of radioisotope power systems," Energy Convers. Manage. **49**(3), 393–401 (2008).
[25]W. Shin, K. Imai, N. Izu, and N. Murayama, "Thermoelectric thick-film hydrogen gas sensor operating at room temperature," Jpn. J. Appl. Phys. **40**(11B), L1232 (2001).

[26]L. Rebenklau, P. Gierth, A. Paproth, K. Irrgang, L. Lippmann, A. Wodtke, L. Niedermeyer, K. Augsburg, and F. Bechtold, "Temperature sensors based on thermoelectric effect," In *2015 European Microelectronics Packaging Conference (EMPC)* (IEEE, 2015), pp. 1–5.
[27]M. D. Thakor, S. Hadia, and A. Kumar, "Precise temperature control through thermoelectric cooler with PID controller," *2015 International Conference on Communications and Signal Processing (ICCSP)* (IEEE, 2015).
[28]U. Sanver, E. Yavuz, and C. Eyupoglu, "An electronic control unit for thermoelectric cooling," In *2019 IEEE Conference of Russian Young Researchers in Electrical and Electronic Engineering (EIConRus)* (IEEE, 2019), pp. 141–145.
[29]Y. Yang, X.-J. Wei, and J. Liu, "Suitability of a thermoelectric power generator for implantable medical electronic devices," J. Phys. D: Appl. Phys. **40**(18), 5790–5800 (2007).
[30]V. Leonov and R. J. M. Vullers, "Wearable electronics self-powered by using human body heat: The state of the art and the perspective," J. Renewable Sustain. Energy **1**(6), 062701 (2009).
[31]E. Romero, R. O. Warrington, and M. R. Neuman, "Energy scavenging sources for biomedical sensors," Physiol. Meas. **30**(9), R35–R62 (2009).
[32]M. Rasouli and L. S. J. Phee, "Energy sources and their development for application in medical devices," Expert Rev. Med. Devices **7**(5), 693–709 (2010).
[33]V. Leonov, "Thermoelectric energy harvester on the heated human machine," J. Micromech. Microeng. **21**(12), 125013 (2011).
[34]A. R. M. Siddique, S. Mahmud, and B. V. Heyst, "A review of the state of the science on wearable thermoelectric power generators (TEGs) and their existing challenges," Renewable Sustain. Energy Rev. **73**, 730–744 (2017).
[35]J. Yang and F. R. Stabler, "Automotive applications of thermoelectric materials," J. Electron. Mater. **38**(7), 1245–1251 (2009).
[36]R. P. Chasmar and R. Stratton, "The thermoelectric figure of merit and its relation to thermoelectric generators," J. Electron. Control **7**(1), 52–72 (1959).
[37]W. R. Fahrner and S. Schwertheim, *Semiconductor Thermoelectric Generators* (Trans Tech Publications, Limited, 2009).
[38]R. Franz and G. Wiedemann, "Ueber die Wärme-Leitungsfähigkeit der Metalle," Ann. Phys. **165**(8), 497–531 (1853).
[39]G. A. Slack, "New materials and performance limits for thermoelectric cooling," In *CRC Handbook of Thermoelectrics*, edited by D. M. Rowe, 1st ed. (CRC Press, 1995), pp. 407–440.
[40]W. Kim, "Strategies for engineering phonon transport in thermoelectrics," J. Mater. Chem. C **3**(40), 10336–10348 (2015).
[41]C. Chang, G. Tan, J. He, M. G. Kanatzidis, and L.-D. Zhao, "The thermoelectric properties of SnSe continue to surprise: Extraordinary electron and phonon transport," Chem. Mater. **30**(21), 7355–7367 (2018).
[42]Y. Xiao and L.-D. Zhao, "Charge and phonon transport in PbTe-based thermoelectric materials," NPJ Quant. Mater. **3**(1), 1–12 (2018).
[43]T. Hori and J. Shiomi, "Tuning phonon transport spectrum for better thermoelectric materials," Sci. Technol. Adv. Mater. **19**(NRG3), 10–25 (2018).
[44]S. Hooshmand Zaferani, R. Ghomashchi, and D. Vashaee, "Strategies for engineering phonon transport in Heusler thermoelectric compounds," Renewable Sustain. Energy Rev. **112**, 158–169 (2019).
[45]M. S. Dresselhaus, G. Chen, M. Y. Tang, R. G. Yang, H. Lee, D. Z. Wang, Z. F. Ren, J.-P. Fleurial, and P. Gogna, "New directions for low-dimensional thermoelectric materials," Adv. Mater. **19**(8), 1043–1053 (2007).
[46]W. Liu, X. Yan, G. Chen, and Z. Ren, "Recent advances in thermoelectric nanocomposites," Nano Energy **1**(1), 42–56 (2012).
[47]K. Ahmad and C. Wan, "Enhanced thermoelectric performance of Bi_2Te_3 through uniform dispersion of single wall carbon nanotubes," Nanotechnology **28**(41), 415402 (2017).
[48]M. Li, D. L. Cortie, J. Liu, D. Yu, S. M. K. N. Islam, L. Zhao, D. R. G. Mitchell, R. A. Mole, M. B. Cortie, S. Dou *et al.*, "Ultra-high thermoelectric performance in graphene incorporated Cu_2Se: Role of mismatching phonon modes," Nano Energy **53**, 993–1002 (2018).
[49]L. Chen, W. Zhao, M. Li, G. Yang, S. M. K. Nazrul Islam, D. R. G. Mitchell, Z. Cheng, and X. Wang, "Graphene inclusion induced ultralow thermal conductivity and improved figure of merit in p-type SnSe," Nanoscale **12**(24), 12760–12766 (2020).
[50]W. H. Nam, Y. S. Lim, W. Kim, H. K. Seo, K. S. Dae, S. Lee, W. S. Seo, and J. Y. Lee, "A gigantically increased ratio of electrical to thermal conductivity and synergistically enhanced thermoelectric properties in interface-controlled TiO_2-RGO nanocomposites," Nanoscale **9**(23), 7830–7838 (2017).
[51]X. Shi, L. Chen, J. Yang, and G. P. Meisner, "Enhanced thermoelectric figure of merit of $CoSb_3$ via large-defect scattering," Appl. Phys. Lett. **84**(13), 2301–2303 (2004).
[52]S. M. K. N. Islam, M. B. Cortie, and X. Wang, "Grape juice: An effective liquid additive for significant enhancement of thermoelectric performance of Cu_2Se," J. Mater. Chem. A **8**(33), 16913–16919 (2020).
[53]Q. Hu, Y. Zhang, Y. Zhang, X.-J. Li, and H. Song, "High thermoelectric performance in Cu_2Se/CDs hybrid materials," J. Alloys Compd. **813**, 152204 (2020).
[54]L. Zhao, S. M. K. N. Islam, J. Wang, D. L. Cortie, X. Wang, Z. Cheng, J. Wang, N. Ye, S. Dou, and X. Shi, "Significant enhancement of figure-of-merit in carbon-reinforced Cu_2Se nanocrystalline solids," Nano Energy **41**, 164–171 (2017).
[55]M. Li, S. M. K. N. Islam, S. X. Dou, and X. L. Wang, "Significantly enhanced figure-of-merit in graphene nanoplate incorporated Cu_2Se fabricated by spark plasma sintering," J. Alloys Compd. **769**, 59–64 (2018).
[56]R. Nunna, P. F. Qiu, M. J. Yin, H. Y. Chen, R. Hanus, Q. F. Song, T. S. Zhang, M. Y. Chou, M. T. Agne, J. Q. He *et al.*, "Ultrahigh thermoelectric performance in Cu_2Se-based hybrid materials with highly dispersed molecular CNTs," Energy Environ. Sci. **10**(9), 1928–1935 (2017).
[57]S. T. Lee and Y. S. Lim, "Effects of interface control using reduced graphene oxide (RGO) on the thermoelectric transport properties of polycrystalline SnSe compounds," Korean J. Met. Mater. **56**(2), 163–169 (2018).
[58]F. Chu, Q. Zhang, Z. Zhou, D. Hou, L. Wang, and W. Jiang, "Enhanced thermoelectric and mechanical properties of Na-doped polycrystalline SnSe thermoelectric materials via CNTs dispersion," J. Alloys Compd. **741**, 756–764 (2018).
[59]J. C. Li, D. Li, W. Xu, X. Y. Qin, Y. Y. Li, and J. Zhang, "Enhanced thermoelectric performance of SnSe based composites with carbon black nanoinclusions," Appl. Phys. Lett. **109**(17), 173902 (2016).
[60]G. S. Yang, L. N. Sang, M. Li, S. M. K. N. Islam, Z. J. Yue, L. Q. Liu, J. N. Li, D. R. G. Mitchell, N. Ye, and X. L. Wang, "Enhancing the thermoelectric performance of polycrystalline SnSe by decoupling electrical and thermal transport through carbon fiber incorporation," ACS Appl. Mater. Interfaces **12**(11), 12910–12918 (2020).
[61]L. S. Huang, J. Z. Lu, D. W. Ma, C. M. Ma, B. Zhang, H. Y. Wang, G. Y. Wang, D. H. Gregory, X. Y. Zhou, and G. Han, "Facile in situ solution synthesis of SnSe/rGO nanocomposites with enhanced thermoelectric performance," J. Mater. Chem. A **8**(3), 1394–1402 (2020).
[62]K. Ahmad, C. Wan, M. A. Al-Eshaikh, and A. N. Kadachi, "Enhanced thermoelectric performance of Bi_2Te_3 based graphene nanocomposites," Appl. Surf. Sci. **474**, 2–8 (2019).
[63]B. Liang, Z. Song, M. Wang, L. Wang, and W. Jiang, "Fabrication and thermoelectric properties of graphene/Bi_2Te_3 composite materials," J. Nanomater. **2013**, 210767.
[64]K. T. Kim, S. Y. Choi, E. H. Shin, K. S. Moon, H. Y. Koo, G. G. Lee, and G. H. Ha, "The influence of CNTs on the thermoelectric properties of a CNT/Bi_2Te_3 composite," Carbon **52**, 541–549 (2013).
[65]K. Agarwal, V. Kaushik, D. Varandani, A. Dhar, and B. R. Mehta, "Nanoscale thermoelectric properties of Bi_2Te_3–graphene nanocomposites: Conducting atomic force, scanning thermal and kelvin probe microscopy studies," J. Alloys Compd. **681**, 394–401 (2016).
[66]D. Suh, S. Lee, H. Mun, S. H. Park, K. H. Lee, S. W. Kim, J. Y. Choi, and S. Baik, "Enhanced thermoelectric performance of $Bi_{0.5}Sb_{1.5}Te_3$-expanded graphene composites by simultaneous modulation of electronic and thermal carrier transport," Nano Energy **13**, 67–76 (2015).
[67]W. H. Shin, K. Ahn, M. Jeong, J. S. Yoon, J. M. Song, S. Lee, W. S. Seo, and Y. S. Lim, "Enhanced thermoelectric performance of reduced graphene oxide incorporated bismuth-antimony-telluride by lattice thermal conductivity reduction," J. Alloys Compd. **718**, 342–348 (2017).
[68]K. T. Kim, T. S. Min, S.-D. Kim, E.-A. Choi, D. W. Kim, and S.-Y. Choi, "Strain-mediated point defects in thermoelectric p-type bismuth telluride polycrystalline," Nano Energy **55**, 486–493 (2019).
[69]D. W. Xie, J. T. Xu, G. Q. Liu, Z. Liu, H. Z. Shao, X. J. Tan, J. Jiang, and H. C. Jiang, "Synergistic optimization of thermoelectric performance in p-type $Bi_{0.48}Sb_{1.52}Te_3$/graphene composite," Energies **9**(4), 236 (2016).

[70]Y. H. Yeo and T. S. Oh, "Thermoelectric properties of p-type $(Bi,Sb)_2Te_3$ nanocomposites dispersed with multiwall carbon nanotubes," Mater. Res. Bull. **58**, 54–58 (2014).

[71]U. G. Hwang, K. Kim, W. Kim, W. H. Shin, W. S. Seo, and Y. S. Lim, "Thermoelectric transport properties of interface-controlled p-type bismuth antimony telluride composites by reduced graphene oxide," Electron Mater. Lett. **15**(5), 605–612 (2019).

[72]P. A. Zong, X. H. Chen, Y. W. Zhu, Z. W. Liu, Y. Zeng, and L. D. Chen, "Construction of a 3D-rGO network-wrapping architecture in a $Yb_yCo_4Sb_{12}$/rGO composite for enhancing the thermoelectric performance," J. Mater. Chem. A **3**(16), 8643–8649 (2015).

[73]B. Feng, J. Xie, G. Cao, T. Zhu, and X. Zhao, "Enhanced thermoelectric properties of p-type $CoSb_3$/graphene nanocomposite," J. Mater. Chem. A **1**(42), 13111–13119 (2013).

[74]X. Shi, L. D. Chen, S. Q. Bai, X. Y. Huang, X. Y. Zhao, Q. Yao, and C. Uher, "Influence of fullerene dispersion on high temperature thermoelectric properties of $Ba_yCo_4Sb_{12}$-based composites," J. Appl. Phys. **102**(10), 103709 (2007).

[75]P-a Zong, R. Hanus, M. Dylla, Y. Tang, J. Liao, Q. Zhang, G. J. Snyder, and L. Chen, "Skutterudite with graphene-modified grain-boundary complexion enhances zT enabling high-efficiency thermoelectric device," Energy Environ. Sci. **10**(1), 183–191 (2017).

[76]D. S. Chen, Y. Zhao, Y. N. Chen, B. A. Wang, H. Y. Chen, J. Zhou, and Z. Q. Liang, "One-step chemical synthesis of ZnO/graphene oxide molecular hybrids for high-temperature thermoelectric applications," ACS Appl. Mater. Interfaces **7**(5), 3224–3230 (2015).

[77]G. Tang, W. Yang, J. Wen, Z. Wu, C. Fan, and Z. Wang, "Ultralow thermal conductivity and thermoelectric properties of carbon nanotubes doped $Ca_3Co_4O_{9+\delta}$," Ceram. Int. **41**(1, Part B), 961–965 (2015).

[78]M. T. Agne, R. Hanus, and G. J. Snyder, "Minimum thermal conductivity in the context of diffuson-mediated thermal transport," Energy Environ. Sci. **11**(3), 609–616 (2018).

[79]P. Strongman, V. Askarpour, and J. Maassen, "Impact of dimensional crossover on phonon transport in van der Waals materials: A case study of graphite and graphene," Phys. Rev. B **104**(3), 035428 (2021).

[80]E. N. Koukaras, G. Kalosakas, C. Galiotis, and K. Papagelis, "Phonon properties of graphene derived from molecular dynamics simulations," Sci. Rep. **5**(1), 12923 (2015).

[81]Y. Kuang, L. Lindsay, S. Shi, X. Wang, and B. Huang, "Thermal conductivity of graphene mediated by strain and size," Int. J. Heat Mass Transfer **101**, 772–778 (2016).

[82]S. Ghosh, I. Calizo, D. Teweldebrhan, E. P. Pokatilov, D. L. Nika, A. A. Balandin, W. Bao, F. Miao, and C. N. Lau, "Extremely high thermal conductivity of graphene: Prospects for thermal management applications in nanoelectronic circuits," Appl. Phys. Lett. **92**(15), 151911 (2008).

[83]A. A. Balandin, S. Ghosh, W. Bao, I. Calizo, D. Teweldebrhan, F. Miao, and C. N. Lau, "Superior thermal conductivity of single-layer graphene," Nano Lett. **8**(3), 902–907 (2008).

[84]S. Ghosh, W. Bao, D. L. Nika, S. Subrina, E. P. Pokatilov, C. N. Lau, and A. A. Balandin, "Dimensional crossover of thermal transport in few-layer graphene," Nat. Mater. **9**(7), 555–558 (2010).

[85]J. H. Seol, I. Jo, A. L. Moore, L. Lindsay, Z. H. Aitken, M. T. Pettes, X. Li, Z. Yao, R. Huang, D. Broido *et al.*, "Two-dimensional phonon transport in supported graphene," Science **328**(5975), 213–216 (2010).

[86]X.-K. Chen and K.-Q. Chen, "Thermal transport of carbon nanomaterials," J. Phys.: Condens. Matter **32**(15), 153002 (2020).

[87]N. Wei, L. Xu, H.-Q. Wang, and J.-C. Zheng, "Strain engineering of thermal conductivity in graphene sheets and nanoribbons: A demonstration of magic flexibility," Nanotechnology **22**(10), 105705 (2011).

[88]X. Mu, X. Wu, T. Zhang, D. B. Go, and T. Luo, "Thermal transport in graphene oxide—From ballistic extreme to amorphous limit," Sci. Rep. **4**(1), 3909 (2014).

[89]H. Lamb, "On the vibrations of an elastic sphere," Proc. London Math. Soc. **1–13**(1), 189–212 (1881).

[90]S. Stehlik, M. Mermoux, B. Schummer, O. Vanek, K. Kolarova, P. Stenclova, A. Vlk, M. Ledinsky, R. Pfeifer, O. Romanyuk *et al.*, "Size effects on surface chemistry and Raman spectra of sub-5 nm oxidized high-pressure high-temperature and detonation nanodiamonds," J. Phys. Chem. C **125**(10), 5647–5669 (2021).

[91]M. H. Kuok, H. S. Lim, S. C. Ng, N. N. Liu, and Z. K. Wang, "Brillouin study of the quantization of acoustic modes in nanospheres," Phys. Rev. Lett. **90**(25), 255502 (2003).

[92]M. Bayle, N. Combe, N. M. Sangeetha, G. Viau, and R. Carles, "Vibrational and electronic excitations in gold nanocrystals," Nanoscale **6**(15), 9157–9165 (2014).

[93]A. Vlk, M. Ledinsky, A. Shiryaev, E. Ekimov, and S. Stehlik, "Nanodiamond size from low-frequency acoustic Raman modes," J. Phys. Chem. C **126**(14), 6318–6324 (2022).

[94]A. Kara and T. S. Rahman, "Vibrational properties of metallic nanocrystals," Phys. Rev. Lett. **81**(7), 1453–1456 (1998).

[95]M. Bayle, P. Benzo, N. Combe, C. Gatel, C. Bonafos, G. Benassayag, and R. Carles, "Experimental investigation of the vibrational density of states and electronic excitations in metallic nanocrystals," Phys. Rev. B **89**(19), 195402 (2014).

[96]D. Şopu, J. Kotakoski, and K. Albe, "Finite-size effects in the phonon density of states of nanostructured germanium: A comparative study of nanoparticles, nanocrystals, nanoglasses, and bulk phases," Phys. Rev. B **83**(24), 245416 (2011).

[97]P. C. H. Mitchell, A. J. Ramirez-Cuesta, S. F. Parker, J. Tomkinson, and D. Thompsett, "Hydrogen spillover on carbon-supported metal catalysts studied by inelastic neutron scattering. Surface vibrational states and hydrogen riding modes," J. Phys. Chem. B **107**(28), 6838–6845 (2003).

[98]C. Cavallari, D. Pontiroli, M. Jiménez-Ruiz, A. Ivanov, M. Mazzani, M. Gaboardi, M. Aramini, M. Brunelli, M. Riccò, and S. Rols, "Hydrogen on graphene investigated by inelastic neutron scattering," J. Phys.: Conf. Ser. **554**(1), 012009 (2014).

[99]Y. Xu, Z. Li, and W. Duan, "Thermal and thermoelectric properties of graphene," Small **10**(11), 2182–2199 (2014).

[100]J. Wang, J. K. Carson, M. F. North, and D. J. Cleland, "A new approach to modelling the effective thermal conductivity of heterogeneous materials," Int. J. Heat Mass Transfer **49**(17), 3075–3083 (2006).

[101]J. C. M. Garnett and J. Larmor, "XII. Colours in metal glasses and in metallic films," Philos. Trans. R. Soc. London Ser. A **203**(359–371), 385–420 (1904).

[102]H. Fricke, "The Maxwell-Wagner dispersion in a suspension of ellipsoids," J. Phys. Chem. **57**(9), 934–937 (1953).

[103]D. P. H. Hasselman and L. F. Johnson, "Effective thermal conductivity of composites with interfacial thermal barrier resistance," J. Compos. Mater. **21**(6), 508–515 (1987).

[104]D. A. G. Bruggeman, "Berechnung verschiedener physikalischer Konstanten von heterogenen Substanzen. I. Dielektrizitätskonstanten und Leitfähigkeiten der Mischkörper aus isotropen Substanzen," Ann. Phys. **416**(7), 636–664 (1935).

[105]R. Landauer, "The electrical resistance of binary metallic mixtures," J. Appl. Phys. **23**(7), 779–784 (1952).

[106]A. G. Every, Y. Tzou, D. P. H. Hasselman, and R. Raj, "The effect of particle size on the thermal conductivity of ZnS/diamond composites," Acta Metall. Mater. **40**(1), 123–129 (1992).

[107]C.-W. Nan, R. Birringer, D. R. Clarke, and H. Gleiter, "Effective thermal conductivity of particulate composites with interfacial thermal resistance," J. Appl. Phys. **81**(10), 6692–6699 (1997).

[108]S. Zhai, P. Zhang, Y. Xian, J. Zeng, and B. Shi, "Effective thermal conductivity of polymer composites: Theoretical models and simulation models," Int. J. Heat Mass Transfer **117**, 358–374 (2018).

[109]C.-W. Nan, G. Liu, Y. Lin, and M. Li, "Interface effect on thermal conductivity of carbon nanotube composites," Appl. Phys. Lett. **85**(16), 3549–3551 (2004).

[110]C. W. Nan, Z. Shi, and Y. Lin, "A simple model for thermal conductivity of carbon nanotube-based composites," Chem. Phys. Lett. **375**(5), 666–669 (2003).

[111]W. Lin, R. Zhang, and C. P. Wong, "Modeling of thermal conductivity of graphite nanosheet composites," J. Electron. Mater. **39**(3), 268–272 (2010).

[112]K. M. F. Shahil and A. A. Balandin, "Graphene–multilayer graphene nanocomposites as highly efficient thermal interface materials," Nano Lett. **12**(2), 861–867 (2012).

[113]F. Deng, Q.-S. Zheng, L.-F. Wang, and C.-W. Nan, "Effects of anisotropy, aspect ratio, and nonstraightness of carbon nanotubes on thermal conductivity of carbon nanotube composites," Appl. Phys. Lett. **90**(2), 021914 (2007).
[114]C. Wang, X. Sun, and J. Deng, "Micromechanical estimation of effective thermal conductivities of metal matrix nanocomposites with local carbon nanotube agglomeration," J. Alloys Compd. **793**, 191–201 (2019).
[115]P. Zhang, P. Yuan, X. Jiang, S. Zhai, J. Zeng, Y. Xian, H. Qin, and D. Yang, "A theoretical review on interfacial thermal transport at the nanoscale," Small **14**(2), 1702769 (2018).
[116]A. Minnich and G. Chen, "Modified effective medium formulation for the thermal conductivity of nanocomposites," Appl. Phys. Lett. **91**(7), 073105 (2007).
[117]P. Kapitza, "The study of heat transfer in helium. II," Zh. Eksp. Teor. Fiz. **11**, 1 (1941) [J. Phys. U.S.S.R. **4**, 181 (1941)].
[118]C. Monachon, L. Weber, and C. Dames, "Thermal boundary conductance: A materials science perspective," Annu. Rev. Mater. Res. **46**(1), 433–463 (2016).
[119]A. Giri and P. E. Hopkins, "A review of experimental and computational advances in thermal boundary conductance and nanoscale thermal transport across solid interfaces," Adv. Funct. Mater. **30**(8), 1903857 (2020).
[120]R. Hanus, R. Gurunathan, L. Lindsay, M. T. Agne, J. Shi, S. Graham, and G. J. Snyder, "Thermal transport in defective and disordered materials," Appl. Phys. Rev. **8**(3), 031311 (2021).
[121]R. Landauer, "Spatial variation of currents and fields due to localized scatterers in metallic conduction," IBM J. Res. Dev. **1**(3), 223–231 (1957).
[122]R. Mazo, *Theoretical Studies on Low Temperature Phenomena* (Yale University, 1955).
[123]E. T. Swartz, *Solid-Solid Thermal Boundary Resistance* (Cornell University, 1987).
[124]E. T. Swartz and R. O. Pohl, "Thermal boundary resistance," Rev. Mod. Phys. **61**(3), 605–668 (1989).
[125]R. Gurunathan, R. Hanus, S. Graham, A. Garg, and G. J. Snyder, "Thermal resistance at a twist boundary and a semicoherent heterointerface," Phys. Rev. B **103**(14), 144302 (2021).
[126]C. Hua, X. Chen, N. K. Ravichandran, and A. J. Minnich, "Experimental metrology to obtain thermal phonon transmission coefficients at solid interfaces," Phys. Rev. B **95**(20), 205423 (2017).
[127]K. Gordiz and A. Henry, "Phonon transport at interfaces: Determining the correct modes of vibration," J. Appl. Phys. **119**(1), 015101 (2016).
[128]J. Yang, *Thermal Conductivity: Theory, Properties, and Applications* (Springer US, 2004).
[129]Z. Tian, S. Lee, and G. Chen, "Comprehensive review of heat transfer in thermoelectric materials and devices," Annu. Rev. Heat Transfer **17**, 425–483 (2014).
[130]P. Debye, "Zur Theorie der spezifischen Wärmen," Ann. Phys. **344**(14), 789–839 (1912).
[131]A. T. Petit and P. L. Dulong, "Recherches sur Quelques Points Importants de la Théorie de la Chaleur," Ann. Chim. Phys. **10**, 395–413 (1819).
[132]J. Mao, Z. Liu, J. Zhou, H. Zhu, Q. Zhang, G. Chen, and Z. Ren, "Advances in thermoelectrics," Adv. Phys. **67**(2), 69–147 (2018).
[133]A. A. Maznev and O. B. Wright, "Demystifying Umklapp vs normal scattering in lattice thermal conductivity," Am. J. Phys. **82**(11), 1062–1066 (2014).
[134]J. Callaway, "Model for lattice thermal conductivity at low temperatures," Phys. Rev. **113**(4), 1046–1051 (1959).
[135]P. B. Allen, "Improved Callaway model for lattice thermal conductivity," Phys. Rev. B **88**(14), 144302 (2013).
[136]J. Ma, "Examining the Callaway model for lattice thermal conductivity," Phys. Rev. B **90**(3), 035203 (2014).
[137]D. Broido, M. Heine, N. Mingo, and A. J. Minnich, "Simulation of phonons," In *Advanced Thermoelectrics* (CRC Press, 2017).
[138]P. G. Klemens, *Encyclopedia of Physics* (Springer-Verlag, 1956).
[139]P. G. Klemens, "The scattering of low-frequency lattice waves by static imperfections," Proc. Phys. Soc. Sect. A **68**(12), 1113–1128 (1955).
[140]D. Li, J. M. Li, J. C. Li, Y. S. Wang, J. Zhang, X. Y. Qin, Y. Cao, Y. S. Li, and G. D. Tang, "High thermoelectric performance of n-type $Bi_2Te_{2.7}Se_{0.3}$ via nanostructure engineering," J. Mater. Chem. A **6**(20), 9642–9649 (2018).
[141]W. Kim and A. Majumdar, "Phonon scattering cross section of polydispersed spherical nanoparticles," J. Appl. Phys. **99**(8), 084306 (2006).
[142]N. Mingo, D. Hauser, N. P. Kobayashi, M. Plissonnier, and A. Shakouri, "Nanoparticle-in-alloy approach to efficient thermoelectrics: Silicides in SiGe," Nano Lett. **9**(2), 711–715 (2009).
[143]A. Ioffe and A. Regel, "Non-crystalline, amorphous, and liquid electronic semiconductors," Progr. Semiconductors **4**, 237–291 (1960).
[144]M. Simoncelli, N. Marzari, and F. Mauri, "Unified theory of thermal transport in crystals and glasses," Nat. Phys. **15**(8), 809–813 (2019).
[145]L. Isaeva, G. Barbalinardo, D. Donadio, and S. Baroni, "Modeling heat transport in crystals and glasses from a unified lattice-dynamical approach," Nat. Commun. **10**(1), 3853 (2019).
[146]P. B. Allen, J. L. Feldman, J. Fabian, and F. Wooten, "Diffusons, locons and propagons: Character of atomic vibrations in amorphous Si," Philos. Mag. B **79**(11-12), 1715–1731 (1999).
[147]P. B. Allen and J. L. Feldman, "Thermal conductivity of disordered harmonic solids," Phys. Rev. B **48**(17), 12581–12588 (1993).
[148]H. R. Seyf and A. Henry, "A method for distinguishing between propagons, diffusions, and locons," J. Appl. Phys. **120**(2), 025101 (2016).
[149]Y. Luo, X. Yang, T. Feng, J. Wang, and X. Ruan, "Vibrational hierarchy leads to dual-phonon transport in low thermal conductivity crystals," Nat. Commun. **11**(1), 2554 (2020).
[150]R. Hanus, J. George, M. Wood, A. Bonkowski, Y. Cheng, D. L. Abernathy, M. E. Manley, G. Hautier, G. J. Snyder, and R. P. Hermann, "Uncovering design principles for amorphous-like heat conduction using two-channel lattice dynamics," Mater. Today Phys. **18**, 100344 (2021).
[151]X. Chen, A. Weathers, J. Carrete, S. Mukhopadhyay, O. Delaire, D. A. Stewart, N. Mingo, S. N. Girard, J. Ma, D. L. Abernathy *et al.*, "Twisting phonons in complex crystals with quasi-one-dimensional substructures," Nat. Commun. **6**(1), 6723 (2015).
[152]X. Xu, J. Zhou, and J. Chen, "Thermal transport in conductive polymer-based materials," Adv. Funct. Mater. **30**(8), 1904704 (2020).
[153]A. Henry, "Thermal transport in polymers," Annu. Rev. Heat Transfer **17**, 485–520 (2014).
[154]S. Ghaffari-Mosanenzadeh, O. Aghababaei Tafreshi, E. Dammen-Brower, E. Rad, M. Meysami, and H. E. Naguib, "A review on high thermally conductive polymeric composites," Polym. Compos. **43**(2), 692–711 (2022).
[155]J. Chen, L. Yan, W. Song, and D. Xu, "Interfacial characteristics of carbon nanotube-polymer composites: A review," Compos. Part A: Appl. Sci. Manuf. **114**, 149–169 (2018).
[156]N. Mohd Nurazzi, M. R. M. Asyraf, A. Khalina, N. Abdullah, F. A. Sabaruddin, S. H. Kamarudin, S. b Ahmad, A. M. Mahat, C. L. Lee, H. A. Aisyah *et al.*, "Fabrication, functionalization, and application of carbon nanotube-reinforced polymer composite: An overview," Polymers **13**(7), 1047 (2021).
[157]J. Hwang, T. Yoon, S. H. Jin, J. Lee, T.-S. Kim, S. H. Hong, and S. Jeon, "Enhanced mechanical properties of graphene/copper nanocomposites using a molecular-level mixing process," Adv. Mater. **25**(46), 6724–6729 (2013).
[158]S. Shaikh, L. Li, K. Lafdi, and J. Huie, "Thermal conductivity of an aligned carbon nanotube array," Carbon **45**(13), 2608–2613 (2007).
[159]E. Neubauer, M. Kitzmantel, M. Hulman, and P. Angerer, "Potential and challenges of metal-matrix-composites reinforced with carbon nanofibers and carbon nanotubes," Compos. Sci. Technol. **70**(16), 2228–2236 (2010).
[160]X. Li, J. Liang, J. Zhou, J. Luo, Y. Wang, and L. Qi, "Fabrication and characterization of aligned carbon nanotubes cluster reinforced magnesium composite based on ultrasound/magnetic compound field," Procedia Eng. **207**, 95–100 (2017).
[161]X. Liang, Y. Yang, F. Dai, and C. Wang, "Orientation dependent physical transport behavior and the micro-mechanical response of ZnO nanocomposites induced by SWCNTs and graphene: Importance of intrinsic anisotropy and interfaces," J. Mater. Chem. C **7**(5), 1208–1221 (2019).
[162]G.-M. Vallet, M. Dunand, and J.-F. Silvain, "Influence of carbon nanotubes dispersion on thermal properties of copper-carbon nanotubes (CNTs) composite materials," Univ. J. Mater. Sci. **3**(4), 55–61 (2015).
[163]Z. Zhou, Y. Huang, B. Wei, Y. Yang, D. Yu, Y. Zheng, D. He, W. Zhang, M. Zou, J.-L. Lan *et al.*, "Compositing effects for high thermoelectric performance of Cu_2Se-based materials," Nat. Commun. **14**(1), 2410 (2023).

[164]G. Yang, L. Sang, F. F. Yun, D. R. G. Mitchell, G. Casillas, N. Ye, K. See, J. Pei, X. Wang, J.-F. Li *et al.*, "Significant enhancement of thermoelectric figure of merit in BiSbTe-based composites by incorporating carbon microfiber," Adv. Funct. Mater. **31**(15), 2008851 (2021).
[165]X. Wang, X. Wang, Z. Wang, Y. Guo, and Y. Wang, "Thermal transport across Cu-metal-carbon nanotube interfaces enhanced by effective interfacial interaction," Chem. Phys. **542**, 111019 (2021).
[166]K. S. Ahn, J. S. Kim, C. O. Kim, and J. P. Hong, "Non-reactive RF treatment of multiwall carbon nanotube with inert argon plasma for enhanced field emission," Carbon **41**(13), 2481–2485 (2003).
[167]M. Garzia Trulli, E. Sardella, F. Palumbo, G. Palazzo, L. C. Giannossa, A. Mangone, R. Comparelli, S. Musso, and P. Favia, "Towards highly stable aqueous dispersions of multi-walled carbon nanotubes: The effect of oxygen plasma functionalization," J. Colloid Interface Sci. **491**, 255–264 (2017).
[168]K. P. Maity, A. Patra, and V. Prasad, "Influence of the chemical functionalization of carbon nanotubes on low temperature ac conductivity with polyaniline composites," J. Phys. D: Appl. Phys. **53**(12), 125303 (2020).
[169]O. I. Nakonechna, N. N. Belyavina, M. M. Dashevskyi, K. O. Ivanenko, and S. L. Revo, "Novel Ti_2CuC_x and $Ti_3Cu_2C_x$ carbides obtained by sintering of products of mechanochemical synthesis of Ti, Cu and carbon nanotubes," Phys. Chem. Solid State **19**(2), 179–185 (2019).
[170]A. F. Quintero-Jaime, D. Cazorla-Amorós, and E. Morallón, "Electrochemical functionalization of single wall carbon nanotubes with phosphorus and nitrogen species," Electrochim. Acta **340**, 135935 (2020).
[171]Y. Zhao, Y. Li, J. Qiao, S. Jiang, P. Mao, J. Qiu, S. Kang, J. Tan, K. Tai, and C. Liu, "Decoupling phonon and carrier scattering at carbon nanotube/Bi_2Te_3 interfaces for improved thermoelectric performance," Carbon **170**, 191–198 (2020).
[172]S. Cho, K. Kikuchi, and A. Kawasaki, "On the role of amorphous intergranular and interfacial layers in the thermal conductivity of a multi-walled carbon nanotube–copper matrix composite," Acta Mater. **60**(2), 726–736 (2012).
[173]I. Firkowska, A. Boden, A.-M. Vogt, and S. Reich, "Tailoring the contact thermal resistance at metal–carbon nanotube interface," Phys. Status Solidi B **248**(11), 2520–2523 (2011).
[174]H. Pal and V. Sharma, "Thermal conductivity of carbon nanotube–silver composite," Trans. Nonferrous Met. Soc. China **25**(1), 154–161 (2015).
[175]J. Williams, W. Broughton, T. Koukoulas, and S. S. Rahatekar, "Plasma treatment as a method for functionalising and improving dispersion of carbon nanotubes in epoxy resins," J. Mater. Sci. **48**(3), 1005–1013 (2013).
[176]K. T. Kim, T. S. Min, and I. Son, "The influence of surface functionalization on the thermoelectric properties of carbon nanotube/Bi_2Te_3 composites," J. Nanosci. Nanotechnol. **16**(10), 10777–10781 (2016).
[177]M. M. Billah and Q. Chen, "Thermal conductivity of Ni-coated MWCNT reinforced 70Sn-30Bi alloy," Compos. Part B: Eng. **129**, 162–168 (2017).
[178]A. Chakravarty, R. Singh, S. Roy, U. Chowdhury, S. Basu, and S. K. Biswas, "Aluminum nitride-single walled carbon nanotube nanocomposite with superior electrical and thermal conductivities," J. Am. Ceram. Soc. **100**(8), 3360–3364 (2017).
[179]K. Chu, C-c Jia, and W-s Li, "Thermal conductivity enhancement in carbon nanotube/Cu–Ti composites," Appl. Phys. A **110**(2), 269–273 (2013).
[180]A. Jayaraj, C. V. K. N. S. N. Moorthy, V. S. N. Venkataramana, S. Jaikumar, and V. Srinivas, "Corrosion, mechanical and thermal properties of aluminium alloy metal matrix nano composites (AA-MMNCs) with multi-walled carbon nanotubes," SN Appl. Sci. **2**(7), 1259 (2020).
[181]Y. Ji, G. Li, C. Chang, Y. Sun, and H. Ma, "Investigation on carbon nanotubes as thermal interface material bonded with liquid metal alloy," J. Heat Transfer **137**(9), 091017 (2015).
[182]P. Mandal and S. C. Mondal, "Investigation of electro-thermal property for Cu-MWCNT composite coating on anodized 6061 aluminium alloy," Appl. Surf. Sci. **454**, 138–147 (2018).
[183]J.-H. Nie, C.-C. Jia, X. Jia, Y. Li, Y.-F. Zhang, and X.-B. Liang, "Fabrication and thermal conductivity of copper matrix composites reinforced by tungsten-coated carbon nanotubes," Int. J. Miner. Metall. Mater. **19**(5), 446–452 (2012).
[184]X. L. Shi, H. Yang, G. Q. Shao, X. L. Duan, L. Yan, Z. Xiong, and P. Sun, "Fabrication and properties of W–Cu alloy reinforced by multi-walled carbon nanotubes," Mater. Sci. Eng. A **457**(1), 18–23 (2007).
[185]R. M. Sundaram, A. Sekiguchi, M. Sekiya, T. Yamada, and K. Hata, "Copper/carbon nanotube composites: Research trends and outlook," R. Soc. Open Sci. **5**(11), 180814 (2018).
[186]J. Nie, C. Jia, X. Jia, Y. Zhang, N. Shi, and Y. Li, "Fabrication, microstructures, and properties of copper matrix composites reinforced by molybdenum-coated carbon nanotubes," Rare Met. **30**(4), 401 (2011).
[187]S. Zhou, C. Wu, T. Zhang, and Z. Zhang, "Carbon nanotube- and Fe_p-reinforced copper–matrix composites by laser induction hybrid rapid cladding," Scr. Mater. **76**, 25–28 (2014).
[188]J. Kong, C-y Zhang, and X. Cheng, "Novel Cu–Cr alloy matrix CNT composites with enhanced thermal conductivity," Appl. Phys. A **112**(3), 631–636 (2013).
[189]M. Yuan, L. Sun, X. W. Lu, P. Jiang, and X. H. Bao, "Enhancing the thermoelectric performance of Cu–Ni alloys by introducing carbon nanotubes," Mater. Today Phys. **16**, 100311 (2021).
[190]Q. Hao, Y. Xiao, and H. Zhao, "Analytical model for phonon transport analysis of periodic bulk nanoporous structures," Appl. Therm. Eng. **111**, 1409–1416 (2017).
[191]I. Sumirat, Y. Ando, and S. Shimamura, "Theoretical consideration of the effect of porosity on thermal conductivity of porous materials," J. Porous Mater. **13**(3), 439–443 (2006).
[192]J.-H. Lee, G. A. Galli, and J. C. Grossman, "Nanoporous Si as an efficient thermoelectric material," Nano Lett. **8**(11), 3750–3754 (2008).
[193]Q. Zhang, L. Xu, Z. Zhou, L. Wang, W. Jiang, and L. Chen, "Constructing nanoporous carbon nanotubes/Bi_2Te_3 composite for synchronous regulation of the electrical and thermal performances," J. Appl. Phys. **121**(5), 055104 (2017).
[194]S. Li, R. Wang, W. Zhu, M. Chu, Z. Huang, Y. Zhang, W. Zhao, F. Liu, J. Luo, Y. Xiao *et al.*, "Achieving high thermoelectric performance by introducing 3D atomically thin conductive framework in porous $Bi_2Te_{2.7}Se_{0.3}$-carbon nanotube hybrids," Adv. Electron. Mater. **6**(8), 2000292 (2020).
[195]H.-S. Yang, G. R. Bai, L. J. Thompson, and J. A. Eastman, "Interfacial thermal resistance in nanocrystalline yttria-stabilized zirconia," Acta Mater. **50**(9), 2309–2317 (2002).
[196]Q. Zhang, Z. Zhou, M. Dylla, M. T. Agne, Y. Pei, L. Wang, Y. Tang, J. Liao, J. Li, S. Bai *et al.*, "Realizing high-performance thermoelectric power generation through grain boundary engineering of skutterudite-based nanocomposites," Nano Energy **41**, 501–510 (2017).
[197]T. S. Min, K. T. Kim, and I. Son, "The influence of interfacial defect-region on the thermoelectric properties of nanodiamond-dispersed $Bi_2Te_{2.7}Se_{0.3}$ matrix composites," Appl. Surf. Sci. **415**, 109–113 (2017).
[198]G. Yang, L. Sang, D. R. G. Mitchell, F. Fei Yun, K. Wai See, A. Jumlat Ahmed, S. Sayyar, A. Bake, P. Liu, L. Chen *et al.*, "Enhanced thermoelectric performance and mechanical strength of n-type BiTeSe materials produced via a composite strategy," Chem. Eng. J. **428**, 131205 (2022).
[199]See https://www.cheaptubes.com/product-category/single-walled-carbon-nanotubes/ for "Single Walled Carbon Nanotubes Products. Cheap Tubes."
[200]P. Kim, L. Shi, A. Majumdar, and P. L. McEuen, "Thermal transport measurements of individual multiwalled nanotubes," Phys. Rev. Lett. **87**(21), 215502 (2001).
[201]E. Pop, D. Mann, Q. Wang, K. Goodson, and H. Dai, "Thermal conductance of an individual single-wall carbon nanotube above room temperature," Nano Lett. **6**(1), 96–100 (2006).
[202]A. E. Aliev, M. H. Lima, E. M. Silverman, and R. H. Baughman, "Thermal conductivity of multi-walled carbon nanotube sheets: Radiation losses and quenching of phonon modes," Nanotechnology **21**(3), 035709 (2009).
[203]K. Ahmad, C. Wan, and M. A. Al-Eshaikh, "Effect of uniform dispersion of single-wall carbon nanotubes on the thermoelectric properties of BiSbTe-based nanocomposites," J. Electron. Mater. **46**(2), 1348–1357 (2017).
[204]A. Moisala, Q. Li, I. A. Kinloch, and A. H. Windle, "Thermal and electrical conductivity of single- and multi-walled carbon nanotube-epoxy composites," Compos. Sci. Technol. **66**(10), 1285–1288 (2006).
[205]R. Gulotty, M. Castellino, P. Jagdale, A. Tagliaferro, and A. A. Balandin, "Effects of functionalization on thermal properties of single-wall and multi-wall carbon nanotube–polymer nanocomposites," ACS Nano **7**(6), 5114–5121 (2013).

[206]W.-T. Hong and N.-H. Tai, "Investigations on the thermal conductivity of composites reinforced with carbon nanotubes," Diamond Related Mater. **17**(7), 1577–1581 (2008).
[207]K. Gordiz and A. Henry, "A formalism for calculating the modal contributions to thermal interface conductance," New J. Phys. **17**(10), 103002 (2015).
[208]A. Rohskopf, R. Li, T. Luo, and A. Henry, "A computational framework for modeling and simulating vibrational mode dynamics," Modell. Simul. Mater. Sci. Eng. **30**(4), 045010 (2022).
[209]G. C. Sosso, V. L. Deringer, S. R. Elliott, and G. Csányi, "Understanding the thermal properties of amorphous solids using machine-learning-based interatomic potentials," Mol. Simul. **44**(11), 866–880 (2018).